Winter 2002

Active and Adaptive Flow Control of Twin-Tail Buffet and Applications

Zhi Yang
Old Dominion University

ACTIVE AND ADAPTIVE FLOW CONTROL OF TWIN-TAIL BUFFET AND APPLICATIONS

by

Zhi Yang
B.S., July 1992, Beijing University of Aeronautics & Astronautics
M.S., July 1995, Beijing University of Aeronautics & Astronautics

A Dissertation Submitted to the Faculty of
Old Dominion University in Partial Fulfillment of the
Requirements for the Degree of

DOCTOR OF PHILOSOPHY

AEROSPACE ENGINEERING

OLD DOMINION UNIVERSITY
December 2002

Approved by

Osama A. Kandil (Director)

Oktay Baysal (Member)

Brett A. Newman (Member)

Gene Hou (Member)

ABSTRACT

ACTIVE AND ADAPTIVE FLOW CONTROL OF TWIN-TAIL BUFFET AND APPLICATIONS

Zhi Yang
Old Dominion University, 2002
Director: Dr. Osama A. Kandil

Modern fighter aircraft with dual vertical tails are operated at high angles of attack. The vortex generated by leading edge extension (LEX) breaks down before reaching the two vertical tails. The wake of highly unsteady, turbulent flow causes unbalanced broadband aerodynamic loading on the tails and may produce severe buffet on the tails and lead to tail fatigue failure.

Flow suction along the vortex cores (FSVC) is investigated as an active control method for tail-buffet alleviation. Suction tubes have been tilted at different angles to study the control effectiveness of suction tubes orientation. Flow field response, aerodynamic loading and aeroelastic results are compared with the no-control case. These flow modifications produce lower tip bending and rotation angle deflections and accelerations. Moreover, the root bending and twisting moments are reduced in comparison with the no-control case. However, there was no shift in the frequencies at which the peaks of the power spectral density (PSD) responses occurred. The primary effect of the FSVC methods is the amplitude reduction of the aeroelastic responses up to 30%. A parametric investigation is conducted and the best control effectiveness is obtained with the suction tubes tilted at -10°. Next, the twin-tail buffet alleviation is addressed by using adaptive flow control, and an adaptive active control method is developed. Control ports, whose locations are determined according to the locations of a range of high-pressure difference, are placed within a small area on the tail surfaces. Flow suction and blowing are applied through these control ports in order to equalize the pressures on the two surfaces of the tail. Mass flow rate through each port is proportional to the pressure difference across the tail at the location of this port. Comparing the flow field and aeroelastic response with the no-control case, the normal-force and twisting-

moment distributions are substantially decreased along with the damping of their amplitudes of variation. The bending-deflection and rotation-angle responses have not changed their sign. The PSD of the root bending moment and root twisting moment have shown substantial decreases of more than 70%. The tail tip acceleration responses have shown similar decreases too.

Next, a parallel high-order compact-scheme code (PHCC) is developed to investigate flow control more accurately and more efficiently. The validation cases are presented and compared with theoretical results, experimental results and other computational results. The PHCC results show good accuracy and high efficiency. Flow computational simulations of Jet and Vortex Actuator (JaVA) or synthetic jet have been investigated. The computational results show good agreement with the experimental data and other computational results. Simplified 2D models, which include an airfoil under the effect of JaVAs and synthetic jet actuators, are developed and investigated for control effectiveness. Simulation results show: with properly selected parameters, the oscillating amplitude of pressure difference and normal force acting on airfoil can be reduced, the peak of the normal force PSD can be reduced and the frequencies at which the peaks of the pressure difference PSD responses occurred can be shifted to higher frequency levels. Too low or too high exciting frequencies have no effect or adverse effect. Low exciting velocity may not produce enough disturbances to suppress the pressure oscillation.

To My Wife
To My Father and Mother

LIST OF SYMBOLS

a	coefficient of compact scheme
$\bar{a}$	acceleration vector
$\bar{a}_m$	covariant base vector
a_∞	speed of sound in freestream
A	cross section area of blowing/suction tube
$\overline{A}$	Roe average matrix
b	coefficient of compact scheme
$\overline{b}$	wing span
$b(z)$	tail cross-section width
c	speed of sound, Sutherland's constant
C	constant
C_{ij}	coefficient of compact scheme at boundary
C_p	pressure coefficient
C_Q	blowing/suction coefficient
C_{RBM}	coefficient of root bending moment ($M_{RB}/q_\infty s_t c$)
C_{RTM}	coefficient of root twisting moment ($M_{RT}/q_\infty s_t c$)
CFL	Courant-Friedrichs-Lewy number
e	total energy per unit mass
e_i	eigenvectors of the Jacobian matrix
E	modulus of elasticity
E_L	function of Q at left interface
E_R	function of Q at right interface
$\bar{E}$	inviscid flux
$\bar{E}_v$	viscous flux
EI	bending stiffness
f	frequency
GJ	torsional rigidity
H_L	stagnation enthalpy per unit mass at left interface

H_R	stagnation enthalpy per unit mass at right interface
I_i	metric identities
$\bar{I}$	the number of bending modes
I(z)	area moment of inertia
$I_{zzCM}(z)$	mass moment of inertia about the center of mass axis
I_θ	mass moment of inertia about the elastic axis
J	Jacobian of coordinate transformation
k	coefficient of thermal conductivity
K_{ij}	terms of stiffness matrix
L	reference length
m	mass
M_{RB}	root bending moment
M_{RT}	root twisting moment
M	Mach number
Ma	Mach number
M_∞	Mach number of freestream
M_t	twisting moment per unit length
$\overline{M}$	the number of bending modes and torsion modes
M_{ij}	terms of mass matrix
n	non-dimensional frequency
$\hat{n}$	unit normal vector
$\hat{n}_{b/s}$	unit normal vector for blowing and suction
N	normal force per unit length
$\overline{N}_i$	terms of force vector
p	static pressure
P_r	Prandtl number
q_k	heat-flux component
q_i	generalized coordinates for bending
q_j	generalized coordinates for torsion
Q	flow vector in the Cartesian coordinates

Q_L	flow variables at left interface
Q_R	flow variables at right interface
$\bar{Q}$	vector of conserved flow variables in generalized coordinates
$\bar{r}$	displacement vector
R	residual terms
Re	Reynolds number
$\bar{R}_v$	residual due to viscous terms
S	wing area
$\tilde{S}_{kn}$	velocity gradient tensor
t	dimensional time, thickness
T	temperature, period of oscillation
$\tilde{u}_k$	filtered velocity
u_τ	friction velocity
U_∞	velocity of free stream
V	volume of the computational domain
$\bar{v}_{b/s}$	velocity vector of blowing/suction
w	bending deflection of the tail
x	x-coordinate
x_j	cartesian coordinates
x_θ	distance between the elastic axis and the inertial axis
y^+	normal distance from a solid wall in wall unit
α	angle of attack or dynamic pitch angle, coefficient of compact scheme
α_i	projection of the difference in Q between the right and left interface
α_f	free parameter
β_i	frequencies
ξ_j	computational coordinates
ρ	density
ρ_∞	density in freestream
μ	molecular viscosity coefficient

μ_∞	molecular viscosity coefficient in freestream
τ_{kn}	shear stress tensor
$\partial\Re$	boundary enclosing the computational domain
λ	bulk viscosity coefficient
λ_i	eigenvalues
γ	constant
ε_w, ε_θ	error in bending and torsion
ϕ	free vibration modes, flow variables
ϕ'	spatial derivative of ϕ
$\hat{\phi}$	filter value of ϕ
Δ^2	spatial filter width
τ	non-dimensional time
τ_w	wall shear stress
θ	torsion deflection angle in radians or dynamic roll angle
$\theta_{\tau\tau}$	tail-up torsion acceleration
δ_{ij}	Kronecker delta function
ω	natural frequency
ξ_x,ξ_y,ξ_z	metrics
η_x,η_y,η_z	metrics
ζ_x,ζ_y,ζ_z	metrics

TABLE OF CONTENTS

LIST OF TABLES

LIST OF FIGURES

CHAPTER 1: INTRODUCTION

1.1 Motivation

Modern designs of fighter aircraft require high agility and maneuverability, which are achieved by the combination of delta wings with leading edge extensions (LEX) and vertical tail(s). When aircraft are operated at high angles of attack, the LEX maintains high lift by generating a pair of leading edge vortices. At some angle of attack, as shown in Figure 1.1, the vortex generated by LEX breaks down before reaching the two vertical tails. The wake of highly unsteady, turbulent flow produced by this vortex breakdown causes unbalanced aerodynamic loading on the tails. According to experiments, the power spectrums of unsteady pressure acting on tails are broadband and may cover the resonance frequencies of the tails, as shown in Figure 1.2. This may produce severe buffet on the tails and lead to tail fatigue failure.

The buffet phenomenon has been investigated as early as the 1930s. The purpose of such studies is to understand and control the buffet phenomenon. How to control this flow-induced-structure-vibration, in fact, is to keep the frequencies of aerodynamic loading away from the resonance frequencies of the structure, and at the same time, not to compromise other aerodynamic and stability requirements of the aircraft.

Computational simulation is a powerful tool for the study of the buffet problems. However, the computational simulation of the whole aircraft is expensive and sometimes unnecessary. A simple model for the essence of the tail buffet is highly desirable to study the buffet phenomenon and its control. This could be achieved by isolating the ingredients of the buffet problem from the whole aircraft. A delta-wing/twin-tail configuration in a vortex breakdown flow provides an efficient and effective model to study the tail buffet phenomenon. Thus, the computational resources are focused on a small region for high computational resolution and efficiency.

Micro-electro-mechanical System (MEMS) techniques provide new and more practical methods to modify and control flow field. Jet and vortex actuator (JaVA) and synthetic jet actuator are few examples of the MEMS. Their potential performances for buffet control should be investigated.

The reference model used for this work is the *AIAA Journal*.

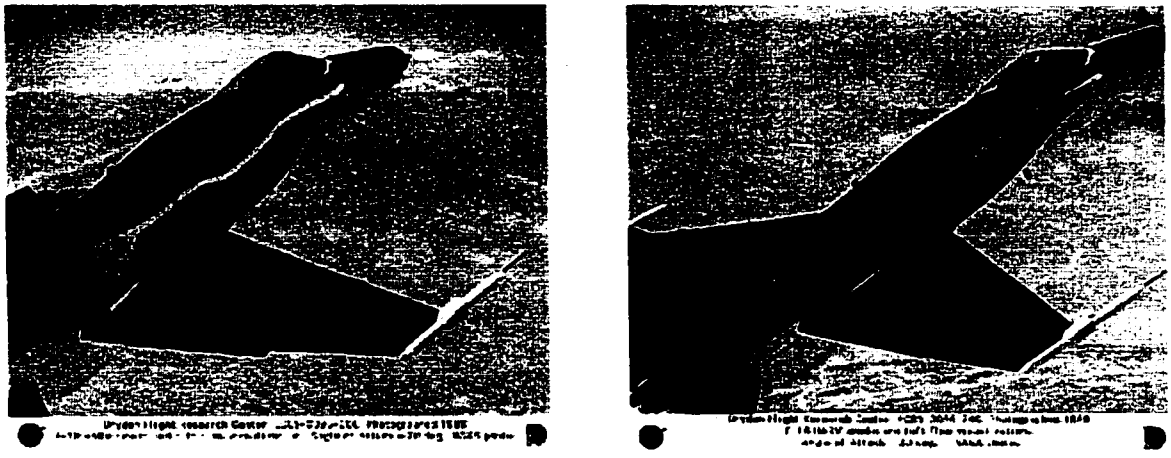

$\alpha = 20°$ $\alpha = 30°$

Figure 1.1 Flow visualization of F-18 (HARV) vortex burst, NASA Dryden Photo, EC89-0096-206, EC89-0096-240, 1989.

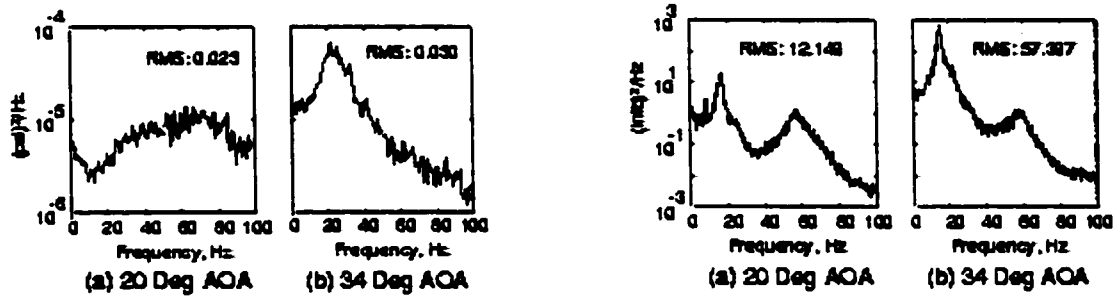

Differential Pressures Root Bending Moment

Figure 1.2 Differential pressures and root bending moment near mid-chord, 1/6-scale F/A-18 with flexible tail.[92] The first bending mode and the first torsion mode of the vertical tail are 15Hz and 58Hz, respectively.

1.2 The Present Research

Flow control has always been one of the main research areas in aerodynamics. There are passive methods, such as aerodynamic shaping, winglets, wing strakes and wing flaps, and active methods, such as blowing, suction and surface heating. Recently, adaptive active control methods, which integrate active control and sensors, microprocessors and actuators for flow actuation, have shown more promising prospects.[1] The purpose of this research is to investigate different active flow control methods for alleviating aircraft tail-buffet and other applications. A simple model, which considers the essence of tail buffet, is used. The model consists of a sharp-edged delta wing and

twin-tails. The delta wing is assumed to be rigid and is used to generate a pair of vortices. The tails are flexible and mathematically modeled as cantilevered beams, with varying cross sectional area, which are fixed at the root and allowed to oscillate in both bending and torsion. This aeroelastic problem is a multidisciplinary problem that is solved using fluid flow equations, structure dynamic equations and grid displacement equations. First, the fluid flow equations are solved using time-accurate, implicit, upwind, flux-difference splitting, finite-volume scheme to obtain the flow field and the aerodynamic loading on the tails. Next, the aeroelastic equations, which are transformed into a set of ordinary differential equations by using modal analysis and the Galerkin method, are solved accurately in time by using fifth-order Runge-Kutta scheme to obtain the bending and torsion deflections, velocities and accelerations of the tails. Finally, the grid displacement equations are solved to update the grid coordinates according to the tail deflection. Different active flow control methods are applied near the tails or on the surface of tails. Structure response results are compared between the controlled cases and no controlled cases.

Since 1990, developments in Micro-electro-mechanical System (MEMS) and materials like piezo-ceramics have led to innovative actuators, such as synthetic jet actuator and Jet and Vortex Actuator (JaVA). A lot of experimental and numerical studies have been conducted to investigate the synthetic jet actuator. Compared with synthetic jet actuator, JaVA is more flexible since it is able to generate four primary flow regimes (vortex flow, wall jet, free jet and oblique jet), which may be used for active flow control. In the present research work the JaVA actuators are investigated for flow control. Application of flow control using a synthetic jet actuator is also investigated and compared with the JaVA actuators. The size of JaVA (about 10mm) and synthetic jet actuator are much less than the size of wing or tail. Many actuators may be needed on the tail surface to control its buffet, and the size of the grid would be very big that would require prohibitive computational resources. Therefore, the use of actuators for buffet control of the delta wing/twin-tail model is very expensive computationally and may not be appropriate as the first step. Thus, an alternative simplified 2D model, which includes an airfoil and a JaVA or a synthetic jet actuator, is developed and investigated. The actuator is placed on the surface of the airfoil in order to control the flow and suppress

the amplitude of pressure oscillation. A parallel high order compact scheme code (PHCC) is developed and applied for the JaVA and synthetic jet actuator simulation studies. The PHCC is not only more accurate but also more efficient than the lower order scheme used before.

In Chapter 2, a literature survey is presented. This chapter includes brief reviews of vortex-generated lift, vortex breakdown over delta wing, state of the art of experimental and numerical investigations of vortex-breakdown induced tail buffet, active flow control, tail buffet alleviation and high order numerical simulation.

In Chapter 3, the mathematical formulations of the fluid flow equations, structure dynamics equations and the grid displacement equations are presented. The initial conditions and boundary conditions are also presented. The implicit, upwind, Roe flux-difference splitting, finite volume scheme is applied to the numerical formulation of fluid flow equations. The modal analysis and Galerkin method are applied to the numerical formulation of structure dynamics equations. The development of a time accurate, implicit, 6^{th} order compact scheme with 10^{th} order filter is also included.

In Chapter 4, computational results of the active flow control of tail buffet for the delta-wing/twin-tail configuration by using flow suction along vortex core (FSVC) are presented. The position and direction of suction tubes are investigated. The primary effect of the FSVC method is the amplitude reduction of the aeroelastic responses.

In Chapter 5, computational results of adaptive active flow control by using blowing-suction ports on tails surface are presented. The distributions of the ports are investigated. The power spectral densities of the root bending moment and root twisting moment have shown substantial decreases of more than 70%.

In Chapter 6, validations of the parallel high-order compact-scheme code (PHCC) are presented. The validation cases include inviscid and viscous, steady and unsteady flow problems. It has been shown that the PHCC is accurate and efficient.

In Chapter 7, computational simulations of Jet and Vortex Actuator (JaVA) are conducted by using an incompressible two-dimensional Navier-Stokes flow solver (INS2D). Computational simulation of synthetic jet actuator is also conducted by using

PHCC. The computational results are in good agreements with experimental data and other published computational results. Applications of Jet and Vortex Actuator (JaVA) or synthetic jet actuator to flow control of a simplified 2D model are investigated by using the parallel high-order compact scheme code (PHCC). Parametric investigations of the control effectiveness of actuators are carried out.

In Chapter 8, conclusions of the present study are given and recommendations for future investigations are suggested.

CHAPTER 2: LITERATURE REVIEW

2.1 Introduction

The purpose of this study is to develop active and adaptive flow control tools for the tail buffet problem and other flow-control applications. For the problems associated with tail buffet, it is essential to understand the characteristics of the unsteady separated flows, which are produced by delta wings at high angles of attack during aircraft maneuvers. So in the first part of this review, a brief history of the discovery and study of vortical lift and vortex breakdown is presented. This will include the experimental work and computational techniques involving vortex breakdown over delta wings. In the second part, experimental and computational investigations of the tail-buffet phenomenon are presented. In the third part, active flow methods are summarized and discussed. In the fourth part, the tail-buffet alleviation methods, including flow control methods and structure control methods, are presented. In the last part, highly accurate computational schemes are presented.

2.2 Vortex Generated Lift and Vortex Breakdown Over Delta Wings

2.2.1 Discovery of Vortex Generated Lift

In the 1940s, the German researchers discovered the vortex generated lift in their design of the Me-262. According to Polhamus review[100] of vortex lift research, the Me-262 wing was designed with an 18° sweepback and inadvertently led to a speed advantage by delaying the onset of compressibility drag. In 1942, modified versions of the Me-262 had wings with sweep angle up to 50°. The highly swept delta wing was also under consideration. In 1946, researchers at Langley tested the captured German highly swept delta wing DM-1 glider to study the low speed characteristics of full scale, highly swept delta wing. Wilson and Lovell[135] sharpened the leading edge of the DM-1 and found that flow separated from the sharp leading edge and produced a strong vortex. The re-attachment of the leading-edge vortex delayed trailing-edge separation and largely increased the lift.

A schematic view of the vortex generated by a slender, sharp-edge delta wing is shown in Figure 2.1. The primary vortices reattach on the surface of delta wing and move outwards to the lead-edge, causing a secondary flow separation. These vortices induce a high suction pressure over the delta wing upper surface along the foot of the vortex core and generate a large increase of lift.

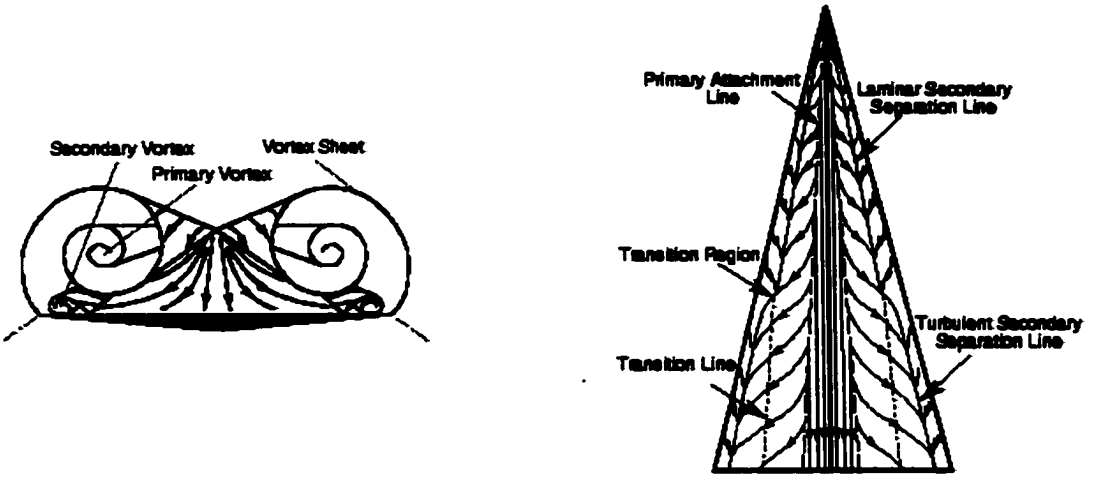

Figure 2.1 A schematic view of the vortical flow and the roll up of the shear layer over a slender, sharp edge delta wing, Visser and Washburn.[128]

2.2.2 Early Observation and Experimental Work of Vortex Breakdown

In 1957, Peckham and Atkinson[96] first discovered the vortex breakdown phenomenon when they tested a Gothic wing, which was a cropped delta wing with curved leading edge, for the lift and drag characteristic over a wide range of angles of attack and yaw angles. They found that the low pressure in the vortex core decreased the temperature, caused a water vapor condensation and revealed the path of the vortex core when the flow speeds were greater than 150 ft/sec and the angles of attack were between 20° and 30°. They noticed the length of vortex core decreased from three root chords downstream of the trailing edge to only a quarter root chords when the angles of attack changed from 25° to 30°. The trail of the condensation belled out before disappearing. They attributed this to the diffusion of the leading edge vortex core.

In 1958, Elle[18] found a similar phenomenon on a thin delta wing, and he was the first to call it *vortex breakdown*. He thought that the vortex breakdown was due to the failure of the downstream fluid transport in the vortex core.

In 1960 by using water tunnel, Werlé[131] observed a relationship between the breakdown location and the angles of attack of the delta wing. He suggested that the vortex breakdown is due to transition of the vortex flow from laminar to turbulence. He also noticed the effect of Reynolds number on the breakdown position at low Reynolds number, shown in Figure 2.2. However, Elle disagreed with Werlé. In his transonic studies published in 1960, Elle[19] found the breakdown location is relatively invariant at high Reynolds number. He concluded that the transition was not the primary mechanism of breakdown, but due to some sort of instability. He also suggested the weak shock at breakdown location was not the cause of breakdown, but a result of it.

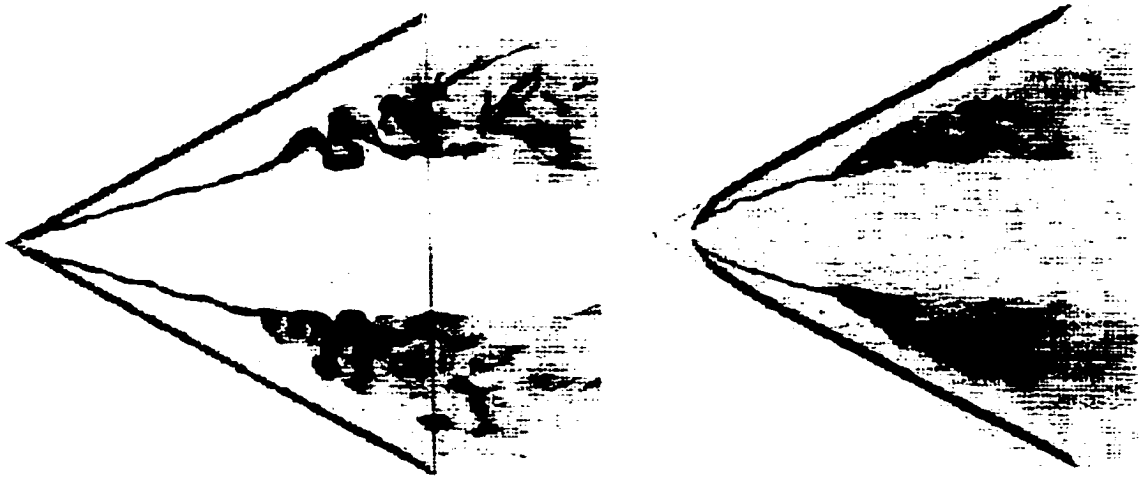

$\alpha = 20°$, $Re_c = 5000$ $\alpha = 20°$, $Re_c = 10000$

Figure 2.2 Effect of Reynolds number on vertex breakdown position on a 63° delta wing. [131]

In 1961, after conducting massive experimental investigations of vortex breakdown on a delta wing, Lambourne and Bryer[73] suggested the main reason of breakdown was the low total pressure in vortex core combined with an adverse pressure gradient along vortex axis. They also found two major modes of breakdown, an axisymmetric bubble type and an asymmetric spiral type. Figure 2.3 shows the famous photograph of Lambourne and Bryer[73], two modes of vortex breakdown can be seen. The lower vortex shows the axisymmetric bubble and the downstream irregular flow. The upper vortex shows the asymmetric spiral flow and the downstream turbulent flow. Figure 2.4 shows the detail of an axisymmetric bubble type of vortex breakdown. In the vortex core there is a stagnation point, which is followed by a sudden expansion zone. Flow is axisymmetric and smooth before the half bubble zone. Then the flow becomes irregular and transform to the spiral type. Figure 2.5 shows a sketch of the spiral type of

vortex breakdown. The vortex core is suddenly decelerated in the direction of vortex axis; the core is deflected spirally for a few revolutions after a sudden kink; and the flow is characterized with large-scale turbulence after a transition.

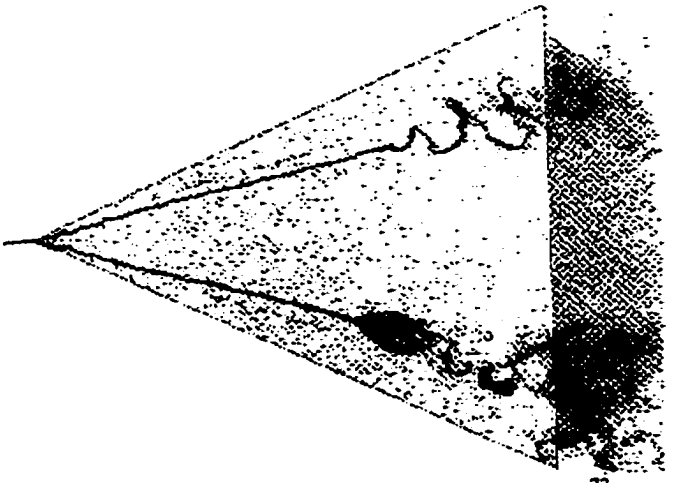

Figure 2.3 Vortex breakdown on a 65° delta wing, Re = 10000.[73] Upper vortex shows an asymmetric spiral type breakdown. Lower vortex shows an axisymmetric bubble type breakdown.

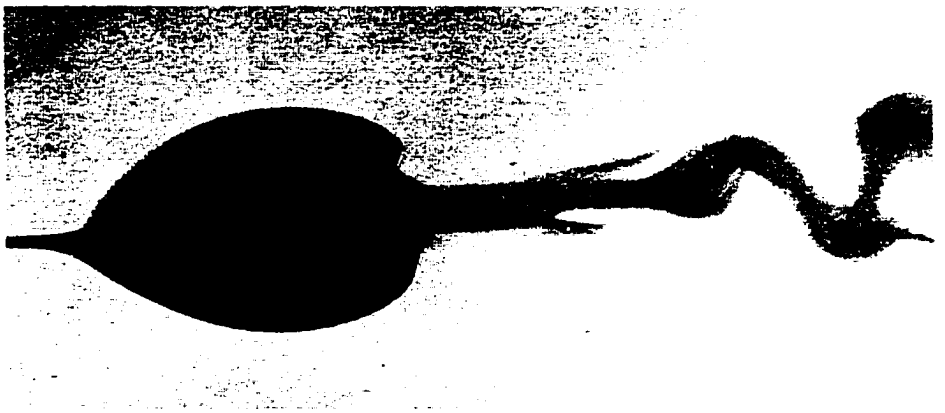

Figure 2.4 An axisymmetric bubble type vortex breakdown. The photo above was taken by Professor Turgut Sarpkaya who retains the copyright.

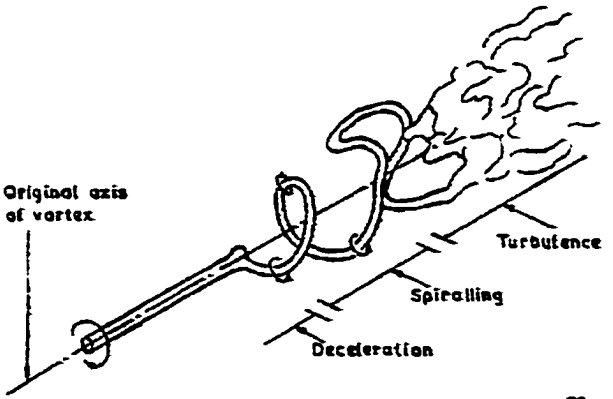

Figure 2.5 A sketch of asymmetric spiral type vortex breakdown.[73]

In 1988, Escudier[21] concluded the key ideas of these early investigations for vortex breakdown, which are: sudden transition, spiral disturbance instability, axial stagnation and wave motion. However, there is still no generally accepted theory of vortex breakdown.

When the angle of attack of a delta wing increases, the leading edge vortex grows strong, the adverse longitudinal pressure gradient increases, the flow in vortex core stagnates and the vortex breaks down into a large-scale turbulence. The characteristics of delta wing vortex breakdown were summarized by Lambourne and Bryer[73] as:

1. Vortex Breakdown includes a sudden deceleration of the vortex core axial flow, followed by an expansion of vortex core, a transition to the large-scale turbulence after a short time.
2. Low total pressure in the vortex core is an essential feature of breakdown.
3. A prerequisite for core flow to stagnate is a positive static pressure gradient along the vortex axis. The breakdown position is also sensitive to this pressure gradient. Decreasing the positive pressure gradient can delay breakdown.
4. The required positive pressure gradient could be attributed to viscous actions within the vortex core, or to deceleration of the flow outside the core. A small change in the external flow would be sufficient, because the external pressure gradient is magnified towards the axis of the core.
5. Depending on the ratio of the rotational to axial velocity components, the spontaneous expansion of a vortex core produces the pressure rise for core stagnation.
6. The vortex breakdown may be attributed to the pressure recovery associated with the existence of the tailing edge. If the breakdown occurs upstream of the trailing edge, its position depends on a combination of incidence and leading edge sweepback and is independent of Reynolds number.

In 1988, Payne[95] summarized the main factors affecting the location of the vortex breakdown:

1. Angle of attack: As angle of attack increases, the breakdown moves upstream.
2. External pressure gradient: As external pressure gradient increases, the breakdown moves upstream.

3. Aspect ratio: An increase of aspect ratio or a decrease of the swept angle moves the breakdown upstream.

Breakdown can be affected by using suction, blowing or flaps. Lambourne[73] and Hummel[37] found applying suction just downstream of the original breakdown position could eliminate the vortex breakdown. Blowing can delay the onset of breakdown. Upward deflection of a trailing edge flap can move the breakdown upstream and downward deflection can move the breakdown downstream.[73] But Erickson[20] found both upward and downward deflection moved the breakdown upstream.

In 1999, Reisenthel, Xie, Gursul and Bettencourt[101] investigated vortex breakdown over a 75° delta wing with a vertical fin placed near the trailing edge at a fixed angle of attack. Results showed the strong hysteretic effects in response to forced oscillations of the fin. Predications of nonlinear indicial theory corroborated two of the key experimental observations, the flattening of the hysteretic loops and the shift of the average location of vortex breakdown with increasing frequency.

2.2.3 Numerical Simulation of Vortex Breakdown

Early computations of vortex breakdown, Hall[33] and Gartshore[24], only considered the isolated, axisymmetric and steady vortices. The locations of vortex breakdown were identified when the computations diverged due to the high adverse pressure gradient. The early computations could not give any information of the flow downstream of vortex breakdown. The present study is focused on the effect of vortex breakdown on the tails. So, time accurate method is sought to predict the locations of vortex breakdown and the unsteady turbulent flow downstream of the breakdown.

In 1983, Krause, Shi and Hartwich[69] obtained the first time accurate, unsteady quasi-axisymmetric solution of vortex breakdown. A bubble type of vortex breakdown was observed, involving the formation, disappearance and reappearance of two internal vortices within the bubble.

In 1987, Taylor et al.[121] produced the solutions of stable vortex flow over a 76° delta wing at 20° angle of attack by solving the unsteady, thin layer Navier-Stokes

equations. Compared with experimental data, computation results under predicted the vorticity and total pressure loss in vortex core.

In 1990, Thomas et al.[122] predicted the flow over a low aspect ratio delta wing from 0° to 40° angle of attack by solving thin layer Navier-Stokes equations with an upwind finite volume scheme. A bubble type of vortex breakdown was observed at 40° angle of attack.

In 1991, O. Kandil, H. Kandil and Liu[42] produced the first time accurate, full Navier-Stokes solutions of supersonic vortex breakdown. They considered a supersonic, quasi-axisymmetric vortex flow in a configured circular duct. A shock was generated near the duct inlet and an unsteady vortex breakdown was predicted behind the shock. The flow was characterized by the evolution, convection and shedding of vortex breakdown bubbles. In a series of papers by O. Kandil, H. Kandil and Liu[44, 45, 46], extensive parametric investigations were conducted to determine the effects of grid resolution, Reynolds number, inflow/outflow boundary conditions and inlet swirl ratio. A detailed discussion of these results can be also found in the dissertation of H. Kandil.[41]

In 1991, Gordnier and Visbal[28] studied the vortex breakdown over a 76° delta wing at 20.5° angle of attack by solving the three dimensional, unsteady, full Navier-Stokes equations. The results showed that the shear layer emanating from the leading edge was subject to instability similar to that occurring in a two-dimensional shear layer flow.

In 1991, by using the full Navier-Stokes equations, Webster and Shang[130] simulated the vortex breakdown over a 70° delta wing at 33° angle of attack. Their results showed the breakdown appeared to be a bubble type in the time average flow field, but it seemed the instantaneous flow field was the spiral type.

In 1993, O. Kandil, H. Kandil and Liu[49] presented the vortex breakdown in transonic flows for the first time over a 65° cropped delta wing by solving the full Navier-Stokes equations. The angle of attack, Mach number and Reynolds number were 20°, 0.85 and 3.23×10^6, respectively. A λ-type shock system and a transverse terminating shock were captured on the upper surface of the delta wing. The leading edge vortex

breakdown to a two-bubble cell behind the terminating shock. As the Mach number increased from 0.85 to 0.9, the terminating shock moved downstream and the size of breakdown region reduced. As the angle of attack increases from 20° to 24°, the shock moved upstream and the size of breakdown region expanded.[47]

In 1994, Ekaterinaris and Schiff[17] simulated the vortex breakdown over a delta wing by solving the thin-layer compressible Navier-Stokes equations with embedded grid. They found the main effect of turbulence modeling was the change of the vorticity in the vortex feeding sheets and hence changed the location of the breakdown and the size of the breakdown region. The computed results showed a progression from no breakdown to steady bubble type breakdown to unsteady spiral type breakdown as the angle of attack was increased.

In 1995, Visbal[125] studied the onset of breakdown in the leading edge vortices above a 75° delta wing under a low Reynolds number. Results showed when the angle of attack was larger than a critical value, even a small increase in angle of attack would induce breakdown. When the bubble type breakdown moved upstream on to the wing, it would lose stability and transform to a helical type breakdown.

In 1996, when applying a two-equation (k-ε) turbulence model in a numerical simulation of vortex breakdown over a delta wing, Rizzetta[104] found the k-ε model gave too much turbulent dissipation and enlarged weak vortices with no breakdown.

In 1999, Görtz and Rzzi[29] investigated the effects of wing thickness, viscosity, turbulence model, numerical scheme and grid refinement on the vortical flow and on vortex breakdown by solving Euler and Navier-Stokes equations. They found that model thickness had an influence on integrated forces, but had a minimal effect on the location of the vortex breakdown at fairly high Reynolds numbers. The breakdown locations appeared to depend on the different numerical schemes — Roe's upwind scheme predicted a more upstream breakdown position than the central scheme. They also noticed the sensitivity of the numerical solution to the fineness of the grid in apex region.

2.3 Tail Buffeting

Buffeting refers to an irregular motion of any parts of aircraft under aerodynamic loads. It is a structural response problem due to the forced vibration when the frequencies of aerodynamic loads excited by the flow turbulence are commensurate with the natural frequencies of the structure. This phenomenon not only decreases the fatigue life of the aircraft structure, but also limits the angle of attack envelope of the aircraft.

2.3.1 Discovery of Tail-Buffet Phenomenon

The investigation of tail-buffet phenomenon was originated in connection with the deadly crash of the Junkers-F13 commercial airplane at Meopham, England on July 21, 1930. Eye witnesses reported seeing the airplane enter a cloud, suddenly hearing a loud noise and then seeing parts of the aircraft fall to the ground. The unusual circumstances of the accident led scientific organizations in England and Germany to undertake detailed investigations of the possible causes. The British Aeronautical Research Committee concluded that the most probable cause of the accident was "buffeting" of the tail. The aircraft had been drawn upward by a region of strong rising gust, which caused the angle of attack to increase sharply, resulting in massive flow separation over the wing. The highly turbulent wake flow passed over the tail resulting in severe vibrations of the tail unit, in which the stabilizer bent rapidly up and down and the elevator moved in an erratic manner. The term buffeting was first used by the British investigations to name this phenomenon.[23]

Liepmann[79] pointed out that since buffeting is the response of an elastic body to a turbulent flow, and hence it is a stochastic process. He suggested that a correct theory of buffeting must account for the turbulent characteristics of the oncoming flow and statistical methods are therefore appropriate for the analysis of buffeting. He concluded that the use of power spectrum concept for the motion of air, and the impedance concepts for the aerodynamic and elastic response could make the analysis relatively simple.

2.3.2 Experimental Investigations of Tail Buffet

Experimental investigations have been massively conducted from the beginning of buffet research. The British Aeronautical Research Committee used wind-tunnel-model to investigate the cause of Meopham accident[23]. They found at large angles of

attack the tail, situated in the wing wake, was subjected to intense forced vibrations caused by the turbulences in the separated flow, which brought about the accident. At the same time, German scientists Blenk, Hertel and Thalau conducted a series of laboratory and flight test[23]. These investigations show that it was possible for the tail to buffet. But in usual flight, except during a steep dive, buffeting intensity was not sufficient to cause the structural failure. They concluded that the Meopham accident was probably caused by high gust or maneuvering load.

Duncan and his associates[15] investigated the buffet by using an airfoil, which created the disturbances, and a "detector" which was made movable to investigate the whole region behind the airfoil. The detector's oscillations, equaling to buffeting intensity, were recorded. The width of the wake was obtained by using a total head tube. They noted the buffeting intensity contours did not coincide with the total head wake.

This early research showed that tail buffeting was a result of flow separation. Tail buffeting could be prevented by preventing flow separation, by boundary layer control or by locating the tail outside of the disturbance region[23]. However, for modern aircraft, especially fighter aircraft, which use vortex generated lift and often is often operating at high angle of attack in combat maneuvers, flow separation and high intensive turbulent flow are inevitable and can cause a very serious problem of tail buffeting. So experimental investigations of the vertical tail buffet have been conducted by many researchers in the past two decades.

Triplett (1984)[123] conducted a wind tunnel studies on a 13%-scale F-15 model. He observed that there were large vibrations of the vertical tails during simulated combat maneuvers at high angles of attack. He suggested the tail flexibility had a significant effect on the unsteady pressures on the tails. He concluded the tails were mainly oscillating in the first torsion mode.

Lee and Brown (1990)[74] investigated tail buffet on the vertical fin of a rigid 6% model of the F/A-18. They found that there was a large increase in the unsteady pressure fluctuations on the upper surface of the LEX at high angle of attack above 25 degrees. The low-pressure region was located outboard of the fins at high angle of attack. The LEX fence had a small influence on the steady balance measurements, such as lift and

pitching moment. However, unsteady quantities were reduced with the fence on. At $\alpha =$ 30°, there were large reductions in steady and unsteady pressures on the vertical tail inboard with fence on.

In 1993, Washburn, Jenkins and Ferman[129] conducted extensive investigation on vortex breakdown induced tail buffeting by using a 76° delta wing with twin tails. The vertical tails were placed at nine locations. The results showed the change of chord wise tail location had a bigger influence on the aerodynamic loads than the change of span wise tail location. The buffeting response decreased as the tails were moved towards the vortex core. It also showed that the vortex breakdown was influenced by the tail location, but the core trajectories upstream of the tail were not. The results also showed a flexible tail could affect the unsteady pressure on a rigid tail located on the other side of the model.

Meyn and James (1993)[85] conducted tail buffet studies on a full-scale, production F/A-18 fighter aircraft. They found the LEX fence significantly reduced RMS bending moment, peak PSD bending moment, RMS pressure and peak PSD pressure. But the LEX fence only had a small effect on the peak power frequencies. Non-dimensional peak power frequencies measured in small-scale model agreed well with the full-scale model, but the non-dimensional RMS pressures measured on the full-scale aircraft were larger than those measured in small-scale tests for angles of attack less than 40°. The full-scale power spectra had more power in the frequencies below the peak power frequency. However, the agreement was good for power spectra for both models.

Lee and Tang (1994)[75] conducted a wind tunnel test on a rigid 6%-scale F/A-18 model. They found the RMS values of the unsteady pressure fluctuations increased with increasing angle of attack on both surfaces. Spectral analyses of the vertical fin buffet loads showed a broad peak at a value of reduced frequency decreased with the increase of angle of attack. The probability density function of the buffet load showed that it had a Gaussian distribution at $\alpha = 25°$ and there was a small deviation from the Gaussian profile when the angle of attack was increased.

Pettit, et al. (1994)[98] also conducted a full-scale, production model F/A-18 in wind tunnel. The LEX fence was shown to effectively reduce the RMS root bending

moments and the corresponding spectral levels when the angle of attack was less than 32° and the sideslip was zero. Higher angles of attack reduced the benefits of the LEX fence and caused the buffet pressures to be concentrated in a narrow, low frequency band. Sideslip had a small effect on the frequency of peak buffet excitation. The changes in the LEX fence's effectiveness caused by varying sideslip were less than those caused by altering angle of attack. Cross-spectral densities between the buffet pressures on the inside and outside surface of the fin showed strong coherence and phase relationships at certain locations.

In 1994, Gursul[30] conducted an experiment to investigate the vortex breakdown of delta wings at high angle of attack. He noticed the coherent pressure fluctuations were due to the helical mode instability of the vortex breakdown flow field. The vortex shedding took the form of symmetric flows and its influence on the unsteady pressure fluctuations was negligible. Measured unsteady pressure at different stream wise locations on the wing surface showed the dimensionless frequency $f\,x/U_\infty$ was close to constant at a fixed angle of attack and sweep angle, which implied increasing wavelength in the stream wise direction. For different wings, the nondimensional frequency was a function of nondimensional circulation $\Gamma/U_\infty x$ only. At a fixed stream wise location, the wavelength of the disturbances and the core radius increased with the nondimensional circulation.

Moses and Pendleton (1996)[91] conducted a comparison of pressure measurements between a full-scale and a 1/6-scale F/A-18 twin tail during buffet. The comparison revealed similarities in the trends of the spectral content as a function of angle of attack. At same station the phase between inboard and outboard was nearly same for both models. So the phase of differential unsteady pressures between two stations on the 1/6-scale model might be scaled up to identically located stations on the full-scale model by using the scaling relationship. They confirmed the effectiveness of LEX fence on reducing buffet load for angle of attack up to 32°.

In 1998, Moses and Ashley[92] investigated the spatial characteristics of the unsteady differential pressures on rigid and flexible tails of a 16% F/A-18 wind tunnel model at buffet loading conditions. Results of the cross correlation and cross spectral

analyses of the pressure time histories showed the unsteady differential pressures were not fully correlated and resembled a wave that traveled along the tails. The pressure correlation varied with flight speed at a constant angle of attack. The results of rigid tail and flexible tail were similar and showed the tail flexibility did not affect the time delays or the phase delays of the unsteady differential pressures.

2.3.3 Numerical Investigations of Tail Buffet

With the fast development of computer memory and speed, CFD became a more powerful tool for physical simulations. However, the cost of computational simulations of the tail buffet problem, which includes turbulence modeling, flow-structure coupling and time accurate computation, is still high. Edwards[16] estimated that the computer speed would have to increase by three orders of magnitude to make the full aircraft simulations practical. His estimates were based on the requirement of tail buffet simulation of full F-15 aircraft and 40 μsec/grid cell/time step using thin layer Navier-Stokes solver. So, a simple model that isolates the characteristics of the tail buffet phenomenon from the whole aircraft is needed. The group led by Dr. O. A. Kandil[48, 51] investigated the tail buffet, including strong coupling between the flow and structure, by using a simplified delta wing/tail model.

In, Rizk, Guruswamy and Gee (1992)[102, 103] investigated the buffet problem of F/A-18 aircraft at 30° angle of attack by solving the Reynolds-averaged, thin layer Navier-Stokes equations. A Chimera type grid consisting of 0.9 million cells was used to simulate the symmetric half of the aircraft. To save computational cost, the tails were assumed to be rigid. So only weak coupling between aerodynamics and structures was considered in this simulation. The significant effects of flexible tails on the unsteady pressure loading of the tails had been demonstrated by an experiment.[129] They concluded that the main response of tail was in the first bending mode.

In 1993, O. Kandil and Flanagan[48] conducted a successful buffet simulation on a single tail model, which consisted of a single flexible cantilevered tail placed in a circular duct. The inlet swirling flow was forced to breakdown by the interaction of supersonic swirling flow and a shock at the inlet of the duct. The unsteady, compressible, full Navier-Stokes equations with the assumption of quasi-axial symmetry were solved. The

tail reached periodic response in short time and the frequency of the bending oscillation was about 20.94.

In 1993, O. Kandil, H. Kandil and Massey[50] presented another successful tail buffet simulation on the model of a 76° sharp edge delta wing and a single flexible rectangular vertical tail. The tail was treated as cantilevered beam and allowed to oscillate in bending mode. The torsion aerodynamic loading was neglected. The results showed the response of the tail was primarily in the first bending mode. The results also showed the effects of the tail location, shape and deflection on the flow field upstream of the tail.

O. Kandil, Massey and H. Kandil (1994)[51] and O. Kandil, Massey and Sheta (1995)[52] developed the model used in Ref [50] by considering both bending mode and torsional mode of the tail. The coupled bending-torsion case showed one order of magnitude higher on the deflection and loads than those of bending only cases. The results also showed the vortex breakdown location and the unsteady pressure on wing and tails were affected by the motion of the tail. The coupled bending and torsion response was nearly twice as large as that of the uncoupled case.

In 1995, Gee, Murman and Schiff[25] made an improved CFD analyses based on previous work[102, 103] by using a refined grid system and computing longer time histories. Total 1.7 million grid points were used and the time histories were up to 1s of real time. When compared with experimental data, the RMS pressure on the vertical tail inboard and outboard surface as well as the power content of the unsteady differential pressure were predicted. Also, the CFD results accurately predicted the effects of the LEX fence, with the inclusion of the fence reducing the magnitude of the aerodynamic loads acted on the vertical tail. Such results indicated that CFD methods could be used to predict tail buffet loads, given sufficient grid resolution in sensitive regions.[25]

In 1995, O. Kandil, Sheta and Massey[59] investigated effects of angles of attack on the tail buffet in transonic flow. The computational model consisted of a single swept-back vertical tail placed at 6% wing-chord downstream of the wing trailing edge and a 65° swept-back, sharp edged, cropped delta wing. Results showed that the vortex breakdown became stronger, the normal forces and torsion moments became larger, the

change in either case. They concluded that the apex flap was an efficient and harmless method for delaying vortex breakdown without increasing the level of tail buffet.

In 2001, Sheta, Rock and Huttsell[117] presented a time-accurate computational investigation of the vertical tail buffet of the F/A-18 aircraft at typical flight conditions. The computed results accurately predicted the RMS of the differential pressure, RMS pressure on the inboard and outboard surface of the tails and the RMS of tail root bending moment. The predominant frequencies of the pressure and the PSD peak of the differential pressure spectra were also predicted accurately. The vertical tail was responding mainly in the first bending mode. The strong coupling between the fluid and structure produced more accurate results than the weak coupling.

2.4 Active Flow Control

Flow control can improve aerodynamic performance and is one of major aerodynamics research areas. Flow control is classified into passive flow control, such as aerodynamic shaping, wing flaps, vortex generators, etc., and active flow control, such as blowing, suction, etc. With the development of micro electromechanical systems (MEMS), more powerful tools can be used to control flow. By integrating microprocessors and MEMS, including arrays of sensors and actuators, flow controls become smarter, or more *active and adaptive*. Recently, there are many researches on the flow control applications of MEMS-based synthetic jet and vortex actuator.

2.4.1 Blowing and Suction

In 1992, Craig[13] investigated computationally to the tangential leading edge blowing (TLEB) on a rounded leading-edge 60-degree delta wing at a high angle of attack by solving the thin layer Navier-Stokes equations. The Baldwin-Lomax algebraic turbulence model was used in his simulation. The computational results demonstrated the effectiveness of blowing as a way to provide roll control at high angles of attack. The saturation effect of increased blowing was also captured well in the computations.

In 1995, O. Kandil, Sharaf El-Din and Liu[55] investigated two active control methods — flow injection and surface heating — for asymmetric flows around circular cones by solving the unsteady compressible full Navier-Stokes equations. The locally

conical flow assumptions had been used in the simulations to save computational time. The injected mass-flow rate was proportional to the surface pressure difference between the left and right side of the cone. A hybrid flow control method of flow injection and surface heating was also studied. The results showed the normal injection alone lost its effectiveness at high angle of attack. However, the surface heating still worked at very high angles of attack. The hybrid method showed superior control effectiveness.

In 1995, O. Kandil, Sharaf El-Din and Liu[56] investigated numerically to the effectiveness of the active control using flow injection on a slender pointed cone by solving the three-dimensional thin-layer Navier-Stokes equations. Normal and tangential flow injection were applied. The injection angle, injection port length and maximum mass flow rate were specified. The maximum mass flow was proportional to the pressure difference between the right and left side of the cone. The computational results showed the flow had recovered its symmetry after the normal or tangential injection control was applied. They also found the tangential injection control was more effective than the normal injection control.

In 1996, Pedreiro, Rock, Celik and Roberts[97] conducted an experiment to investigate the forebody tangential blowing (FTB). They demonstrated that FTB could control the roll-yaw motion of a delta wing-body model. It was shown that asymmetric blowing was a highly non-linear effecter that could be linearized by superimposing symmetric blowing. They noticed the flow structure over wing-body combination at 45° angle of attack was asymmetric. Asymmetric FTB could increase the flow asymmetry or invert it depending on which side of the model blowing was applied. The asymmetry could also be inverted by a change in roll angle.

In 1996, O'Rourke, Ralston, Kloc and Langan[94] investigated a conformal pneumatic control device employing tangential slot blowing. Results showed that the device provided effective levels of yaw control on a realistic configuration representative of future fighters. A parametric investigation on forebody cross-section, device location, device orientation and different slot and jet geometries was conducted. The optimum configuration was found to be tangential slot blowing located at the near the apex of the forebody blowing forward and inboard, across the nose. This configuration was tested at

different blowing levels, sideslip angles and rotation rates. In all cases it was found to be robust and controllable and the response indicated little or no control lags.

In 1997, O. Kandil and Menzies[54] developed a control system to control the wing rock. The unsteady, compressible, full Navier-Stokes equations and the Euler equations of rigid-body dynamics were solved to simulate the delta wing rock phenomenon. An active control model using a mass injection system was applied from wing surface to suppress the limit-cycle oscillation of the wing. The control law was based on the feedback of the roll angle and roll velocity. Results demonstrated the effectiveness of the design.

In 1999, Guy, Morrow and McLaughlin[31] applied periodic blowing and suction at the leading edge of a 70° swept delta wing. A parametric study was conducted at an angle of attack of 40° to search for the optimum working point of the periodic flow actuator. The best effect of the flow excitation was found at a nondimensional frequency of 1.2-1.4 and at an oscillatory momentum coefficient of 0.0045. Velocity surveys showed the flow excitation increased velocities close to the wing and across the vortex after the onset of vortex breakdown. The effect of periodic blowing and suction was experimentally demonstrated which showed the vortex breakdown was delayed as much as 0.2 chord length.

2.4.2 Synthetic Jet Actuator

The synthetic jet actuator is also called zero mass jet actuator because the jet is formed without net mass injection across the system boundary. Figure 2.6 shows a sketch of synthetic jet. It consists of an enclosed rigid cavity with a small orifice and a movable diaphragm. When the diaphragm is driven by a piezoelectric actuator, the fluid is periodically blown out and drawn into the cavity through the orifice, generating a jet with a train of counter rotating vortex pairs that are produced at the edge of the orifice. As one of the most useful micro fluid devices, the potential application of synthetic jet includes thrust vectoring of jet engines[118], mixing enhancement[12] and active control of separation and turbulence in boundary layer.[3]

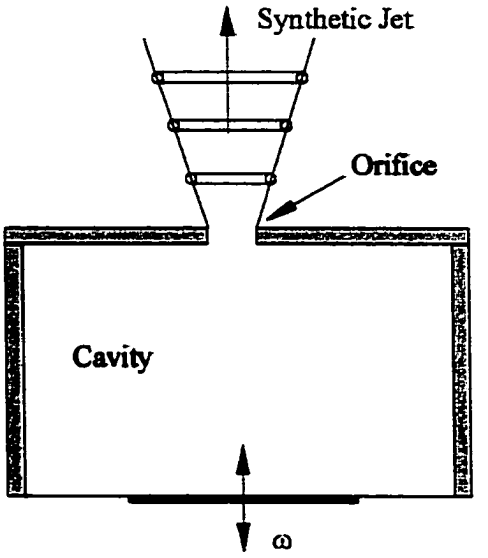

Figure 2.6 Schematic of synthetic jet.

In 1997, B. Smith and Glezer[118] investigated the flow characteristic of high ratio synthetic jet actuators. The experimental results showed that a unique feature of synthetic jets was the capability of transferring linear momentum to the flow system without net mass injection across the system boundary. The application of synthetic jest to thrust vectoring and direct excitation of small-scale motions in a conventional jet was also investigated. The primary jet could be vectored either toward or away from the actuator jets at angle of 30° to 80°. The actuation frequency was at least an order of magnitude higher than the unstable frequency and thus resulted in direct excitation of small-scale motions and enhanced turbulent dissipation.

In 1997, Kral, Donovan, Cain and Cary[68] investigated the synthetic jet by solving the two-dimensional, incompressible Navier-Stokes equations with the Spalart-Allmaras turbulence model. The computational domain did not include the cavity and the diaphragm. The actuator was represented by a suction/blowing boundary condition along the orifice. The turbulent synthetic simulations showed a pair of counter-rotating vortices, the quick diffusion of these vortices due to the turbulence and good agreement with the experiments of Smith and Glezer.[118]

In 1997, Hassan and JanakiRam[34] conducted a numerical study to investigate the effect of an array of synthetic jets on the aerodynamic characteristics of the NACA-0012

airfoil. The results suggested the synthetic jets with the careful selection of their peak amplitude and oscillation frequency could enhance the lift characteristics of airfoils. The results also showed that the synthetic jet for a helicopter blade could alter the pressure distribution near the blade's leading edge and hence lower blade-vortex interaction (BVI) noise levels. They found the ratio between the jet peak velocity to the external flow velocity was an important parameter.

In 1998, Cain, Kral, Donovan and D. Smith[10] presented the first set of simulations of high-speed synthetic jets. The results showed a near sonic jet, both primary and forcing jets were near sonic, was capable of an amazing mixing enhancement. To examine the effects of turbulence model on the synthetic jet simulation. Spalart Allmars one equation model and Menter blended k-ω/k-ε shear stress transport model were used in computation. The results showed the influence of the turbulence model is almost negligible.

In 1998, Smith and Glezer[119] investigated the formation and evolution of synthetic jets. They found that a train of counter-rotating vortex pairs were formed at the edge of an orifice by the periodic motion of a flexible membrane in a sealed cavity. They noted the jet was formed without net mass injection, but the momentum of ejected fluid was nonzero. Each vortex pair developed a span wise instability and transition to turbulence and became indistinguishable from the mean jet flow. In the far field, the synthetic jets were similar to conventional two-dimensional jets and had higher mean velocity decrease in stream wise centerline direction.

In 1998, Rizzetta, Visbal and Stanek[105] investigated a three-dimensional synthetic jet by using a Direct Numerical Simulation (DNS) approach. Several two-dimensional cases were also investigated. The interior flow was computed on an overset deformation grid and the jet flow was simulated by a high-order compact finite difference scheme. The depth of the cavity and the Reynolds number were found to be important parameters. The three-dimensional computation indicated that the external flow breakdown into turbulence resulting of span wise instabilities.

In 1998, Hassan[35] conducted numerical studies to investigate the beneficial effects of an array(s) of zero-mass jets. Results were shown the lift enhancement and emulation

of the aerodynamic effects resulted from a mechanical trailing edge flap. Two arrays of zero mass jets were used on rotor/proprotor blades to alter the local pressure distribution and decrease noise levels of the blade vortex interaction (BVI).

In 1998, Amitay, D. Smith, Kibens, Parekh and Glezer[2] conducted flow control in wind tunnel experiments on a two-dimensional cylinder and a two-dimensional thick airfoil by using synthetic jet. Their experiments showed the effects of synthetic jets on the pressure distribution around the models resulting in the substantial lift increases and drag reductions. The transient mechanisms of the lift force as a result of a step change in the control input was investigated using phase-locked velocity measurement in the wake.

In 2000, Lee and Goldstein[77] conducted direct numerical simulation of an array of two-dimensional synthetic jets. A virtual solid boundary condition, which imposed a localized body force along desired points in the computational mesh to bring the fluid there to a specified velocity so that the force had the same effect as a solid boundary, was used in the simulation. Results suggested the jet formation was highly sensitive to the flow Reynolds number and jet evolution was affected by Strouhal number. They also conducted the investigation on the geometry and found the shape of lip and the depth of the cavity were important parameters in the resulting flow.

In 2000, Amitay, Pitt, Kibens, Parekh and Glezer[3] demonstrated flow control for internal flows by using an array of synthetic jets. A two-dimensional serpentine duct model with three configurations was used to generate separation bubble or complete separation. The Mach number of the flow in duct was less than 0.3 and the array momentum coefficient C_μ was about $O(10^{-4})$. The results showed the separation flow was reattached when arrays of synthetic jets were placed downstream of the separation point. Flow reattachment reduced the losses within the duct and increased the volume flow rate.

In 2001, Chatlynne, Rumigny, Amitay and Glezer[11] investigated the modification of the aerodynamic shape of a two-dimensional Clark-Y airfoil in wind tunnel experiments. A low-$C\mu$ synthetic jet actuator was placed downstream from a miniature surface-mounted passive obstruction. The interaction between the actuation and the cross flow resulted in the formation of a small stationary recirculating flow domain near the surface of the airfoil. Results showed a reduction in the magnitude of the pressure within

the recovery domain to the trailing edge and resulted in reductions in the pressure drag and relatively small reductions in lift.

In 2001, Mittal, Rampunggoon and Udaykumar[88] investigated the interaction of a modeled synthetic jet with a flat plate boundary layer by using an incompressible Navier-Stokes solver. The motion membrane is modeled as a moving boundary in order to accurately compute the flow inside the cavity. The simulations showed that the presence of the cross flow resulted in a significantly different flow because of the dynamics of the vortex structures produced by the jets. The results also showed the skewness might be an important characteristic of the jet profile. The virtual aero-shaping effect of the synthetic jet was investigated. Large mean recirculation bubbles were formed in the external boundary layer when the jet velocity was much higher than the cross flow velocity.

In 2001, B. Smith and Swift[120] investigated synthetic jets and similar continuous jets by experimental measurements and flow visualization. The results showed no synthetic jet was formed if dimensionless stroke length L_o/h was less than one threshold value. As L_o/h was increased beyond the threshold value, the vortex pair escaped the influence of the suction stroke and resulted in the increase of jet momentum. Synthetic jets with large stroke lengths had more small-scale motions than similar Reynolds number jets with the smaller stroke lengths. A synthetic jet bears much resemblance to a continuous jet in the far field, but a synthetic jet entrained more fluid and grown faster than a continuous jet in the near field. Reynolds number affected the transition of the flow exiting the nozzle, the transition of the vortex pair and the turbulent characteristics of the developed jet flow. The far field behavior of synthetic jets appeared to be a function of both Reynolds number and stroke length.

2.4.3 Jet and Vortex Actuator (JaVA)

Jet and vortex actuator (JaVA) is similar to a synthetic actuator shown in Figure 2.7. It consists of a cavity and a plate that serves as the actuation surface. A shaker is used to actuate the plate in an oscillation motion. Air is pushed out of the cavity when the plate moves downward and sucked into cavity when the plate moves upward. The plate is placed asymmetrically over the cavity opening, forming narrow and wide gaps, shown in Figure 2.7 (b). Depending on the scaling parameters, JaVA can generate different flows,

such as free jet, wall jet, vortex flow or a combination of these flows. There are massive studies on the synthetic jet actuator, but the researches on the JaVA are relatively less. The author thinks JaVA is more flexible and can generate more flow types compared with synthetic jet actuator. In Chapter 7, the JaVA's characteristics and applications on flow separation control are investigated.

In 1995, Jacobson and Reynolds[39] developed an actuator that consisted of a pizeoelectrically driven cantilever mounted flush and asymmetric in a cavity. When the actuator is driven, flow disturbance over the actuator is a quasi-steady pair of counter rotating stream wise vortices. The actuator is fast, controllable and do not need a fluid source (zero net mass). It is compact by using planar micro electromechanical systems (MEMS) and generates a substantial disturbance in the flow. Its performance was demonstrated in a laminar boundary layer flow.

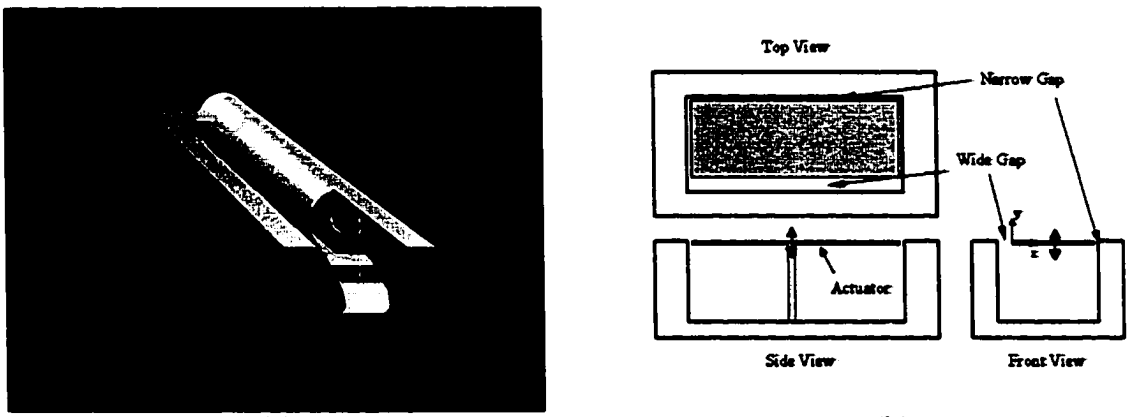

(a) (b)

Figure 2.7 A 3D model (a)[138] and a sketch (b) of Jet and Vortex Actuator (JaVA).

In 1995, Koumoutsakos[67] conducted direct numerical simulations to investigate the active vortex actuators without external flow, which had been experimentally studied by Jacobson and Reynolds[38], and Saddoughi.[110] An adaptive computational scheme, based on the vortex methods, was used to solve the two-dimensional incompressible unsteady flow. The simulations had shown a dramatic difference in the flow behavior for various parameters of the configuration. Two types of flows were observed computationally and experimentally. Type I, the periodic jet developed from the narrow gap at relatively low amplitudes and high frequencies; Type II, the periodic jet developed from the wide gap at relatively high amplitudes and low frequencies.

In 1998, Lachowicz, Yao and Wlezien[80] conducted experiments to characterize jet and vortex actuators in still air. They concluded the JaVA could generate three primary flow regimes — wall jet, free jet and vortex flow — depending on scaled amplitude, actuator Reynolds number and gap spacing. For the vortex flow, they noticed the actuator operational range increased as the size of the actuator decreased. Then they suggested for the first time that micro-size actuators might provide a larger operational range than macro-size actuators. The optimum actuator efficiency occurred at a Stokes number of about 8 for the vortex flow.

In 1998, Joslin, Lachowicz and Yao[40] simulated the flow induced by the jet and vortex actuator (JaVA). Direction numerical simulation was used to solve unsteady, incompressible Navier-Stokes equations. The cavity was not included in computational domain. A velocity profile was used to represent the flow in the gaps and motion of the oscillating plate. The computational results showed a vortex structure with approximately the same size as the experiments. The amplitudes of the tangential velocities were smaller than the measured values.

In 1999, Kandil, Yang and Lachowicz[65] simulated the JaVA induced flow using incompressible Navier-Stokes equations. Two types of flow modes, a vortex mode and a free jet mode, were presented and had good agreement with experimental data.

2.5 Buffeting Alleviation

Because of the destructive effects of tail buffet, many researchers investigated how to alleviate the tail buffet. The buffet phenomenon is structural forced vibration excited by the aerodynamic loading. Change of structure characteristic or flow characteristic could control the buffet. The methods that alleviate tail buffet can be classified as structure control and flow control.

2.5.1 Buffeting Alleviation by Structure Control

Hauch, Jacobs and Dima (1995)[32] developed an Active Vertical Tail to alleviate the tail buffet by using piezoelectric actuators, strain gage sensors and simple control techniques. Moses (1999)[93] presented the research work of the NASA Langley research center in buffeting alleviation by active control of smart materials. LaRC was conducting

wind tunnel tests of new piezoelectric actuators to demonstrate their effectiveness under specific load conditions. However, there are penalties on weight to get effective control by using piezoelectric actuator.

2.5.2 Buffeting Alleviation by Flow Control

Bean, Greenwell and Wood (1992)[5] and Bean and Wood (1993)[6] studied the application of suppressing single bin buffet by tangential leading edge blowing (TLEB). The buffet suppression was achieved at any angle of attack in the testing. Symmetric TLEB induces a linear shift in the buffeting response and the wing stall angle. It was found that a tapering slot was almost twice as efficient at modifying vortex behavior, and therefore, suppressing fin buffeting, compared to a parallel slot. The maximum response was characterized by both leading edge vortex shear layers impinging on the fin leading edge and tip. It has been shown that the frequency content of the excitation flow field is a function of freestream velocity and angle of attack. Mass flow requirements for TLEB are comparable to short takeoff vertical landing reaction control system; for a modern combat aircraft at low speeds typical of a high angle of attack flight, a total C_μ of 0.1 corresponds to about 10% of compressor mass flow.

In 1996, Pettit et al.[98] and Meyn et al.[85] applied the leading edge extension (LEX) fences to alleviate the tail buffet. The LEX fence is shown in Figure 2.8. The LEX fences could reduce the tail buffet excitation for the angle of attack up to 32°.

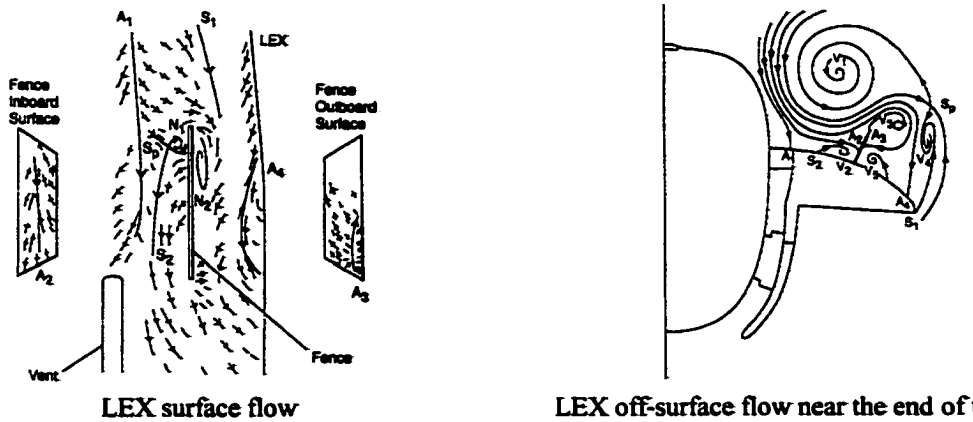

LEX surface flow LEX off-surface flow near the end of the fence

Figure 2.8 LEX fence at $M_\infty = 0.6$ and $\alpha = 30°$.[76]

In 1999, Kandil, Yang and Sheta[62] investigated the tail buffet alleviation by using flow suction along the vortex cores (FSVC). The results showed that the root bending and

twisting momentums were reduced. The frequencies at the peaks of the power spectral density responses did not shift. A parametric study about the location of suction and direction of the suction tube was conducted. The best control results were obtained when the suction tubes were placed near the tail with tilted direction of -10°.

In 1999, Kandil and Yang[63, 64] developed a new adaptive flow control for twin-tail buffet alleviation. Control ports were placed at certain locations of the tail inner and outer surface. The suction and blowing volume flow rate at each port was proportional to the pressure difference between the inner and outer tail surface at each location. A parametric study of the effects of the number and location of these control ports on the buffet response including their control effectiveness at different angle of attack was carried out. The bending and rotation angle responses did not change their sign. The power spectral densities of the root bending momentum and root twisting momentum showed substantial reduction of more than 70%.

In 1999, Flynn, Morrison and Mabey[22] conducted experiment to investigate buffet alleviation on an un-swept wing at high incidence. Results showed that a permeable surface vented to an otherwise airtight plenum, adjacent to an unsteady separation, reduced the severity of the buffet excitation. However, the separation produced "stall cells." Qualitative evidence suggested that the buffet excitation increased rapidly when the size of the stall cell approximately doubled. It also showed that the position of the permeable surface was moved to follow the mean separation line. If the permeable surface was placed under attached flow in a region of large favorable pressure gradient, separation could occur further upstream and lead to an increase of buffet excitation.

2.6 Highly Accurate Numerical Simulation for Complex Unsteady Flows

Fast increases in speed and storage of computer make computational fluid dynamics (CFD) an effective tool for performing design and understanding the nature of flow. The nonlinear partial differential equations that describe flow dynamics are solved numerically in a computational grid to simulate a flow field. Turbulence, usually referred to high frequency and small random amplitude fluctuations, are characteristics of such flow. Averaged governing equations are often used; therefore, the turbulence properties

are not calculated directly and models need to be incorporated in the governing equations to account for turbulence's effects. Most turbulence models function reasonably well for a wide range of flow conditions. However, all turbulence models eventually fail when the fluid state becomes sufficiently intricate. The use of time-averaged flow equations neglects the effects of high frequency phenomena, which are often the important considerations of aero-acoustics, combustion, buffet, flutter and other fluid related interactions.[107]

As an alternate approach to traditional time averaged equations and turbulence modeling, direct numerical simulation (DNS) can compute fine scale flow details directly. But DNS requires huge computational resources because the mesh should fine enough to capture the smallest scales in the flow. Only the calculations to simple geometric configurations can be done. By modeling the smallest turbulent structures with a sub-grid model (SGS), Large-Eddy Simulation (LES) only simulate the large scales of turbulent structures. LES can be more accurate than RANS and need much less computer time than DNS.

In 1992, Lele[78] presented and analyzed compact finite difference schemes for the evaluation of derivatives, interpolation and filtering. The new schemes improved the representation of a range of wave numbers rather than accurate resolution of a single wave number. The schemes might be used on non-uniform meshes and a variety of boundary conditions might be imposed. The family of schemes presented reduced to the Padé schemes if the constraint of maximal formal accuracy with a specified computational stencil was imposed. Their improved resolution with spectral-like behavior had been demonstrated in a variety of applications.

In 1992, Poinsot and Lele[99] discussed the boundary conditions for Navier-Stokes equations. The boundary conditions using characteristic wave relations and compatible with non-dissipative scheme were derived. Reflecting and non-reflection boundary condition treatments were presented. Implementation for inlet, outlet boundary conditions and slip, non-slip walls were presented.

In 2000, Visbal and Gordnier[126,127] solved the three dimensional, unsteady Navier-Stokes equations on dynamic meshes by high-order compact schemes. Padé type spatial

discretizations up to sixth order and low-pass filters up to tenth order were applied. Time integration method were the explicit forth order Runge-Kutta method, which was suitable for wave propagation, and implicit sub-iterative second order approximately-factored method, which was suitable for wall-bounded flow simulations. The numerical metrics were treated with strong conservation form to eliminate metric-cancellation errors. The second order temporal approximation was used to compute the grid speed. This high order scheme showed superior accuracy over standard second order scheme on severely distorted dynamic meshes.

CHAPTER 3: FORMULATION AND COMPUTATIONAL SCHEMES

3.1 Introduction

The research focus deals with multidisciplinary type problems. In this study, modeling of flow-structure interaction problems is investigated. Three sets of governing equations need to be used. They are: the unsteady, compressible, full Navier-Stokes equations; the aeroelastic equations for coupled bending and torsion vibration of cantilevered tails; and the equations for moving grid due to the deflection of tails.

This chapter is organized as follows: First, the flow equations, the computational fluid dynamics formulation, including Roe's 2nd order upwind scheme and boundary and initial conditions for the flow field are presented. Then, the elastic equations, the computational structural formulation and structural initial and boundary conditions are presented. Next, the grid displacement equations are presented. The method of solution is presented at the end of the chapter.

3.2 Fluid Flow Dynamics Equations

The dimensionless, unsteady, compressible Navier-Stokes equations in conservative form are given by

$$\frac{\partial \bar{Q}}{\partial t}+\frac{\partial \bar{E}_j}{\partial \xi_j}=\frac{\partial (\bar{E}_v)_j}{\partial \xi_j}, \qquad j=1, 2, 3 \tag{3.1}$$

The flow field vector $\bar{Q}$, inviscid flux $\bar{E}_j$ and viscous flux $(\bar{E}_v)_j$ are given by

$$\begin{aligned} \bar{Q} &= \frac{Q}{J} \\ \bar{E}_j &= \frac{1}{J}\left((\xi_j)_t Q + (\xi_j)_k E_k\right) \\ (\bar{E}_v)_j &= \frac{1}{J}(\xi_j)_k (E_v)_k \end{aligned} \tag{3.2}$$

where Q is the flow vector in the Cartesian coordinates, and J is the Jacobian of the transformation from the Cartesian coordinates to the body-conformed coordinates. E_k are

the inviscid flux vectors in Cartesian coordinates and $(E_v)_k$ are viscous and heat conduction fluxes vectors in Cartesian coordinates. They are given by

$$J=\frac{\partial(\xi_1,\xi_2,\xi_3,t)}{\partial(x_1,x_2,x_3,t)},\ Q=\begin{bmatrix}\rho\\ \rho u_1\\ \rho u_2\\ \rho u_3\\ \rho e\end{bmatrix},\ E_k=\begin{bmatrix}\rho u_k\\ \rho u_1u_k+\delta_{1k}p\\ \rho u_2u_k+\delta_{2k}p\\ \rho u_3u_k+\delta_{3k}p\\ \rho u_k(e+\frac{p}{\rho})\end{bmatrix},\ (E_v)_k=\begin{bmatrix}0\\ \tau_{k1}\\ \tau_{k2}\\ \tau_{k3}\\ u_n\tau_{kn}-q_k\end{bmatrix} \tag{3.3}$$

where τ_{kn} is the shear stress tensor. For Newtonian fluids with the Stokes's hypothesis, $\lambda=-\frac{2}{3}\mu$, τ_{kn} is given by

$$\tau_{kn}=\frac{\mu M_\infty}{Re}\left(\frac{\partial u_k}{\partial x_n}+\frac{\partial u_n}{\partial x_k}-\frac{2}{3}\delta_{kn}\frac{\partial u_m}{\partial x_m}\right) \tag{3.4}$$

and the heat conduction flux, q_k, is given by

$$q_k=\frac{-\mu M_\infty}{(\gamma-1)\,Pr\,Re}\frac{\partial T}{\partial x_k} \tag{3.5}$$

The variables in Equation (3.1) – (3.5) are non-dimensionalized by using the reference parameters. The reference parameters are $L, a_\infty, L/a_\infty, \rho_\infty$ and μ_∞ for the length, velocity, time, density and molecular viscosity, respectively. The pressure is non-dimensionlized by $\rho_\infty a_\infty^2$. The freestream Reynolds number is defined by $Re=\frac{\rho_\infty U_\infty L}{\mu_\infty}$ and the Prandtl number, $Pr=\frac{\mu C_p}{k}$, is chosen as 0.72. The dimensionless viscosity is given by Sutherland's law

$$\mu=T^{\frac{3}{2}}\left(\frac{1+c}{T+c}\right) \tag{3.6}$$

where T is the non-dimensional temperature and c is the Sutherland's constant, $c\approx 110.4/T_\infty$.

3.3 Computational Fluid Dynamics Formulation

The schemes used in computational fluid dynamics include the finite difference scheme and the finite volume scheme. The code used in Chapter 4 and 5 is based on the

Roe's upwind finite volume scheme. The code (PHCC) developed in Chapter 6 is based on the high order compact finite difference scheme. The Roe's upwind finite volume scheme and high order compact finite difference scheme are presented below.

3.3.1 Finite Volume Formulation: Roe's Upwind Scheme

The conservative form of the full Navier-Stokes equations, Equation (3.1), can be integrated over the domain V

$$\int_v \frac{\partial \bar{Q}}{\partial t} dv + \int_v \frac{\partial (\bar{E}_j - (\bar{E}_v)_j)}{\partial \xi_j} dv = 0 \tag{3.7}$$

Applying the Gauss divergence theorem to the second term, the equation above can be rewritten as

$$\int_v \frac{\partial \bar{Q}}{\partial t} dv + \oint_{\partial \Re} \frac{\bar{E}_j - (\bar{E}_v)_j}{J} \bar{a}_m \cdot \hat{n}\, ds = 0 \tag{3.8}$$

where $\bar{a}_m$ is the covariant base vector, $\partial\Re$ the boundary enclosing computational domain V and $\hat{n}$ the unit outward normal of $\partial\Re$.

The flux-difference splitting scheme developed by Roe[108] is based on a characteristics decomposition of the flux differences and posses the conservation properties. Consider the one-dimensional equation

$$\frac{\partial Q}{\partial t} + \frac{\partial E}{\partial x} = 0 \tag{3.9}$$

where E is a function of first order of Q. Using the chain rule, this equation can be written as

$$\frac{\partial Q}{\partial t} + A\frac{\partial Q}{\partial x} = 0 \tag{3.10}$$

where $A = \frac{\partial E}{\partial Q}$ is the flux Jacobian matrix. The exact solution of the Riemann problem can be written as

$$E_R - E_L = \sum_{i=1}^{3} \alpha_i \lambda_i e_i \tag{3.11}$$

where α_i represents the projection of the difference in Q between the initial right and left states, λ_i and e_i are the eigenvalues and eigenvectors of the Jacobian matrix A, respectively. As shown in Ref. 108, the interface flux can be determined using

$$E_{j+\frac{1}{2}}(Q_L,Q_R)=\frac{1}{2}\left(E_L+E_R-\sum_{i=1}^{3}\alpha_i\lambda_i e_i\right) \tag{3.12}$$

Consider the Euler equations, where E is not a linear function of Q, Roe[108] suggested the following form

$$\frac{\partial Q}{\partial t}+\overline{A}\frac{\partial Q}{\partial x}=0 \tag{3.13}$$

where $\overline{A}$ is the Roe-average matrix, which satisfies the following conditions:

1. $\overline{A}$ constitutes a linear mapping from the vector space Q to the vector space E.
2. As $Q_L \to Q_R \to Q$, $\overline{A}(Q_L,Q_R) \to A(Q)$
3. For any Q_L and Q_R, $\overline{A}(Q_L,Q_R)\times(Q_L-Q_R)=E_L-E_R$
4. The eigenvectors of $\overline{A}$ are linearly independent.

Based on the third property, the flux difference between the left and right states and the interface fluxes can be written as

$$E_R-E_L=A(Q_L-Q_R) \tag{3.14}$$

$$E_{j+\frac{1}{2}}(Q_R-Q_L)=\frac{1}{2}\left[(E_L+E_R)-\left|\overline{A}\right|(Q_R-Q_L)\right]_{j+\frac{1}{2}} \tag{3.15}$$

The last term of Equation (3.15) is the dissipation term and can be written as[124]

$$\left|\overline{A}\right|(Q_R-Q_L)=\left|\overline{A}\right|\Delta Q$$

$$=\begin{bmatrix}\alpha_4\\ \tilde{u}_1\alpha_4+\dfrac{\partial\xi}{\partial x_1}\alpha_5+\alpha_6\\ \tilde{u}_2\alpha_4+\dfrac{\partial\xi}{\partial x_2}\alpha_5+\alpha_7\\ \tilde{u}_3\alpha_4+\dfrac{\partial\xi}{\partial x_3}\alpha_5+\alpha_8\\ \tilde{H}\alpha_4+\left(\tilde{\tilde{U}}-\hat{\xi}_t\right)\alpha_5+\tilde{u}_1\alpha_6+\tilde{u}_2\alpha_7+\tilde{u}_3\alpha_8-\left(\dfrac{\tilde{a}^2}{\gamma-1}\right)\alpha_1\end{bmatrix} \tag{3.16}$$

where, J the transformation Jacobian is a function of time on dynamic grids.

Spatial Discretization

To discretize Equation (3.17), the first derivative can be expressed as a linear combination of node values. The compact finite difference schemes in generalization form are

$$\alpha\phi'_{i-1} + \phi'_i + \alpha\phi'_{i+1} = b\frac{\phi_{i+2} - \phi_{i-2}}{4h} + a\frac{\phi_{i+1} - \phi_{i-1}}{2h} \qquad (3.18)$$

where, ϕ can be any scalar function, such as metric or flow variable, h is the grid size. The spatial derivative ϕ' is obtained in the computational plane by solving the tri-diagonal system. The coefficients a, b and α determine the spatial properties of the algorithm. According to Taylor series expansion, the relations between the coefficients a, b and α are

$$a + b = 1 + 2\alpha \quad \text{(2nd order)}$$
$$a + 4b = 6\alpha \quad \text{(4th order)}$$
$$a + 16b = 10\alpha \quad \text{(6th order)}$$

So the different combinations of a, b and α give the different scheme accuracy. Table 3.1 lists several combinations of a, b, and α and correspond truncation error. When α is not zero, the formula yields the compact scheme. When α is equal to zero, the explicit scheme can be obtained.

Table 3.1 Coefficients for spatial discretization at interior points[78]

	α	a	b	Truncation error
Compact 5-point, 6th order, C6	$\frac{1}{3}$	$\frac{14}{9}$	$\frac{1}{9}$	$\frac{4}{7!}h^6\phi^{(7)}$
Compact 3-point, 4th order, C4	$\frac{1}{4}$	$\frac{3}{2}$	0	$\frac{-1}{5!}h^4\phi^{(5)}$
Explicit 5-point, 4th order, E4	0	$\frac{4}{3}$	$-\frac{1}{3}$	$\frac{-4}{5!}h^4\phi^{(5)}$
Explicit 3-point, 2nd order, E2	0	1	0	$\frac{1}{3!}h^2\phi^{(3)}$

To keep the tri-diagonal form of equation, high order one-sided formulas are used at boundary points. For example, at first point Point-1 and at last point Point-N, the derivatives ϕ' are expressed as:[78]

$$\text{Point-1:} \qquad \phi'_1 + C_1\phi'_2 = \sum_{i=1}^{M} c_i\phi_i \tag{3.19}$$

$$\text{Point-N:} \qquad \phi'_N + C_1\phi'_{N-1} = \sum_{i=1}^{M} c_i\phi_{N+1-i}$$

For the second point Point-2 and the Point-N-1, the derivatives ϕ' are expressed as: [78]

$$\text{Point-2:} \qquad C_{21}\phi'_1 + \phi'_2 + C_{22}\phi'_3 = \sum_{i=1}^{M} d_i\phi_i \tag{3.20}$$

$$\text{Point-N-1:} \qquad C_{21}\phi'_N + \phi'_{N-1} + C_{22}\phi'_{N-2} = \sum_{i=1}^{M} d_i\phi_{N+1-i}$$

where the coefficients C_1, C_{21}, C_{22}, c_i and d_i are selected to provide the required order at boundary points and keep a minimum stencil size. [78]

Filtering Scheme

Because the compact schemes used here are center-differenced and non-dissipative, filtering is needed to suppress numerical instabilities generated from all sources, such as boundary conditions and the mesh non-uniformities. If a solution is ϕ, filtered values $\hat{\phi}$ satisfy

$$\alpha_f\hat{\phi}_{i-1} + \hat{\phi}_i + \alpha_f\hat{\phi}_{i+1} = \sum_{n=0}^{N} \frac{a_n}{2}(\phi_{i+n} + \phi_{i-n}) \tag{3.21}$$

With proper choice of coefficients, a $2N^{th}$ order formula on a 2N+1 point stencil can be obtained. By using Taylor series analyses, the N+1 coefficients, a_0, a_1, ..., a_N, are derived in terms of α_f. The parameter α_f can be adjusted in the range of -0.5 to 0.5. The higher value of α_f corresponds to less dissipative filter. α_f =0.5 corresponds the no filtering. According to reference 126, a value of α_f between 0.3 to 0.5 is appropriate. The filtering can be applied on the conserved variables or non-conserved variables after each iteration in every direction. For the grid points near boundary, either locally reduce-stencil-size LOC (low-order centered) formula or high order one-sided formula can be applied. The LOC method is simple and has been successful in some problems, but LOC requires very fine grid near boundary to keep low error. The one-sided high order formula does not need fine grid near boundary and can be more accurate. Table 3.2 lists the coefficients for

filter formula at interior points. Details about the coefficients of boundary points can be found in reference 28. Visbal et al. showed that the high order filter is superior to damping in terms of robustness and accuracy. [126]

Table 3.2 Coefficients for filter formula at interior points[78]

Scheme	a_0	a_1	a_2	a_3	a_4	a_5	Order
F2	$\frac{1}{2}+\alpha_f$	$\frac{1}{2}+\alpha_f$	0	0	0	0	2
F4	$\frac{5}{8}+\frac{3}{4}\alpha_f$	$\frac{1}{2}+\alpha_f$	$-\frac{1}{8}+\frac{1}{4}\alpha_f$	0	0	0	4
F6	$\frac{11}{16}+\frac{5}{8}\alpha_f$	$\frac{15}{32}+\frac{17}{16}\alpha_f$	$-\frac{3}{16}+\frac{3}{8}\alpha_f$	$\frac{1}{32}-\frac{1}{16}\alpha_f$	0	0	6
F8	$\frac{93}{128}+\frac{35}{64}\alpha_f$	$\frac{7}{16}+\frac{9}{8}\alpha_f$	$-\frac{7}{32}+\frac{7}{16}\alpha_f$	$\frac{1}{16}-\frac{1}{8}\alpha_f$	$-\frac{1}{128}+\frac{1}{64}\alpha_f$	0	8
F10	$\frac{193}{256}+\frac{63}{128}\alpha_f$	$\frac{105}{256}+\frac{151}{128}\alpha_f$	$-\frac{15}{64}+\frac{15}{32}\alpha_f$	$\frac{45}{512}-\frac{45}{256}\alpha_f$	$-\frac{5}{256}+\frac{1}{128}\alpha_f$	$\frac{1}{512}-\frac{1}{256}\alpha_f$	10

α_f is a free parameter in the range of $0<|\alpha_f|\le 0.5$

Metric Evaluation

When using finite the difference compact scheme, the metric calculation needs to be paid attention in computation, especially in the three-dimensional computation. When the governing equations are written in strong-conservation form, errors arise in finite difference discretizations. To keep these errors from degrading the accuracy of finite difference schemes, freestream preservation and metric cancellation should be satisfied. There are four metric identities: [127]

$$
\begin{aligned}
I_1 &= \left(\frac{\xi_x}{J}\right)_\xi + \left(\frac{\eta_x}{J}\right)_\eta + \left(\frac{\zeta_x}{J}\right)_\zeta = 0 \\
I_2 &= \left(\frac{\xi_y}{J}\right)_\xi + \left(\frac{\eta_y}{J}\right)_\eta + \left(\frac{\zeta_y}{J}\right)_\zeta = 0 \\
I_3 &= \left(\frac{\xi_z}{J}\right)_\xi + \left(\frac{\eta_z}{J}\right)_\eta + \left(\frac{\zeta_z}{J}\right)_\zeta = 0 \\
I_4 &= \left(\frac{\xi_t}{J}\right)_\xi + \left(\frac{\eta_t}{J}\right)_\eta + \left(\frac{\zeta_t}{J}\right)_\zeta + \left(\frac{1}{J}\right)_t = 0
\end{aligned}
\qquad (3.22)
$$

For the two-dimensional problems on distorted grids, when the metrics are computed with the same formula as those used for the fluxes, the compact scheme satisfies the

freestream preservation.[126] The use of analytic metrics on stretched curvilinear grid could produce large errors. [126] However, this straightforward method of computing metrics does not satisfy the metric cancellation for three-dimensional curvilinear grids. Unacceptable errors can be produced by using below formulas.

$$\begin{aligned} \xi_x/J &= y_\eta z_\zeta - y_\zeta z_\eta \\ \eta_x/J &= y_\zeta z_\xi - y_\xi z_\zeta \\ \zeta_x/J &= y_\xi z_\eta - y_\eta z_\xi \end{aligned} \tag{3.23}$$

Thus the special treatments of metric computation for three-dimensional problems were given: [127]

$$\begin{aligned} \xi_x/J &= (y_\eta z)_\zeta - (y_\zeta z)_\eta \\ \eta_x/J &= (y_\zeta z)_\xi - (y_\xi z)_\zeta \\ \zeta_x/J &= (y_\xi z)_\eta - (y_\eta z)_\xi \end{aligned} \tag{3.24}$$

Similar formulas are used to calculate other metric terms. The freestream preservation is recovered by using above formulas to transform metrics computation. [127]

Solution Procedure

First, forming the inviscid fluxes at the nodes and calculating the derivatives of these fluxes by using compact scheme. The metrics are calculated by the same scheme as that used in fluxes computation. For three-dimensional computation on curvilinear grids, special treatments are needed to satisfy the freestream preservation as mentioned above. Then, the viscous terms in the Navier-Stokes equations are obtained by twice applications of the compact scheme to primitive variables, u, v, w and T. After updating the solution at the interior grid points, the physical boundary conditions are applied. [78]

3.3.3 Euler Implicit Time Integration; Approximate Factorization

The governing equations can be written as

$$\frac{\partial \bar{Q}}{\partial t} = R(\bar{Q}) \quad \text{where} \quad R(\bar{Q}) = -\frac{\partial (\bar{E}_j - (\bar{E}_v)_j)}{\partial \xi_j} \tag{3.25}$$

Using Euler implicit time integration, above equations can be rewritten as

$$\frac{1}{\Delta t}\left[(1+\phi)(\bar{Q}^{n+1} - \bar{Q}^n) - \phi(\bar{Q}^n - \bar{Q}^{n-1})\right] = R(\bar{Q}^{n+1}) \tag{3.26}$$

where ϕ equal to 0 and 0.5 correspond the 1st and 2nd order temporal accuracy. The residual is linearized by using Taylor series expansions

$$R(\bar{Q}^{n+1}) \approx R(\bar{Q}^n) + \frac{\partial R}{\partial \bar{Q}} \Delta \bar{Q}^n$$

where $\Delta \bar{Q} = \bar{Q}^{n+1} - \bar{Q}^n$

Assuming a nondeforming grid and 1st order temporal accuracy, Equation (3.25) becomes

$$\left[\frac{I}{\Delta t} - \frac{\partial R}{\partial \bar{Q}}\right] \Delta \bar{Q}^n = R(\bar{Q}^n) \tag{3.27}$$

In terms of the inviscid and viscous fluxes, the equations can be rewritten as

$$\left[\frac{I}{\Delta t} + \frac{\partial}{\partial \xi_j}\left(\frac{\partial}{\partial \bar{Q}}\left[\bar{E}_j - (\bar{E}_v)_j\right]\right)^n\right] \Delta \bar{Q}^n = -\frac{\partial}{\partial \xi_j}\left(\bar{E}_j - (\bar{E}_v)_j\right)^n \tag{3.28}$$

To save computational time, the approximate factorization of Beam and Warming is used, the equations can be approximately factorized as

$$\begin{aligned}&\left[\frac{I}{\Delta t} + \frac{\partial}{\partial \xi_1}\left(\frac{\partial}{\partial \bar{Q}}\left[\bar{E}_1 - (\bar{E}_v)_1\right]\right)\right]\left[\frac{I}{\Delta t} + \frac{\partial}{\partial \xi_2}\left(\frac{\partial}{\partial \bar{Q}}\left[\bar{E}_2 - (\bar{E}_v)_2\right]\right)\right] \\ &\left[\frac{I}{\Delta t} + \frac{\partial}{\partial \xi_3}\left(\frac{\partial}{\partial \bar{Q}}\left[\bar{E}_3 - (\bar{E}_v)_3\right]\right)\right]\left[\frac{I}{(\Delta t)^2}\right]^{-1} \Delta \bar{Q}^n = -\frac{\partial}{\partial \xi_j}\left(\bar{E}_j - (\bar{E}_v)_j\right)\end{aligned} \tag{3.29}$$

The solution is obtained by solving the following three one-dimensional equations

$$\left[\frac{I}{\Delta t} + \frac{\partial}{\partial \xi_1}\left(\frac{\partial}{\partial \bar{Q}}\left[\bar{E}_1 - (\bar{E}_v)_1\right]\right)\right] \Delta \bar{Q}^* = -\frac{\partial}{\partial \xi_j}\left(\bar{E}_j - (\bar{E}_v)_j\right)^n \tag{3.30}$$

$$\left[\frac{I}{\Delta t} + \frac{\partial}{\partial \xi_2}\left(\frac{\partial}{\partial \bar{Q}}\left[\bar{E}_2 - (\bar{E}_v)_2\right]\right)\right] \Delta \bar{Q}^{**} = \Delta \bar{Q}^* \tag{3.31}$$

$$\left[\frac{I}{\Delta t} + \frac{\partial}{\partial \xi_2}\left(\frac{\partial}{\partial \bar{Q}}\left[\bar{E}_2 - (\bar{E}_v)_2\right]\right)\right] \Delta \bar{Q} = \frac{\Delta \bar{Q}^{**}}{(\Delta t)^2} \tag{3.32}$$

The solution of each of these equations is obtained by solving a block tri-diagonal set of equations.

3.3.4 Discretization of the Viscous Terms

The viscous fluxes on the left-hand side of the differential equations, Equation (3.26), are given by

$$\frac{\partial}{\partial \xi_j}\frac{\partial (\bar{E}_v)_j}{\partial \bar{Q}} = \frac{\partial}{\partial \xi_1}\frac{\partial (\bar{E}_v)_1}{\partial \bar{Q}} + \frac{\partial}{\partial \xi_2}\frac{\partial (\bar{E}_v)_2}{\partial \bar{Q}} + \frac{\partial}{\partial \xi_3}\frac{\partial (\bar{E}_v)_3}{\partial \bar{Q}} \tag{3.33}$$

Differentiating the portions with terms that are functions of ξ^n (where $n \neq m$) will produce cross-derivative terms. The presence of these terms on the left-hand side of the equation would destroy the efficiency of the upper and lower triangular matrix solution by requiring a central differencing of these terms. In some applications, the viscous terms containing derivatives parallel to the solid body surface can be neglected relative to those in the normal direction. This approximation is known as the thin-layer approximation where only the viscous terms containing derivatives normal to the body surface (along the coordinate line), are retained. In this investigation, the thin-layer approximation was used only to simplify the viscous terms on the left-hand side of the differential equations for better efficiency of the computer code. While the cross-derivative terms were retained on the right-hand side of the differential equation where they were evaluated explicitly.

On the right-hand side of the differential equation, Equation (3.26), the viscous terms contribution to the residual is given by

$$\bar{R}_v = \frac{\partial (\bar{E}_v)_j}{\partial \xi_j} \tag{3.34}$$

The viscous fluxes are linearized in time by

$$(\bar{E}_v)_j^{n+1} = (\bar{E}_v)_j^n + O(\Delta t) \tag{3.35}$$

The viscous terms at a time step n+1 are evaluated using the information from the previous time step, n. The fluxes are centrally differenced and a second-order approximation to the cross-derivative terms is used.

3.3.5 Large Eddy Simulation

To accurately predict the turbulent flow, direct numerical simulation (DNS) is the straightforward method. However, DNS is also very expensive method because it requires that the grid should be fine enough to capture the smallest scales in the flow.

Large eddy simulation (LES) has been shown to yield accurate turbulence simulation at an acceptable CPU time compared with DNS. In LES the large scales are computed directly and the smallest scales are modeled by a subgrid scale model. The LES equation for compressible flows are the Navier-Stokes equations written using the filtered variables and the additional subgrid terms in the momentum and energy equations. Following Moin et al.[89], the subgrid term in the momentum equations can be written as

$$\tau_{kn} = -2C\rho\Delta^2\left|\tilde{S}\right|(\tilde{S}_{kn} - \tfrac{1}{3}\tilde{S}_{mm}\delta_{kn}) + \tfrac{1}{3}\tau_{mm}\delta_{kn} \tag{3.36}$$

where

$$\tilde{S}_{kn} = \frac{1}{2}\left(\frac{\partial \tilde{u}_k}{\partial x_n} + \frac{\partial \tilde{u}_n}{\partial x_k}\right), \quad \left|\tilde{S}\right| = \sqrt{2\tilde{S}_{kn}\tilde{S}_{kn}}$$

and Δ^2 is a spatial filter width and is set equal to cell size. In the three dimensional case, $\Delta = \sqrt[3]{V}$ and V is the volume of the cell. According to the Smagorinsky subgrid simulation (SGS) model [9], C is a constant and is set to 0.01. Near the solid wall, a damping function is added and C is written as

$$C = 0.01(1 - \exp(-(y^+/25)^3)), \quad y^+ = \frac{\rho u_\tau y}{\mu}, \quad u_\tau = \sqrt{\frac{\tau_w}{\rho}}$$

In dynamic SGS model developed by Germano et al.[26], the C is not a constant and is determined by a dynamic procedure. The dynamic SGS model is better but more computationally expensive than the Smagorinsky SGS model. The last term in Equation 3.35 is usually neglected and little error is introduced. Then, the SGS stresses in the Navier-Stokes equations can be combined with the laminar viscosity coefficient and is given by

$$\mu_{eff} = \mu_{Laminar} + \mu_{SGS}, \text{ and } \mu_{SGS} = C\rho\Delta^2\left|\tilde{S}\right| \tag{3.37}$$

Similarly in the energy equation, the hear conduct coefficient is replaced by

$$k_{eff} = k_{Laminar} + k_{SGS} = \frac{\mu_{Laminar} c_p}{Pr_{Laminar}} + \frac{\mu_{SGS} c_p}{Pr_{SGS}} \tag{3.38}$$

3.4 Flow Initial and Boundary Conditions

Initial and boundary conditions are very important in the computation. In-appropriate boundary conditions can contaminate the solution or even make computation

divergent. The boundary conditions used in this investigation are discussed in the flowing sections.

3.4.1 Initial Conditions

For the steady flow problems, the initial conditions are assumed as impulsively started initial conditions. These initial conditions mimic inserting the configuration suddenly in the freestream. For the unsteady flow problems, the initial conditions are set as the solution of the steady flow calculations with same configuration and flow conditions.

3.4.2 Solid Surface Conditions

For a solid surface, the velocity, pressure and temperature conditions should be specified. For stationary surface without blowing or suction, the no-slip and no-penetration conditions are enforced, $\vec{v} = \vec{v}_{surface}$. The normal pressure gradient, $\frac{\partial p}{\partial \hat{n}}$, is set to zero and the adiabatic condition is enforced, $(\frac{\partial T}{\partial \hat{n}})_s = 0$.

For a moving surface, such as moving tails due to buffet loading, the normal pressure gradient becomes $\frac{\partial p}{\partial \hat{n}} = -\rho \vec{a} \cdot \hat{n}$, where $\vec{a}$ is the acceleration vector of the surface and $\hat{n}$ is the surface unit normal. For the tails, the acceleration vector due to the coupled bending and torsion deflections is given by

$$\vec{a} = -\vec{r}\left[\frac{\partial^2\theta}{\partial t^2}\sin\theta + \left(\frac{\partial\theta}{\partial t}\right)^2\cos\theta\right]\hat{i} + \left\{\frac{\partial^2 w}{\partial t^2} + \vec{r}\left[\frac{\partial^2\theta}{\partial t^2}\cos\theta - \left(\frac{\partial\theta}{\partial t}\right)^2\sin\theta\right]\right\}\hat{j} \qquad (3.39)$$

where $\vec{r}$ is the displacement vector to the point measured from the elastic axis of the tail.

For the surface with blowing or suction, the velocity at the surface is set by the blowing/suction coefficient C_Q

$$\vec{v}_{b/s} = \left(\frac{SC_Q}{A}\right)U_\infty \hat{n}_{b/s} \qquad (3.40)$$

where A is the blowing/suction tube cross section area and $\hat{n}_{b/s}$ is the unit normal of the blowing/suction direction.

3.4.3 Far Field and Non-Reflection Boundary Conditions

At infinite distance from the source of disturbance the flow is assumed to be undisturbed and equals the free stream flow. Because of the limitation of computational domain, some special treatments, so-called non-reflecting boundary conditions, must be applied to mimic the infinite domain boundary. These conditions are based on the characteristic theory and are implemented at the far-field boundary of the computational domain.

3.4.4 Zonal Boundary Conditions

For the multi-block computational domain, information needs to be exchanged at the block interfaces. So the zonal boundary conditions are used. At the interface of two blocks, ghost cells, which belong to each block separately, are used. After each iteration, flow variables are exchanged and saved in ghost cells.

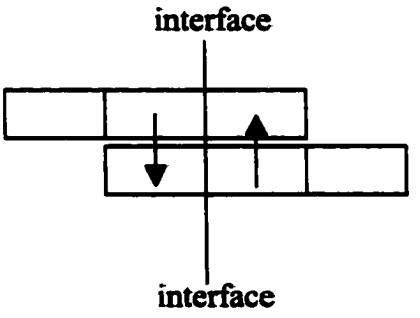

3.5 Aeroelastic Equations

For the twin-tail buffet problem, the wing is assumed as rigid and the vertical tails are simplified as flexible cantilevered beams. The tail bending and torsion displacements are assumed small in comparison with the tail thickness and the cross section of beams is assumed rigid. The dimensionless, linearized aeroelastic equations for the bending deflection, w, and the twist angle, θ, are given by[116]

$$\frac{\partial^2}{\partial z^2}\left[EI(z)\frac{\partial^2 w}{\partial z^2}(z,t)\right]+m(z)\frac{\partial^2 w}{\partial t^2}(z,t)+m(z)x_\theta(z)\frac{\partial^2 \theta}{\partial t^2}(z,t)=N(z,t) \qquad (3.41)$$

$$\frac{\partial}{\partial z}\left[GJ(z)\frac{\partial \theta}{\partial z}(z,t)\right]-m(z)x_\theta(z)\frac{\partial^2 w}{\partial t^2}(z,t)-I_\theta(z)\frac{\partial^2 \theta}{\partial t^2}(z,t)=-M_t(z,t) \qquad (3.42)$$

where z is the vertical distance from the fixed support, N is the normal force per unit length and M_t is the twisting moment per unit length, I(z) is the area moment of inertia and is given by

$$I(z) = \rho \frac{b(z) \times t(z)^3}{12} \tag{3.43}$$

J(z) is the geometrical torsion constant. For thin rectangular cross section, it is given by

$$J(z) = \rho \frac{b(z) \times t(z)^3}{3} \tag{3.44}$$

The mass moment of inertia per unit length about the elastic axis, I_θ, is equal to $I_\theta = m x_\theta^2 + I_{zzCM}$, where m is the mass per unit length, I_{zzCM} the mass moment of inertia per unit length about the center of mass axis, and x_θ the distance between the elastic axis and inertia axis. Then, I_θ is given by

$$I_\theta(z) = m(z) x_\theta^2 + \frac{m(z)(t^2(z) + b^2(z))}{12} \tag{3.45}$$

The EI and GJ are the bending and torsional stiffness of the tail section, and E is the elastic modulus of elasticity. The modulus of rigidity, G, is given by

$$G = \frac{E}{2(1+\nu)}, \quad \nu = \frac{1}{3} \tag{3.46}$$

The aeroelastic equations are normalized by $L, a_\infty, L/a_\infty$ and ρ_∞ for the length, velocity, time and density, respectively. The modulus of elasticity, E, and the modulus of rigidity, G, are normalized by $\rho_\infty a_\infty^2$.

3.6 Computational Structural Dynamics Formulation

For the vertical tails, which are treated as flexible cantilevered beam, the dimensionless, linearized governing equations are given by Equation (3.41) and (3.42). The Galerkin method is used to solve these equations.

Using modal analysis, the dependent variables are expanded in terms of the natural free vibration modes of a cantilevered beam as[116]

$$w(z,t) = \sum_{i=1}^{\bar{I}} \phi_i(z) q_i(t) \tag{3.47}$$

$$\theta(z,t)=\sum_{j=I+1}^{\bar{M}}\phi_j(z)q_j(t) \tag{3.48}$$

where $\phi_i(z)$ and $\phi_j(z)$ are the comparison functions satisfying the free vibration modes of bending and torsion, respectively; and $q_i(t)$, $q_j(t)$ are generalized coordinates for bending and torsion, respectively.

The comparison functions for the bending deflections are taken as the eigenfunctions of uniform beam given by

$$\phi_i(z)=C_r\left[\frac{\sin(\beta_i L)-\sinh(\beta_i L)}{\cos(\beta_i L)+\cosh(\beta_i L)}\right][\sin(\beta_i z)-\sinh(\beta_i z)]+[\cos(\beta_i z)-\cosh(\beta_i z)] \tag{3.49}$$

where β_i is the solution of the bending frequency equation for cantilevered beam which is given by

$$\cos(\beta_i L)\cosh(\beta_i L)=-1 \tag{3.50}$$

The solutions satisfying the bending frequency equation are given by

$$\begin{gathered}\beta_1=1.875 \quad \beta_2=4.694 \quad \beta_3=7.855\\ \beta_4=10.996 \quad \beta_5=14.137 \quad \beta_6=17.279\\ \beta_i=(i-0.5)\pi \quad \text{as} \quad i\to\infty\end{gathered} \tag{3.51}$$

and the bending natural frequency is given by

$$\omega_i=\beta_i^2\sqrt{\frac{EI}{m}} \tag{3.52}$$

The comparison functions for the torsional deflections are given by

$$\phi_j(z)=\sin(\beta_j z) \tag{3.53}$$

There are infinite solutions satisfying the torsional equation. They are given by

$$\beta_j=\frac{(2j-1)\pi}{2L} \qquad j=1,2,3\ldots\infty \tag{3.54}$$

The torsion natural frequency is given by

$$\omega_j=\frac{(2j-1)\pi}{2L}\sqrt{\frac{GJ}{I_\theta}} \tag{3.55}$$

Rewrite the equations in matrix form; the original governing aeroelastic equations have been transformed from coupled partial differential equations to a $\overline{M}$ set of coupled 2nd ordinary differential equations as

$$[M]\{\ddot{q}\}+[K]\{q\}=\{Q\} \tag{3.64}$$

or

$$\begin{bmatrix} M_{11} & M_{12} \\ M_{21} & M_{22} \end{bmatrix}\begin{Bmatrix} \ddot{q}_i \\ \ddot{q}_j \end{Bmatrix}+\begin{bmatrix} K_{11} & 0 \\ 0 & K_{22} \end{bmatrix}\begin{Bmatrix} q_i \\ q_j \end{Bmatrix}=\begin{Bmatrix} \overline{N}_1 \\ \overline{N}_2 \end{Bmatrix} \quad \begin{matrix} i=1,2,\cdots,\bar{I} \\ j=\bar{I}+1,\cdots,\overline{M} \end{matrix} \tag{3.65}$$

Where

$$M_{11}=\int_0^L m\phi_r\phi_i dz \tag{3.66}$$

$$M_{12}=M_{21}=\int_0^L m x_\theta \phi_r\phi_j dz \tag{3.67}$$

$$M_{22}=\int_0^L I_\theta \phi_s\phi_j dz \tag{3.68}$$

$$K_{11}=\int_0^L EI\frac{d^2\phi_r}{dz^2}\frac{d^2\phi_i}{dz^2}dz \tag{3.69}$$

$$K_{22}=\int_0^L GJ\frac{d\phi_s}{dz}\frac{d\phi_j}{dz}dz \tag{3.70}$$

$$\overline{N}_i=\int_0^L \phi_r N dz \tag{3.71}$$

$$\overline{N}_2=\int_0^L \phi_s M_t dz \tag{3.72}$$

The equations can be further reduced to a set of coupled first order ordinary differential equations by introducing a new variable η

$$\begin{aligned} \{\eta\}&=[I]\{\dot{q}\} \\ [M]\{\dot{\eta}\}+[K]\{q\}&=\{Q\} \end{aligned} \tag{3.73}$$

Then, the new system of equations can be written in state space form as

$$\begin{Bmatrix} \dot{\eta} \\ \dot{q} \end{Bmatrix}=\begin{bmatrix} 0 & -[M]^{-1}[K] \\ I & 0 \end{bmatrix}\begin{Bmatrix} \eta \\ q \end{Bmatrix}+\begin{Bmatrix} [M]^{-1}\{Q\} \\ 0 \end{Bmatrix} \tag{3.74}$$

The solutions of these equations can be obtained by using fifth-order accurate Runge-Kutta method. Then, by substituting these solutions into Equation (3.47) and (3.48), the bending deflection, w, and the torsion deflection, θ, can be obtained.

3.7 Structural Initial and Boundary Conditions

The tails are initially assumed in an undeformed stationary state. The initial conditions are given by

$$w(z,0)=\frac{\partial w(z,0)}{\partial t}=0$$
$$\theta(z,0)=\frac{\partial \theta(z,0)}{\partial t}=0 \tag{3.75}$$

The tails are assumed to respond as cantilevered beams, clamped at the root and free at the tip. They are free to oscillate in both coupled or uncoupled bending torsion oscillations. The corresponding boundary conditions for cantilevered beam are given by

$$w(0,t)=\frac{\partial w}{\partial z}(0,t)=\frac{\partial^2 w}{\partial z^2}(L,t)=\frac{\partial}{\partial z}\left[EI(L)\frac{\partial^2 w}{\partial z^2}(L,t)\right]=0$$
$$\theta(0,t)=\frac{\partial \theta}{\partial t}(L,t)=0 \tag{3.76}$$

where L is the vertical height of the tail. The boundary conditions at the clamped root are plugged in the computational solver explicitly, while the boundary conditions at the free-end are used before in the process of transforming the aeroelastic equations form their partial differential form to their ordinary differential form.

3.8 Grid Displacement Equations

After the bending deflection, w, and the torsion angle, θ, of the tails are obtained, the grid points are smoothly deformed to accommodate the deflections of the tail. Since the grid displacement is relatively small and the grid is deformed at every time step, simple interpolation procedure is used to compute the y and z coordinates of the grid. These equations for the right side of the tail are given by

$$y_{i,j,k}^{n+1}=y_{i,j,k}^{n}+[w_{i,j,k}^{n}+(X-x_{i,j,k}^{n})\tan\theta_{i,j,k}^{n+1}]\cos\left(\frac{\pi}{2}\frac{y_{i,j,k}^{n}}{Y}\right) \tag{3.77}$$

$$z_{i,j,k}^{n+1}=z_{i,j,k}^{n}-[\Delta z_{i,j,k}^{o}-\sqrt{(\Delta z_{i,j,k}^{o})^2-(\Delta w^{n+1})^2}]\cos\left(\frac{\pi}{2}\frac{z_{i,j,k}^{n}}{Z}\right) \tag{3.78}$$

where $y^{n+1}_{i,j,k}$ and $z^{n+1}_{i,j,k}$ are the y and z coordinates of a grid point at the n+1 time step, $z^{o}_{i,j,k}$ is the original z coordinate of a tail grid point and $\Delta z^{o}_{i,j,k} = z^{o}_{i,j,k} - z^{o}_{i,j,k-1}$, Y is the maximum value of y coordinate from the grid point on tail surface to the corresponding point at the right boundary of the computational domain, Z is the maximum value of z coordinate from the tail root to the upper boundary of the computational domain and X is the x coordinate of the tail elastic axis. The deforming grid generated by these equations is smooth and can respond to the deformation of the tail. The displacements of grid are decreased smoothly from the tail surface to the outer boundary of the computational domain. At each time step, the metric terms and the grid speed terms are updated once the new grid is obtained.

3.9 Method of Solution

For the delta-wing/twin-tails problem, the delta wing is assumed to be rigid, while the tail is considered flexible. The procedure includes several steps.

1) Initially, the tails are assumed to be rigid and the grids do not deform. The Navier-Stokes equations are solved by using pseudo-time stepping, implicit, upwind finite-volume scheme. Once the computation converges, the resulting solution is used as the initial condition for next step.
2) The time accurate, implicit, upwind finite-volume scheme is used to solve the fluid flow problem. The tails can deform and the grid speed is obtained. The initial grid speed is set to zero. In this step, the flow field solution and the pressure distribution on the tail surfaces are obtained.
3) The normal force and twisting moment acting on tail surfaces due to the pressure distribution obtained in step 2 are computed. Next, the twin-tail deflections are obtained by using the aeroelastic equations.
4) Using the twin-tails deflections, new grid is generated by solving the grid displacement equations. The metric coefficients and the grid speed are updated.
5) The computational cycle, which includes steps 2, 3 and 4, is repeated every time step. Equal time step is used for both flow and structural computations. The tales are rigid in step 1, but are movable in steps 2, 3 and 4.

For the JaVA/synthetic jet flow control problems, the procedure includes: 1) Solving for initial solution while the actuator is not active, and 2) Solving for disturbance flow while the actuator is active.

CHAPTER 4: ACTIVE FLOW CONTROL

4.1 Introduction

Active flow control for twin-tail buffet alleviation is investigated. Flow suction along the vortex cores (FSVC) of the leading edges of the delta wing is used in order to delay the vortex breakdown flow upstream of the twin tail and to modify the vortex core path. This approach has been used earlier by Hummel[37] in his experimental research work. A parametric study of the effects of the span-wise position and axial orientation of the suction tubes and volumetric suction flow rate on the twin-tail buffet response is carried out. The computational model consists of a sharp-edged delta wing of aspect ratio one and swept-back flexible twin tail with taper ratio of 0.23. This complex multidisciplinary problem is solved sequentially using three sets of equations for the fluid flow, aeroelastic response and grid deformation, on a dynamic multi-block grid structure. The computational model is pitched at 30° angle of attack. The freestream Mach number and Reynolds number are 0.3 and 1.25 million, respectively. The model is investigated for the inboard position of the twin tails, which corresponds to a separation distance between the twin tails of 33% of the wingspan. Comparison of the time history and power spectral density responses of the tails for various FSVC controls are presented and discussed.

4.2 Computational Model: Active Flow Control Method (FSVC)

The twin tail-delta wing configuration consists of a 76° swept back, sharp-edged delta wing (aspect ratio of one) and dynamically scaled flexible twin tail similar to those used by Washburn et al.[129]. The vertical tails are oriented normal to the upper surface of the delta wing and have a centerline sweep of 53.5°. Each tail is made of a single Aluminum spar and Balsa wood covering. The Aluminum spar has a taper ratio of 0.3 and a constant thickness of 0.001736. The Aluminum spar is constructed from 6061-T6 alloy with density, ρ, modulii of elasticity and rigidity, E and G of 2693 kg/m^3, 6.896×10^{10} N/m^2 and 2.5925×10^{10} N/m^2, respectively. The Balsa wood covering has a taper ratio of 0.23 and aspect ratio of 1.4. The Balsa thickness decreases gradually from 0.0211 at the tail root to 0.0111 at the tail midspan and then constant thickness of 0.0111

is maintained to the tail tip. The tail cross section is a semi-diamond shape with bevel angle of 20°. The Balsa density, modulii of elasticity and rigidity, E and G, are 179.7 kg/m^3, 6.896×10^8 N/m^2 and 2.5925×10^8 N/m^2, respectively. The tails are assumed to be magnetically suspended and the leading edge of the tail root is positioned at x/c = 1.0, measured from the wing apex. The configuration is statically pitched at 30° angle of attack. The freestream Mach number and Reynolds number are 0.3 and 1.25×10^6, respectively. A multi-block grid consisting of four blocks is used for the solution of the problem. The first block is O-H grid for the wing and upstream region, with 101×50×54 grid points in the wrap around, normal and axial directions, respectively. The second block is H-H grid for the inboard region of the twin tails, with 15×50×13 grid points in the wrap around, normal and axial directions, respectively. The third block is H-H grid for the outboard region of the twin tails, with 87×50×13 grid points in the wrap around, normal and axial directions, respectively. The fourth block is O-H grid for the downstream region of the twin tails, with 101×50×25 grid points in the wrap around, normal and axial directions, respectively. Figure 4.1 shows the grid topology of the twin tail-delta wing configuration.

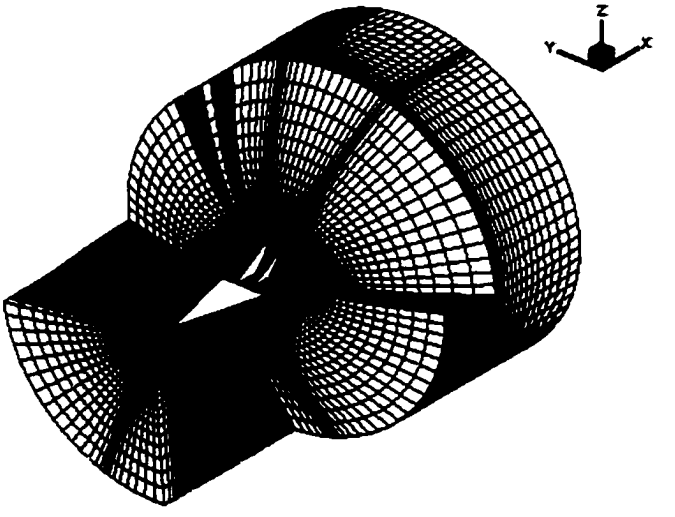

Figure 4.1 Three dimensional grid topology of the twin tail delta wing configuration.

The main purpose of flow control method is to modify the flow field in the region of the twin-tail. Unsteady vortex breakdown of the leading-edge vortex cores develops

upstream of the twin-tail and moves downstream in close proximity to the twin-tail. This highly unsteady vortex-breakdown flow produces unsteady differential pressure on each tail forcing it to oscillate through wide ranges of amplitudes and frequencies, which eventually result into a tail fatigue failure. Hence, flow control method should be designed to move the vortex breakdown location downstream behind the twin-tail and displace the vortex core path in such a way as to add more aerodynamic damping to tail. The control method should be effective over the whole ranges of angle of attack and Mach number during the configuration maneuverability. Moreover, the control method should not produce adverse effects on the aerodynamic performance. This is a multidisciplinary, time-dependent control problem.

To deal with such complex problem, the approach that we have adopted is a step-by-step investigation of simple and combined flow control method. The first method is the tangential leading edge blowing (TLEB)[115, 62]. The second method is the flow suction along the vortex core (FSVC) [115, 62]. In the TLEB method, an air jet is blown tangential to the delta wing surface along its whole leading edge. The volume flow rate of this jet is varied linearly along the wing leading edge. The control effect of this method is to modify the path of the leading edge vortex core, moving it closer to the tail to intersect it. This will increase the aerodynamic damping of the tail. An other effect of this method is to increase the vortex core axial momentum, which in turn moves the vortex breakdown location further downstream. In the FSVC method, flow suction is applied along the leading edge vortex core in order to remove the low-level axial momentum flow from the vortex breakdown region. This control method will increase the axial momentum of the vortex flow and move the vortex breakdown further downstream.

It had been shown that TLEB method moved the vortex breakdown location downstream and the leading edge vortices laterally toward the twin tail[115, 62]. The TLEB control produced lower tail root bending and twisting moments as well as lower torsion deflection and acceleration than those of the no-control case. However, the bending deflection and acceleration were higher than those of the no-control case. In the FSVC method (out position)[115], it has been shown that size of the vortex breakdown region has been reduced and moved in the downstream direction. It also reduced the tail bending

deflection. However, the root bending momentum, bending and torsion accelerations and torsion deflection of the tail were higher than those of the no-control case.

The TLEB and FSVC (out position) methods were combined and applied simultaneously to the same configuration[115]. The results have shown no improvement compared with those of each method being applied separately.

Further investigation of the FSVC method has shown that moving the suction tubes in the spanwise direction toward the tail location produced favorable aeroelastic control. This control method is called the FSVC in position method. The results of this method have shown additional reduction in the tail root bending and twisting moments, its tip bending and torsion accelerations and its tip torsion deflection than those of no-control case. Increasing the suction volumetric flow rate produced further reduction in the tail aeroelastic responses. It is therefore concluded that the FSVC in position method produces the best control in comparison with all the other methods that were tried before.

The imaginary suction tubes are installed behind the wing at $x_t/c = 1.3$ on both sides of the wing along the center of the two vortices, which are almost at $z_t/c = 0.2$ above the wing surface at this location, shown in Figure 4.2. This FSVC method is called suction out position. A volume flux Q is sucked away from the vortex cores along the vortex path at an angle of 30°. The suction coefficient is $C_Q = 3.53\times10^{-2}$ and the suction-tubes non-dimensional cross-section area is 2.94×10^{-3}. A parametric study of the effects of the spanwise position of the suction tubes and volumetric suction flow rate on the twin-tail buffet response is also investigated. In this case, the spanwise position of the suction tubes is moved towards the twin tails (called FSVC in position) with the same volumetric suction flow rate. The suction tubes cross-sectional area is then increased from 2.94×10^{-3} to 5.29×10^{-3}, keeping the suction velocity fixed. This results in increasing the suction coefficient from $C_Q=3.53\times10^{-2}$ to $C_Q=6.354\times10^{-2}$. To get better results, the axial orientation of suction tubes is investigated. The direction of suction tubes is tilted to the right at an angle of $+\varphi$ or to the left at angle of $-\varphi$ with respect to an observer looking in the upstream direction, shown in Figure 4.2.

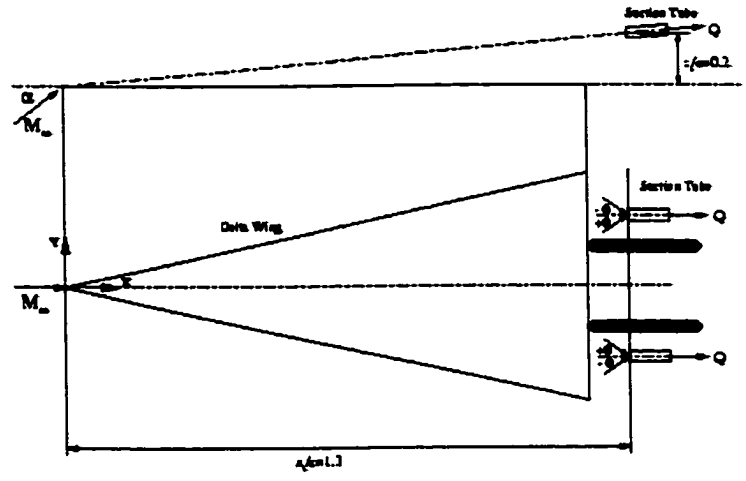

Figure 4.2 Schematic view showing the arrangement for sucking of the flow.

4.3 Flow Field Results of FSVC Method

Figures 4.3 and 4.4 show snap shots of the flow field results at $\tau = 19$ after allowing the tails to move and interact with the flow. The figures show a top view of the vortex cores total pressures iso-surfaces, total pressure contours and instantaneous streamlines on a cross-flow plane at x=1.096, for the no-control case. Figures 4.6 and 4.7 show the flow field results for the FSVC method (in position) with $\varphi = +10°$at the same time instant as that of the no-control results. Figures 4.9 and 4.10 show the flow field results for the FSVC in-position method with $\varphi = -10°$ at the same time instant.

The top view figures of vortex cores (Figures 4.3, 4.6 and 4.9) show the effect of FSVC in-position methods on the location of vortex-breakdown point. It is observed that when the suction tubes are titled to the right or the left the location of vortex-breakdown point moves further downstream. The best control has been achieved when the suction tubes are tilted to the left at $\varphi = -10°$, where the breakdown point is at 70% of the wing chord. The no-control case shows that the breakdown point is at 64% of the wing chord.

The cross-flow-plane figures of the total pressure contours and instantaneous streamlines (Figures 4.4, 4.7 and 4.10) show the substantial effect of FSVC methods, particularly when the suction tubes are tilted. It is observed that tilting the suction tubes to the right or the left lowers the vortex core vertical location and moves it away from the

tail. Moreover, it increases the high total-pressure flow in the region between the tails. The best control has been achieved with the suction tubes tilted to the left.

The results of FSVC methods show that when the suction tubes are tilted to the left they produce the best control results of the vortex-breakdown region so far. The location of the vortex-breakdown point is moved in the spanwise direction away from the tail location, and additional high total-pressure flow moves in the region between the twin tails. These modifications of the flow field above the wing and near the tails are expected to reduce the aeroelastic responses, and hence the fatigue failure.

4.4 Load and Aeroelastic Results of FSVC Method

Figures 4.5, 4.8 and 4.11 show the distribution histories of bending deflection, w, rotation angle deflection, θ, normal force, N, and twisting moment, M, versus the tail height, z. Each figure shows the distribution every dimensionless time unit. These curves are labeled as A, B, etc. It is observed that the bending deflections are in the first, second and third mode shapes, while the rotation angle deflections are in the first and second mode shapes. The bending deflections are mostly positive and the twisting angle deflections are mostly negative. On the other hand, the maximum normal forces are occurring at the tail root, and the maximum twisting moments are occurring in the distance range of $z = 0.04$ to $z = 0.06$, which corresponds to 17.8% to 26.7% of the tail span, respectively. The normal forces are mostly positive and the twisting moments are mostly negative. It is observed that the FSVC methods reduce the variations in the normal force and twisting moment in comparison with those of the no-control case. They also reduce the bending and rotation angle deflections. The best control is achieved with the suction tubes tilted at $\varphi = -10°$.

Figure 4.12 shows comparisons of the time history of the tip bending deflection, tip rotation angle deflection, tip bending acceleration and tip rotation angle acceleration for the FSVC methods and no-control case. It is observed that the best control of the amplitudes of these responses is obtained with the suction tubes tilted at $\varphi = -10°$. Figure 4.13 shows the power spectral density (PSD) of the corresponding tip bending and rotation accelerations. It is observed that the FSVC with the suction tubes tilted at

φ=−10° produces the lowest peaks. However, there is no shift in the frequencies of these peaks.

Figures 4.14 shows comparisons of the time history of the root bending moment and the root twisting moment for FSVC methods and the no-control case. It is observed that the best control of the amplitudes of these responses is obtained again with the suction tubes tilted at $\varphi = -10°$. Figures 4.15 shows the PSD of the corresponding root bending and twisting moments. The lowest peaks of the PSD are obtained for the same tubes tilting. Again, there is no shift in the frequencies of these peaks.

It is important to mention that Figures 4.12 and 4.14 are not showing any period or phase changes due to the FSVC methods. The main effect of these methods is the amplitude reduction of the various responses.

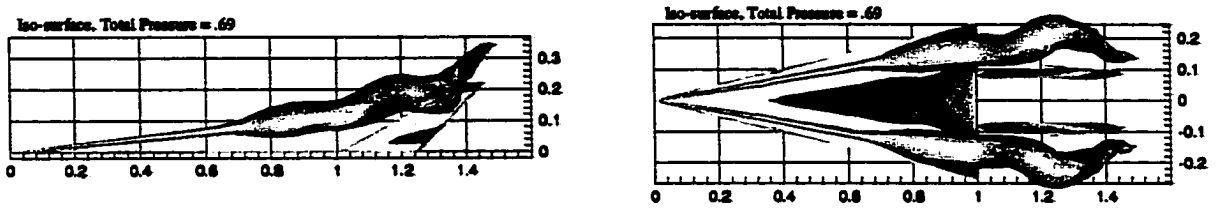

(a) Side view (b) Top view

Figure 4.3 Top view and side view showing the vortex core total pressure iso-surface. No-control case at $\tau = 19$, $M_\infty = 0.3$, $\alpha = 30°$, $Re = 1.25\times10^6$.

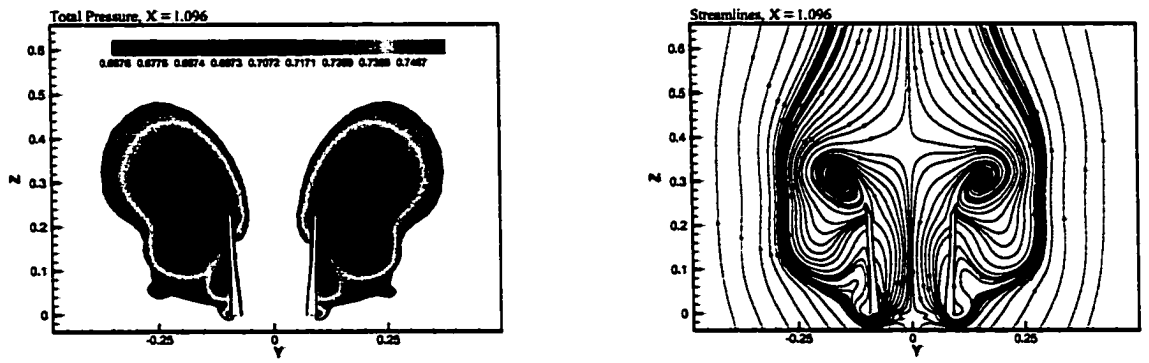

Figure 4.4 Snap shots of total pressure contours and instantaneous streamlines on cross plane, $x = 1.096$. No-control case at $\tau = 19$, $M_\infty = 0.3$, $\alpha = 30°$, $Re = 1.25\times10^6$.

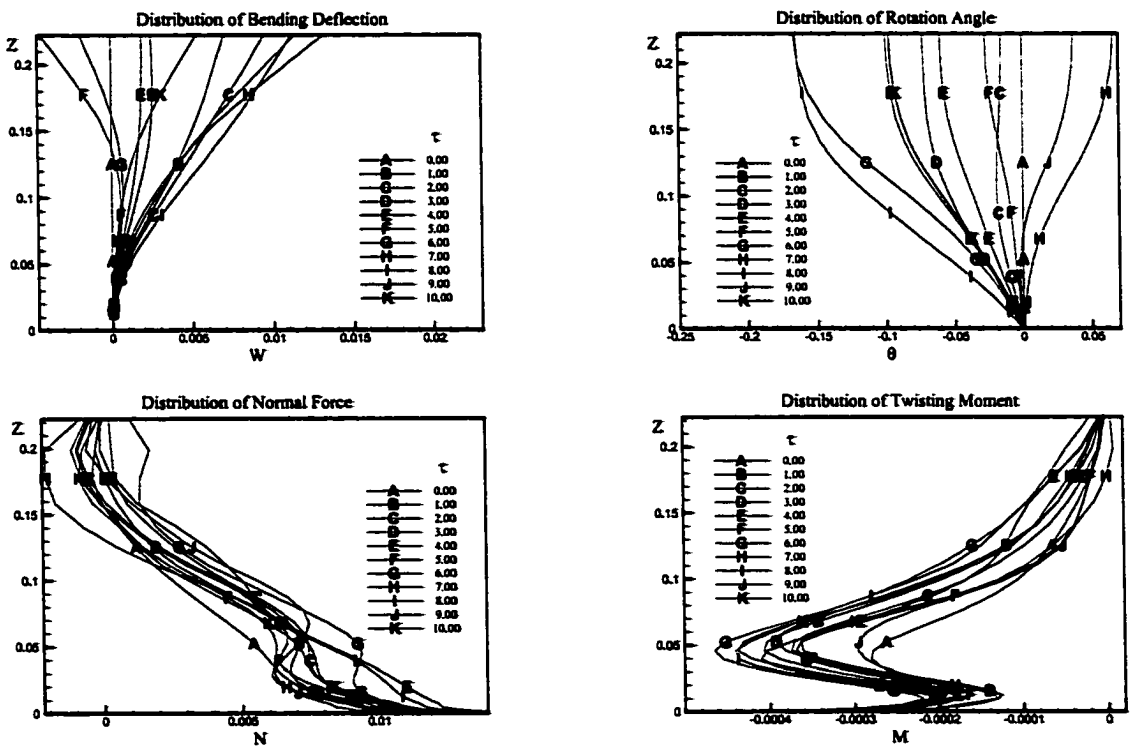

Figure 4.5 Distribution of bending deflection, rotation angle, normal force and twisting moment along the tail span. No-control case at $M_\infty = 0.3$, $\alpha = 30°$, $Re = 1.25\times10^6$.

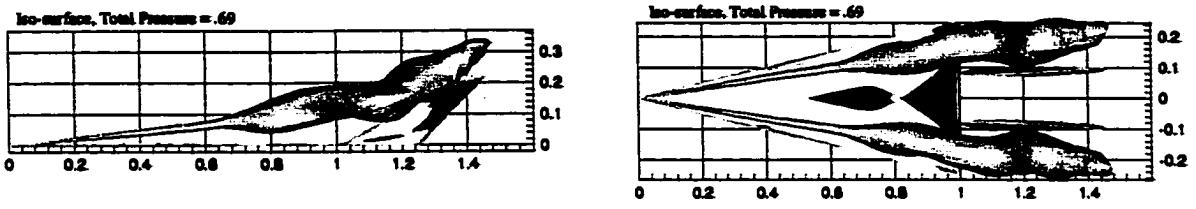

(a) Side view (b) Top view

Figure 4.6 Top view and side view showing the vortex core total pressure iso-surface. FSVC (in, 10°) case at $\tau = 19$, $M_\infty = 0.3$, $\alpha = 30°$, $Re = 1.25\times10^6$.

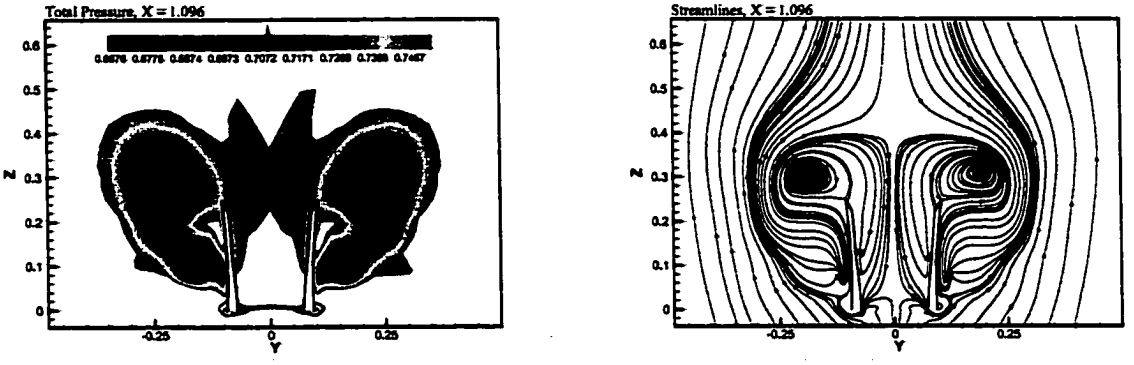

Figure 4.7 Snap shots of total pressure contours and instantaneous streamlines on cross plane, $x = 1.096$. FSVC (in, 10°) case at $\tau = 19$, $M_\infty = 0.3$, $\alpha = 30°$, $Re = 1.25\times10^6$.

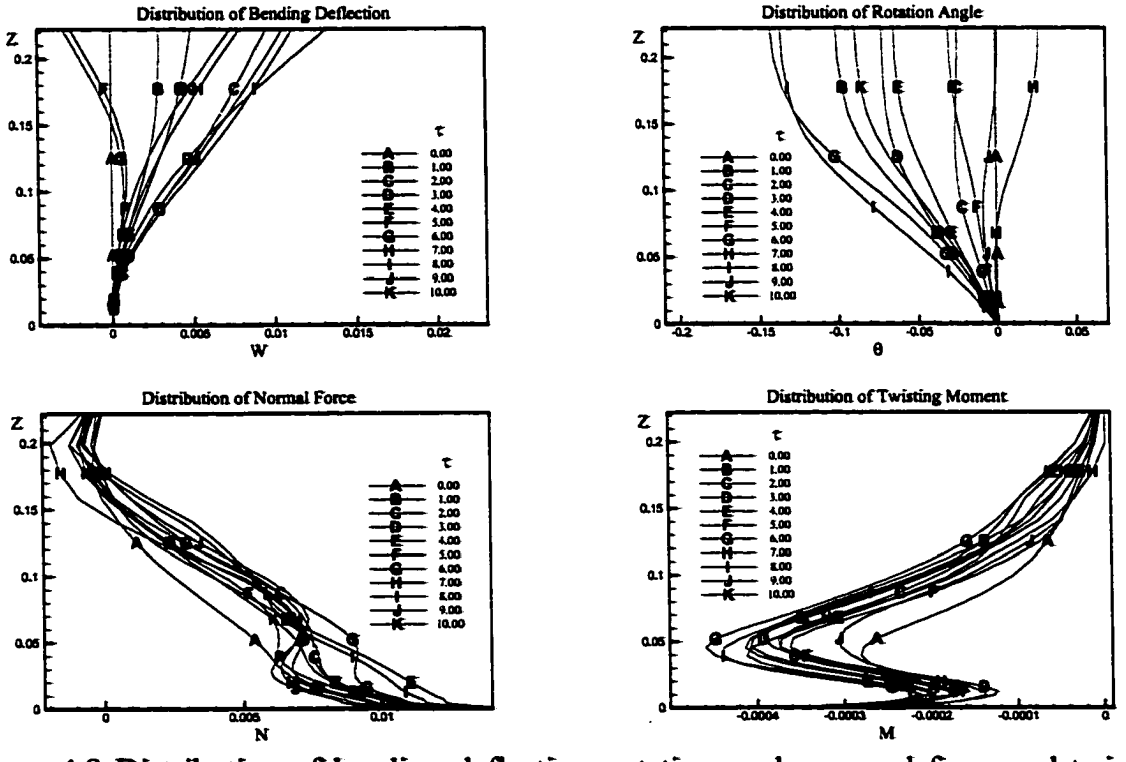

Figure 4.8 Distribution of bending deflection, rotation angle, normal force and twisting moment along the tail span. FSVC (in, 10°) case at $M_\infty = 0.3$, $\alpha = 30°$, $Re = 1.25\times10^6$.

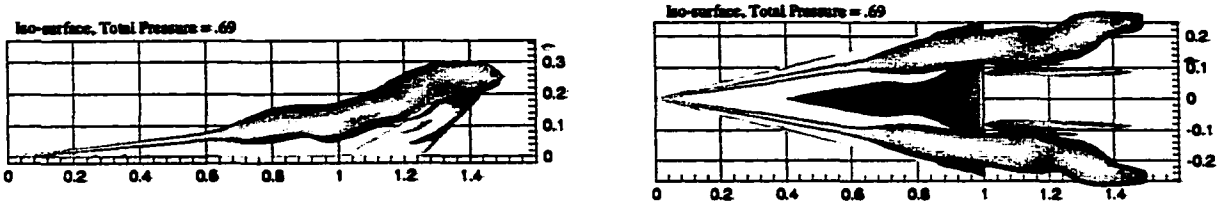

(a) Side view (b) Top view

Figure 4.9 Top view and side view showing the vortex core total pressure iso-surface. FSVC (in, -10°) case at $\tau = 19$, $M_\infty = 0.3$, $\alpha = 30°$, $Re = 1.25 \times 10^6$.

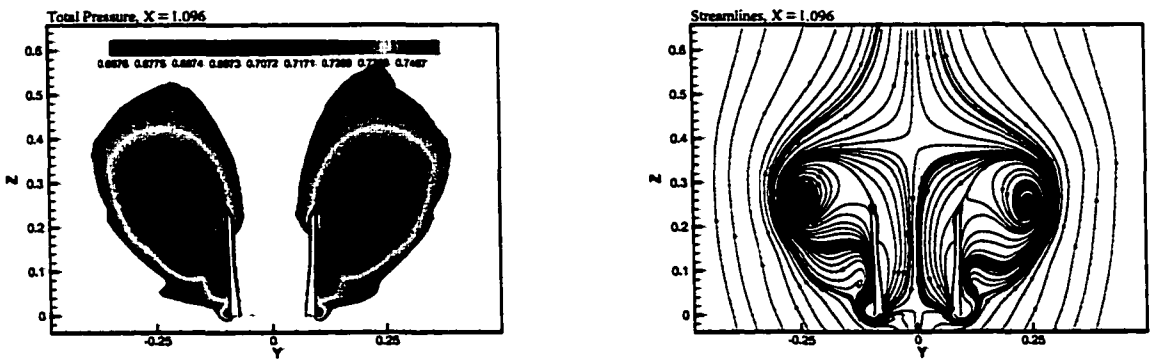

Figure 4.10 Snap shots of total pressure contours and instantaneous streamlines on cross plane, $x = 1.096$. FSVC (in, -10°) case at $\tau = 19$, $M_\infty = 0.3$, $\alpha = 30°$, $Re = 1.25 \times 10^6$.

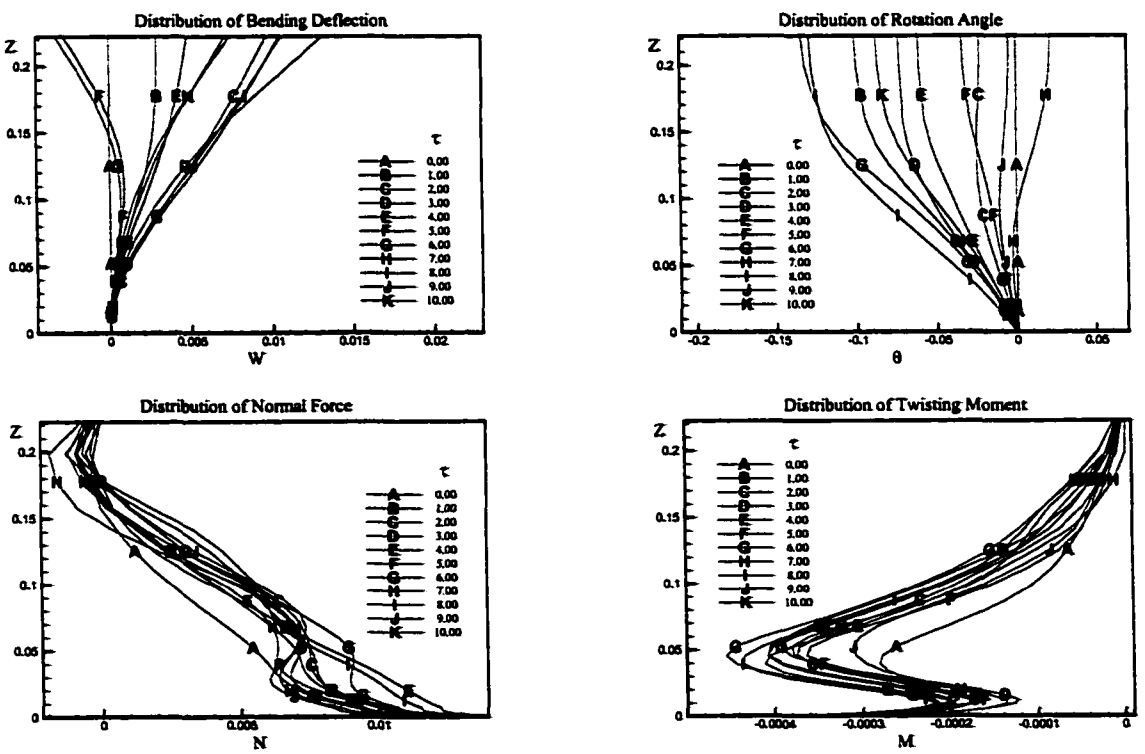

Figure 4.11 Distribution of bending deflection, rotation angle, normal force and twisting moment along the tail span. FSVC (in, -10°) case at $M_\infty = 0.3$, $\alpha = 30°$, $Re = 1.25 \times 10^6$.

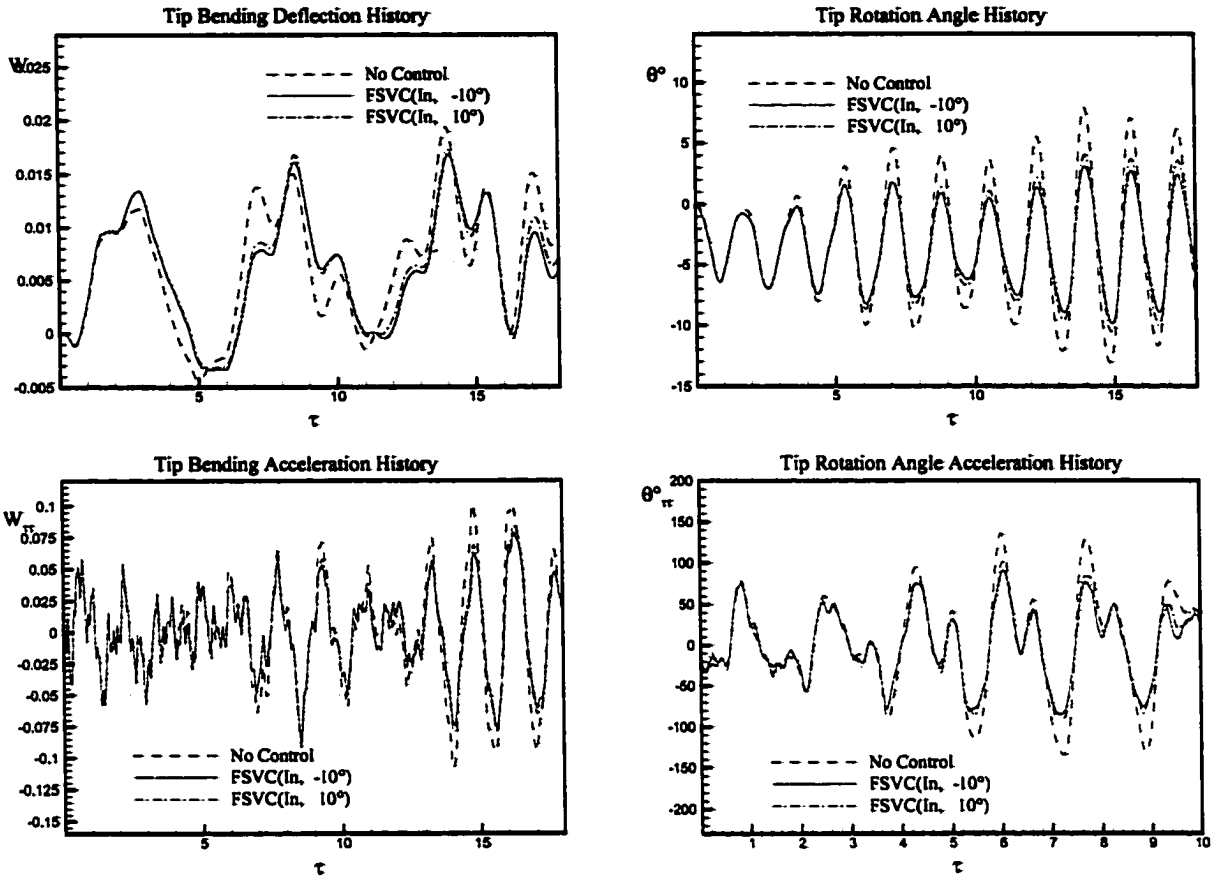

Figure 4.12 Effect of FSVC on the history of right tail tip bending and torsion deflections and accelerations for uncoupled bending-torsion modes. $M_\infty = 0.3$, $\alpha = 30°$, $Re = 1.25 \times 10^6$.

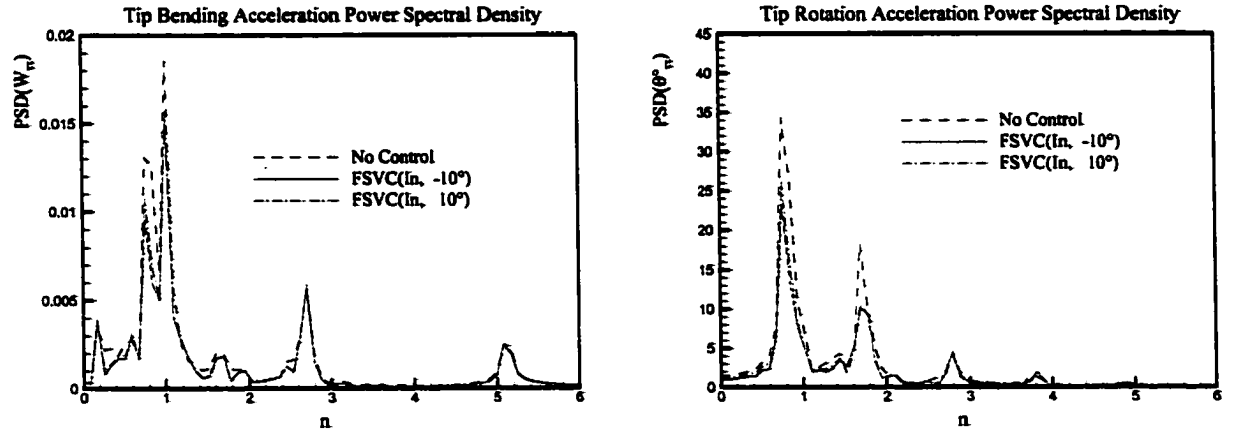

Figure 4.13 Effect of FSVC on power spectral density of right tail tip bending and torsion accelerations for uncoupled bending-torsion modes. $M_\infty = 0.3$, $\alpha = 30°$, $Re = 1.25 \times 10^6$.

4.5 Summary

The fundamental issue of twin-tail buffet alleviation is addressed using flow control methods via suction. Flow suction along the vortex cores (FSVC) of the leading edges of the delta wing of the configuration is used. The purpose of the FSVC methods is to move the location of the vortex-breakdown point in the downstream direction and the vortex-breakdown region in the spanwise direction away from the tail location. The effects of the axial orientation of the suction tubes of the FSVC methods have been investigated. The suction tubes have been tilted to the left at an angle $\varphi = -10°$ and to the right at an angle $\varphi = 10°$. The flow field results and the loads and aeroelastic results are compared with those of the no-control case. The results of the FSVC tilting methods show that the vortex-breakdown point is moved downstream, the vortex-breakdown region is moved away from the tail location, and a high total-pressure flow move in the region between the twin tails. These flow modifications produce lower tip bending and rotation angle deflections and accelerations. Moreover, the root bending and twisting moments are reduced in comparison with the no-control case. However, there is no shift in the frequencies at which the peaks of the PSD responses occur. Moreover, there are no changes in the periods or the phases of these responses. The primary effect of the FSVC methods is the amplitude reduction of the aeroelastic responses. The best control results are obtained with the suction tubes tilted at $\varphi = -10°$.

CHAPTER 5: ADAPTIVE ACTIVE FLOW CONTROL

5.1 Introduction

Adaptive active flow control for twin-tail buffet alleviation is presented in this chapter. The concept of this technique is to place control ports at certain locations of the tail surfaces. The locations of the control ports are determined by searching for the locations of maximum pressure differences across the tail surfaces. Control ports are placed at these locations and flow suction or blowing is applied through them in order to minimize the pressure difference across the tail. The volumetric flow rate at each port is proportional to the pressure difference across the tail at each location. The computational model consists of a sharp-edged delta wing and a swept-back flexible twin tail. This complex multidisciplinary problem is solved sequentially using three sets of equations for the fluid flow, aeroelastic response and grid deformation, using a dynamic multi-block grid structure. The computational model is investigated at 30° and 35° angle of attack for the inboard position of the twin tails of 33% of the wingspan. Flow field and aeroelastic results are presented, compared with the no-control case and discussed.

5.2 Computational Model: Adaptive Suction and Blowing Flow Control

The delta-wing/twin-tail configuration is the same as the one used in Chapter 4. The delta wing/twin tail configuration consists of a 76° swept back, sharp-edged delta wing (aspect ratio of one) and dynamically scaled flexible twin tail. To achieve this goal the contours of the pressure-coefficient difference are calculated for the left and right tails. A range of the high-pressure difference is determined and the corresponding cells are located. In these cells, control ports are placed. The computations for this case starts with the initial conditions that correspond to the solution of the flow field with a rigid twin tail. Next, the aeroelastic equations are turned on along with the grid displacement equations for the elastic tails. The flow control is implemented through the boundary conditions on the tail surfaces at the control ports (reference the equations of Chapter 2). The suction or blowing volume flow rate is proportional to the instantaneous pressure difference across the tail at the location of the port.

Figure 5.1 shows the difference of pressure coefficients on the tail surface without control after 11,000 time steps or $\tau = 11$. If the pressure on the outer tail surface is greater than the pressure on the inner tail surface, suction volume flow rate is applied at the outer port and an equal volume of blowing flow rate is applied at the corresponding inner port. Figure 5.2 shows different arrangements for active flow control ports on the tail. The type T and type T_2 are shown here. The locations of the active control ports are marked with black color, their distribution looks like a T-shape at the lower left portion of the tail starting from the tail leading edge.

5.3 Flow Field Results of Adaptive Flow Control

Figures 5.3 and 5.4 show snap shots of the flow field results at $\tau = 10$ after allowing the tails to move and interact with the flow. These figures show side and top view of the vortex cores total pressures iso-surfaces, total pressure contours and instantaneous streamlines on a cross-flow plane at x = 1.096, for the no-control case at α=30°. Figures 5.5 and 5.6 show the flow field results for the T type control case at the same angle of attack and time instant as that of the no control case. Figures 5.8 and 5.9 show the flow field results for the T_1 type control case at the same angle of attack and time instant as that of the no-control case.

The top view figures of vortex cores (Figures 5.3, 5.5 and 5.8) show the effect of adaptive control methods on the location of vortex-breakdown point. Compared with the no-control case, the vortex-breakdown points do not show obvious change. This is what is needed, because the purpose of using the adaptive control ports is to modify the flow field near tails and at the same time not to affect the flow field upstream.

The cross-flow-plane figures of the total pressure contours and instantaneous streamlines (Figures 5.4, 5.6 and 5.9) show substantial effects of adaptive control methods. It is observed that the vortex cores near the tail move towards the tails. Moreover, adaptive control increases the high total-pressure flow in the region between the twin tails. These modifications of flow field near the twin tails, which are produced by adaptive control, add more aerodynamic damping to the tails. The effects of these modifications will be seen in the figures of tail's structure response.

Figure 5.13 shows the time history of the root bending moment and root twisting moment. It is obvious that the control effectiveness is substantial. It is suppressing the amplitudes of their variations continuously with time with a substantial decrease in their mean level. In comparison with the no-control case, the corresponding power spectral densities of Figure 5.14 show decreases in their values at the fundamental frequency of more than 70%.

Figure 5.15 shows the time history of the absolute mass flow rate, Q, and the kinetic energy rate (power), K.E., which are needed for applying the adaptive flow control. It is observed that both Q and K.E. amplitudes are decreasing substantially with time. T_2-type control requires less mass and energy than T type control. For the configuration at $\alpha = 30°$, both T-type and T_2-type control generate good results.

Figures 5.24-27 show the aeroelastic responses of the tail for the no-control case and the present adaptive control cases at $\alpha = 35°$.

Figure 5.24 shows the time history of the tip bending and rotation deflections and accelerations. For the tip bending deflection, T type control produces much higher value compared with the no-control case. As time increases, the tip bending deflection decreases but it is still higher than the value of the no-control value. The tip bending deflection of T_2-type control case is a little bit higher than that of the no-control case at the beginning and decreases as time increases. As for the rotation angle, both types of control generate much smaller amplitude than the no-control case. The power spectral densities of the tip bending and torsion acceleration are shown in Figure 5.25. The amplitude of the tip bending acceleration at 1^{st} mode is decreased up to 40% for T type control and 50% for T_2-type control compared with the no-control case. For higher mode, T_2-type control generates higher tip bending accelerations than T-type control. Both of them are less than those of the no control case. Similar results can be observed in the figure of the power spectral density of torsion acceleration.

Figure 5.26 shows the time history of the root bending moment and root twisting moment. The control effectiveness of T_2-type control is substantial, but not for T-type control at this time. T_2-type control is suppressing the amplitudes of their variations continuously with time with a substantial decrease in their mean value level. In

comparison with the no-control case, the corresponding power spectral densities of Figure 5.27 show decreases in their values at the fundamental frequency of more than 40% for root bending moment (T_2-type) and 20% for root twisting moment (T_2-type).

Figure 5.28 shows the time history of the absolute mass flow rate, Q, and the kinetic energy rate (power), K.E., which are needed for applying the adaptive flow control. T_2-type control requires less mass and energy than T-type control. For this configuration at $\alpha = 35°$, T_2-type control generates much better results than T-type control.

Based on the results above, it is concluded the adaptive control method had shown its control effectiveness. However, the control ports must adaptively change their locations to be effective at different angles of attack.

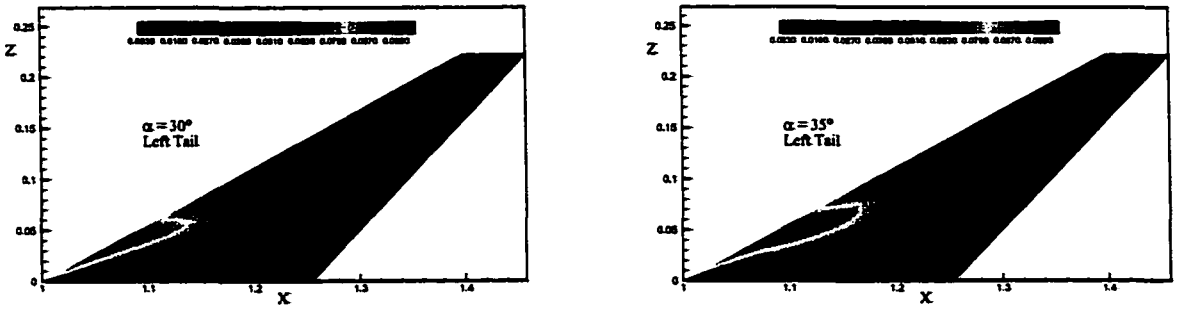

Figure 5.1 Difference of pressure coefficient contours on twin-tail surface. $M_\infty = 0.3$, $Re = 1.25\times10^6$.

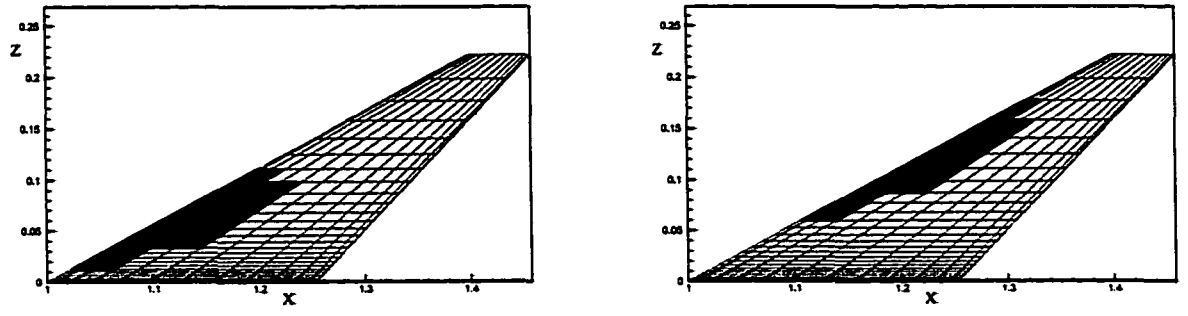

Active adaptive control (T type) Active adaptive control (T_2 type)

Figure 5.2 Schematic view showing the arrangement for active control ports.

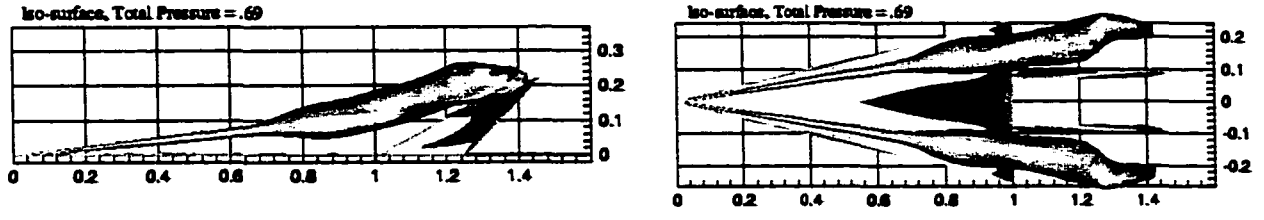

(a) Side view (b) Top view

Figure 5.3 Top view and side view showing the vortex core total pressure iso-surface. No control case at $\tau = 10$. $Ma_\infty = 0.3$, $\alpha = 30°$, $Re = 1.25\times10^6$.

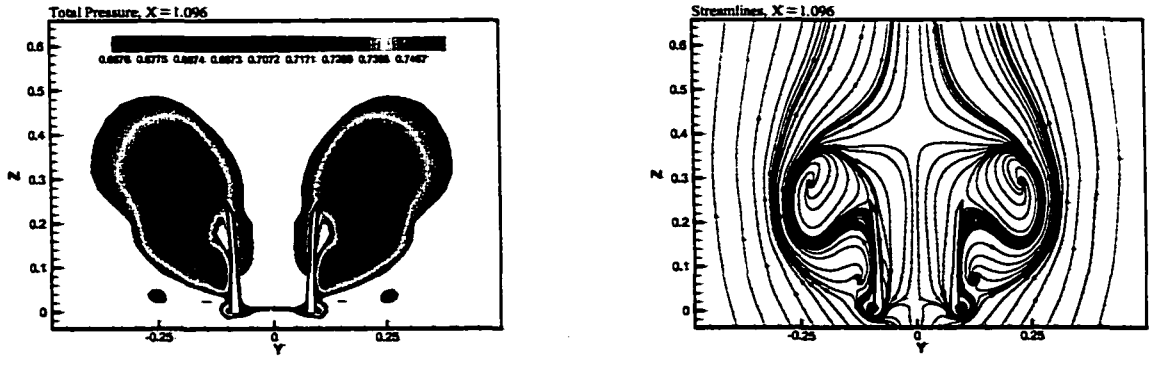

Figure 5.4 Snap shots of total pressure contours and instantaneous streamlines on cross plane, $x = 1.096$. No control at $\tau = 10$. $Ma_\infty = 0.3$, $\alpha = 30°$, $Re = 1.25\times10^6$.

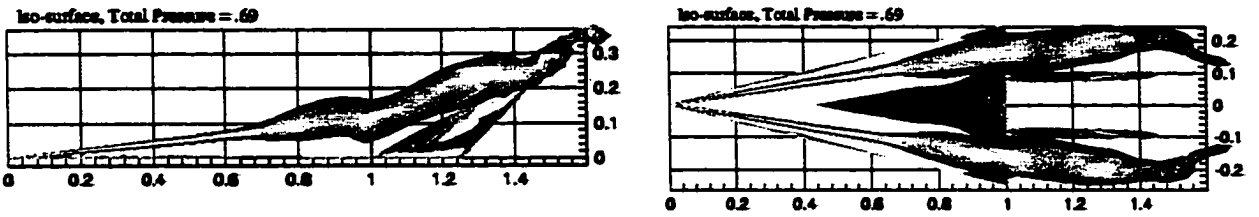

(a) Side view (b) Top view

Figure 5.5 Top view and side view showing the vortex core total pressure iso-surface. Active control (T type) at $\tau = 10$. $Ma_\infty = 0.3$, $\alpha = 30°$, $Re = 1.25\times10^6$.

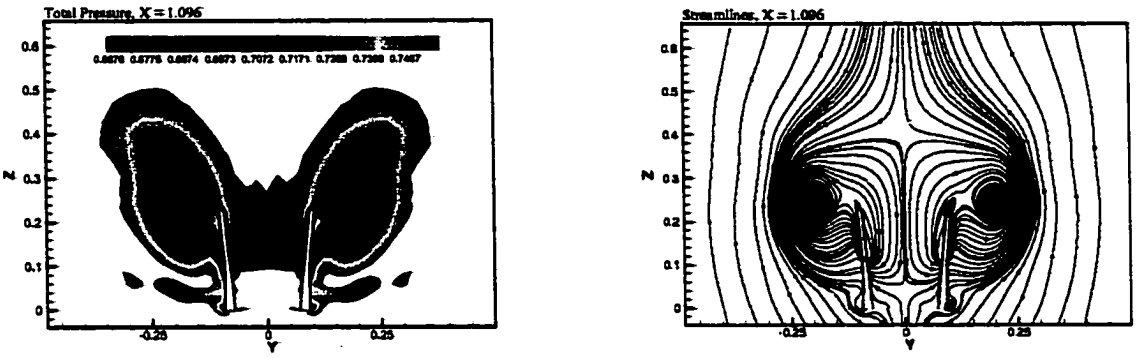

Figure 5.6 Snap shots of total pressure contours and instantaneous streamlines on cross plane, $x = 1.096$. Active control (T type) at $\tau = 10$. $Ma_\infty = 0.3$, $\alpha = 30°$, $Re = 1.25\times10^6$.

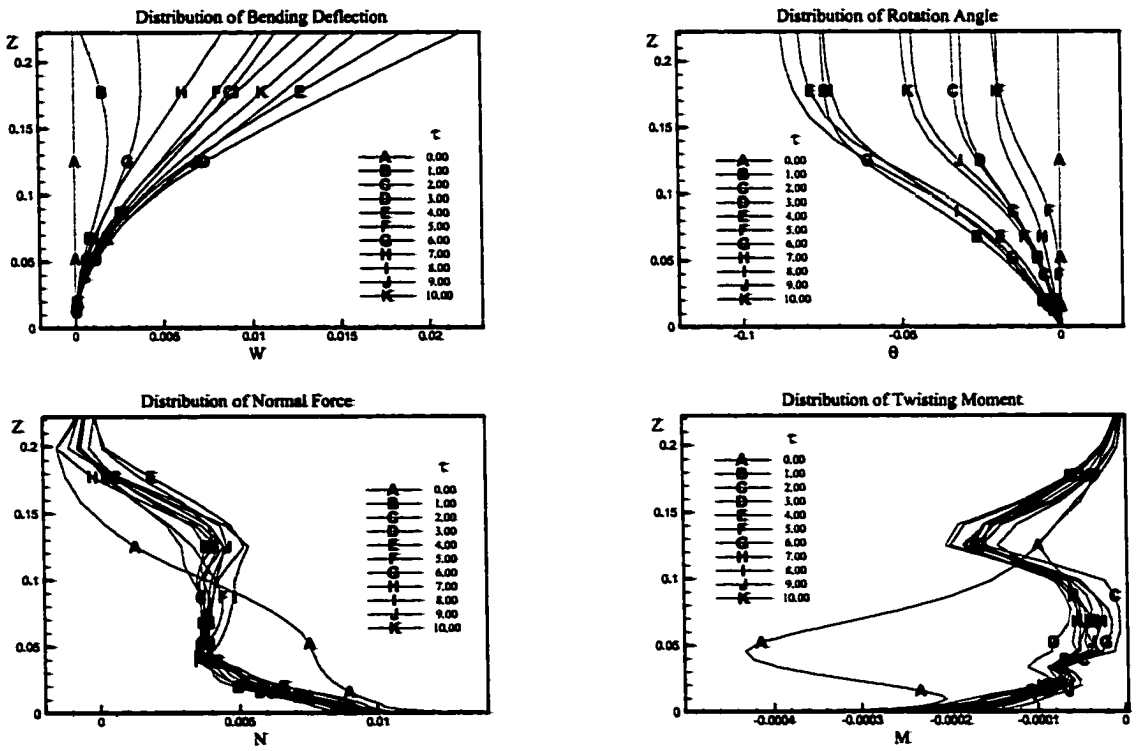

Figure 5.7 Distribution of bending deflection, rotation angle, normal force and twisting moment along the tail span. Active control (T type) at $\tau = 10$. $Ma_\infty = 0.3$, $\alpha = 30°$, $Re = 1.25\times10^6$.

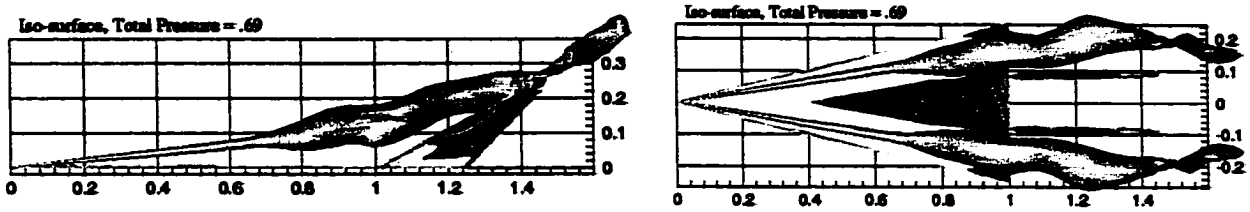

(a) Side view (b) Top view

Figure 5.8 Top view and side view showing the vortex core total pressure iso-surface. Active control (T_2 type) at $\tau = 10$. $Ma_\infty = 0.3$, $\alpha = 30°$, $Re = 1.25\times10^6$.

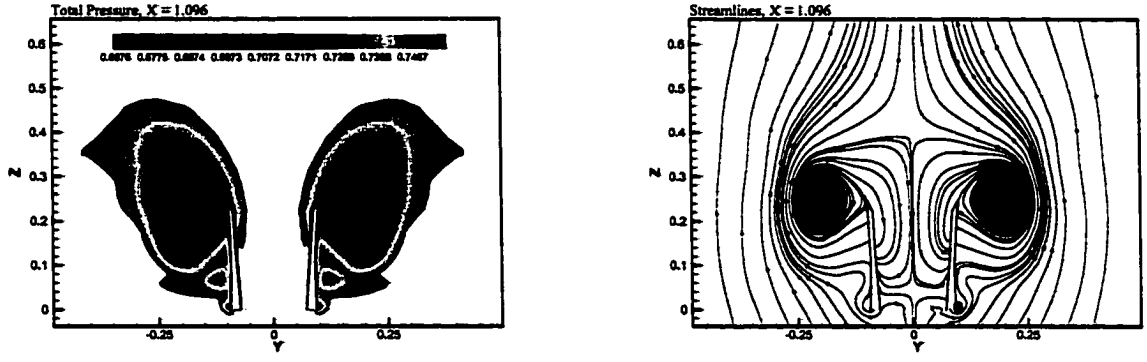

Figure 5.9 Snap shots of total pressure contours and instantaneous streamlines on cross plane, $x = 1.096$. Active control (T_2 type) at $\tau = 10$. $Ma_\infty = 0.3$, $\alpha = 30°$, $Re = 1.25\times10^6$.

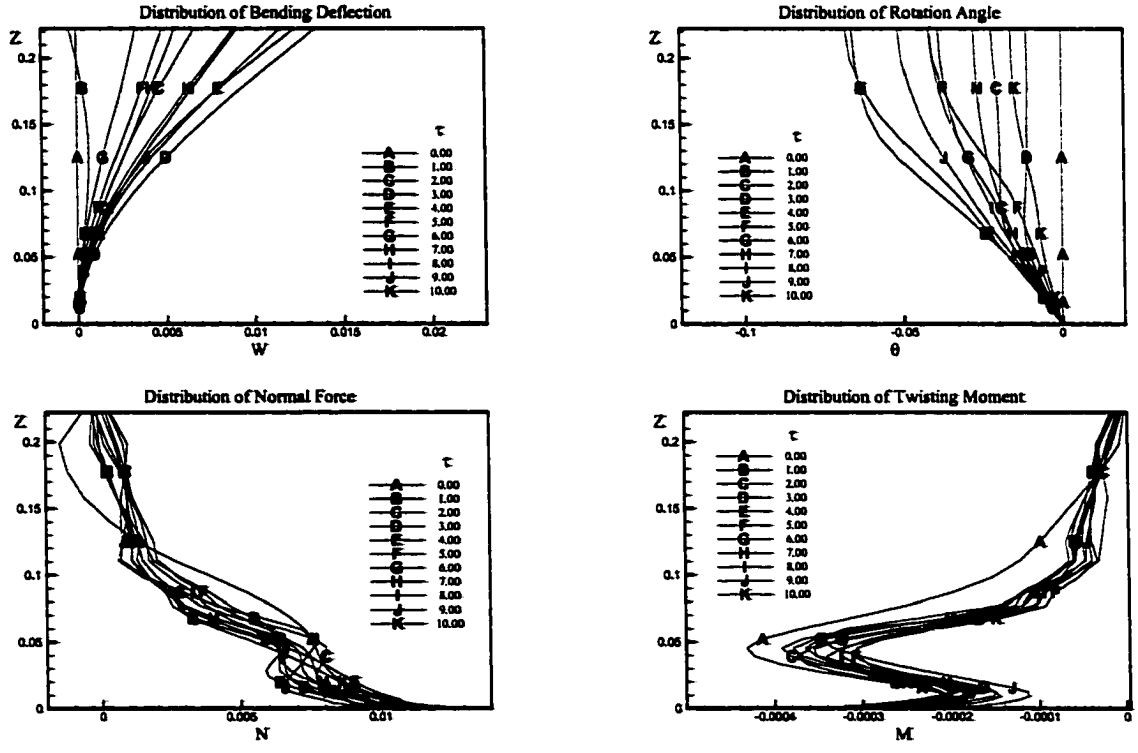

Figure 5.10 Distribution of bending deflection, rotation angle, normal force and twisting moment along the tail span. Active control (T_2 type) at $\tau = 10$. $Ma_\infty = 0.3$, $\alpha = 30°$, $Re = 1.25\times10^6$.

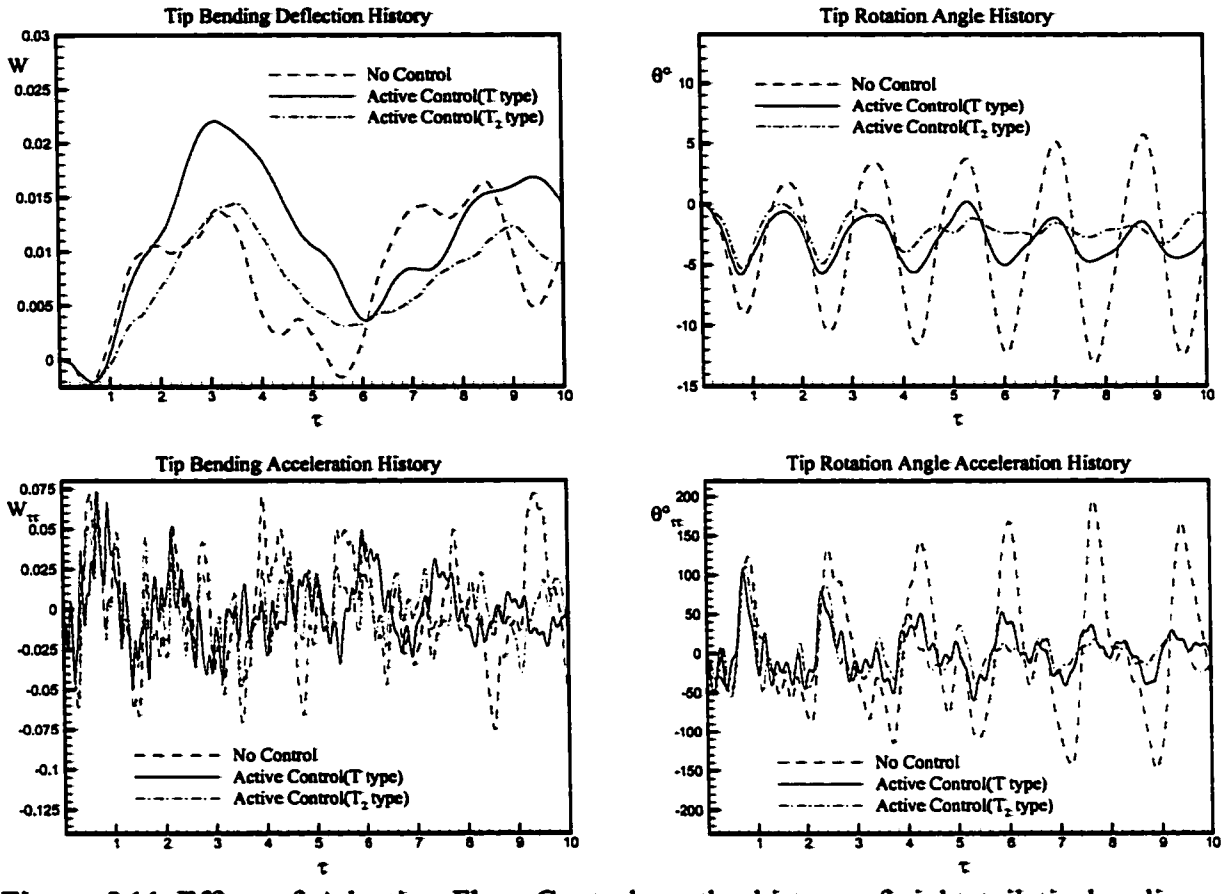

Figure 5.11 Effect of Adaptive Flow Control on the history of right tail tip bending and torsion deflections and accelerations for uncoupled bending-torsion modes. $M_\infty = 0.3$, $\alpha = 30°$, $Re = 1.25\times10^6$.

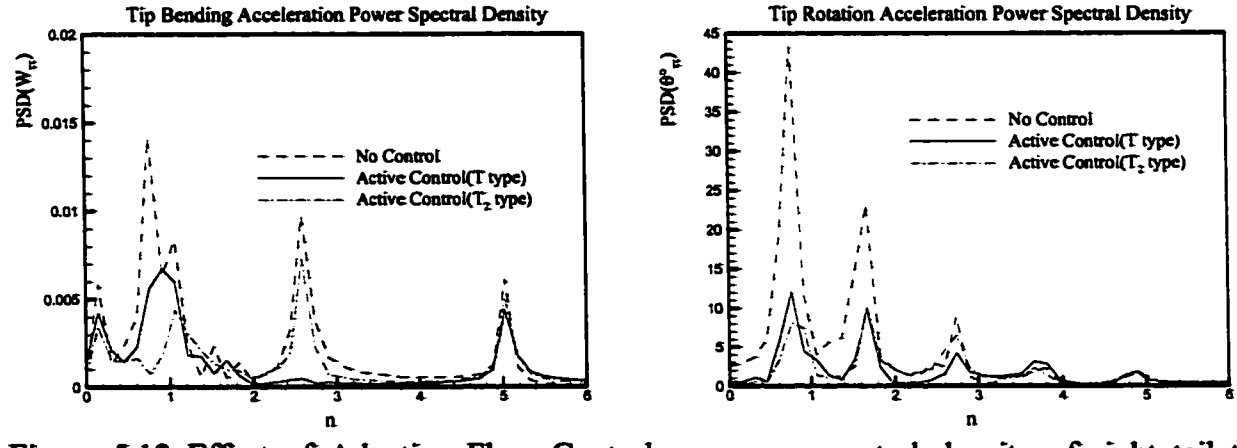

Figure 5.12 Effect of Adaptive Flow Control on power spectral density of right tail tip bending and torsion accelerations for uncoupled bending-torsion modes. $M_\infty = 0.3$, $\alpha = 30°$, $Re = 1.25\times10^6$.

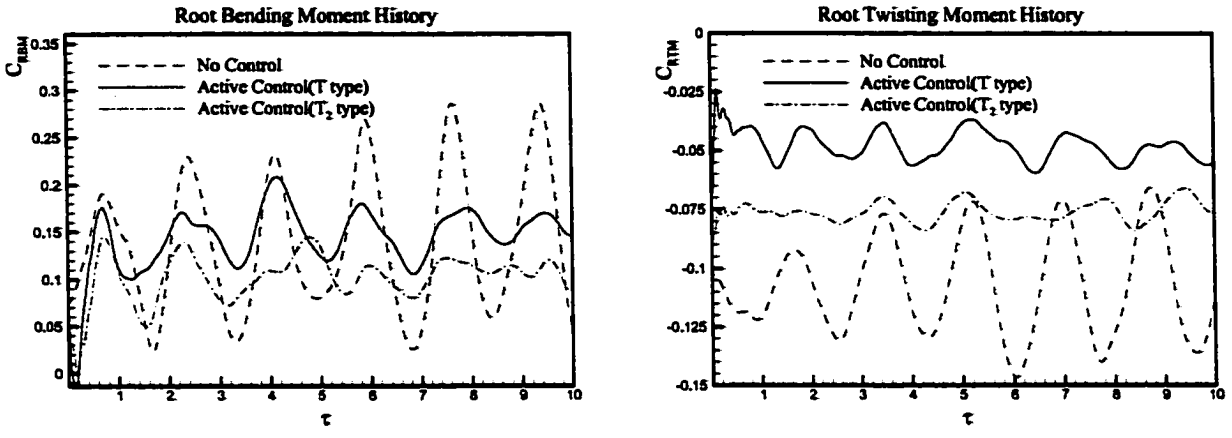

Figure 5.13 Effect of Adaptive Flow Control on the history of right tail root bending moment and twisting moment coefficients for uncoupled bending-torsion modes. $M_\infty = 0.3$, $\alpha = 30°$, $Re = 1.25\times10^6$.

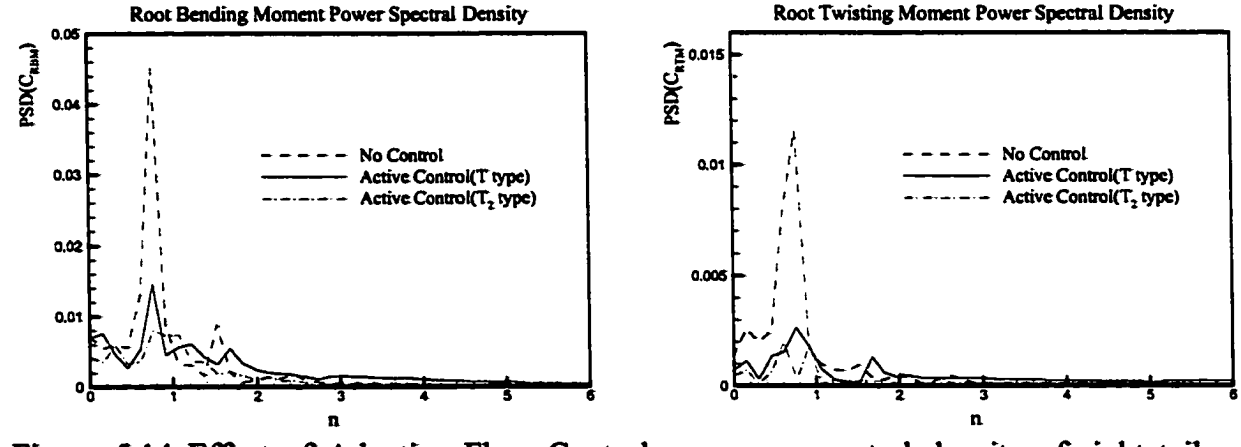

Figure 5.14 Effect of Adaptive Flow Control on power spectral density of right tail root bending moment and twisting moment coefficients for uncoupled bending and torsion modes. $M_\infty = 0.3$, $\alpha = 30°$, $Re = 1.25\times10^6$.

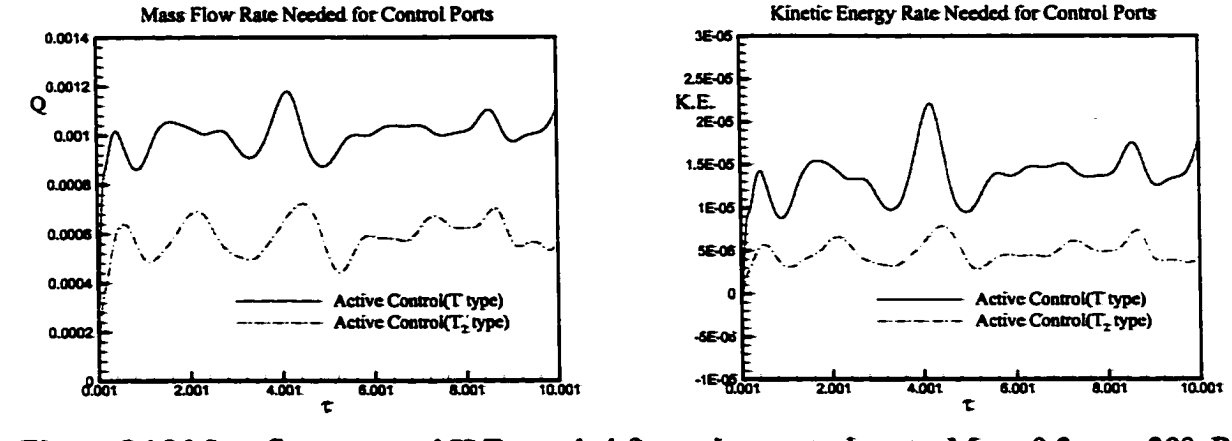

Figure 5.15 Mass flow rate and K.E. needed for active control ports. $M_\infty = 0.3$, $\alpha = 30°$, $Re = 1.25\times10^6$.

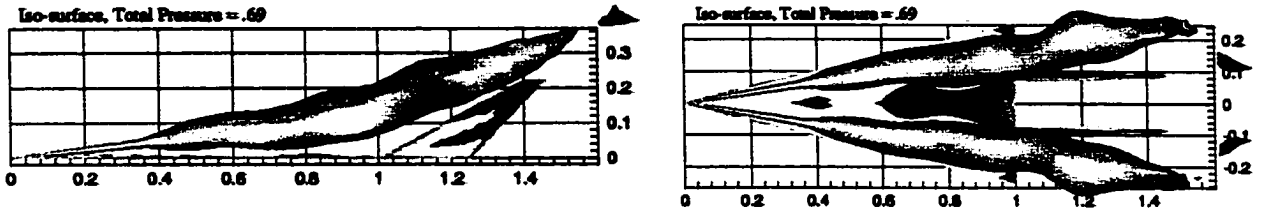

(a) Side view (b) Top view

Figure 5.16 Top view and side view showing the vortex core total pressure iso-surface. No control case at $\tau = 10$. $Ma_\infty = 0.3$, $\alpha = 35°$, $Re = 1.25 \times 10^6$.

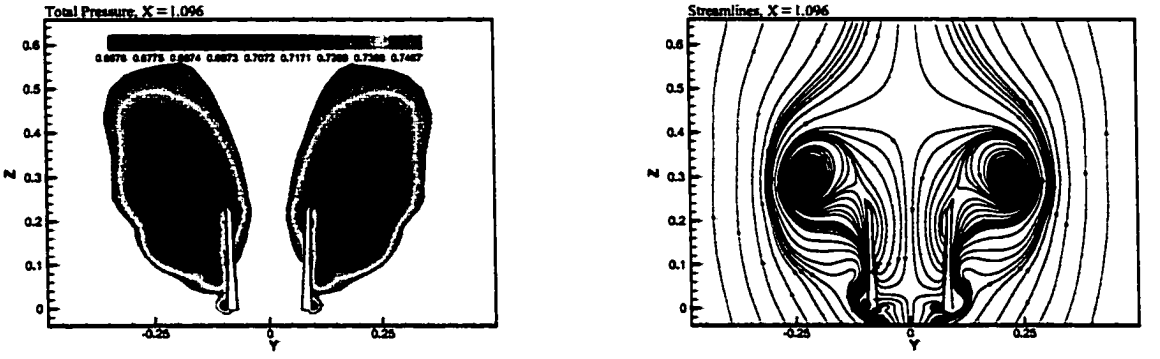

Figure 5.17 Snap shots of total pressure contours and instantaneous streamlines on cross plane, x = 1.096. No control case at $\tau = 10$. $Ma_\infty = 0.3$, $\alpha = 35°$, $Re = 1.25 \times 10^6$.

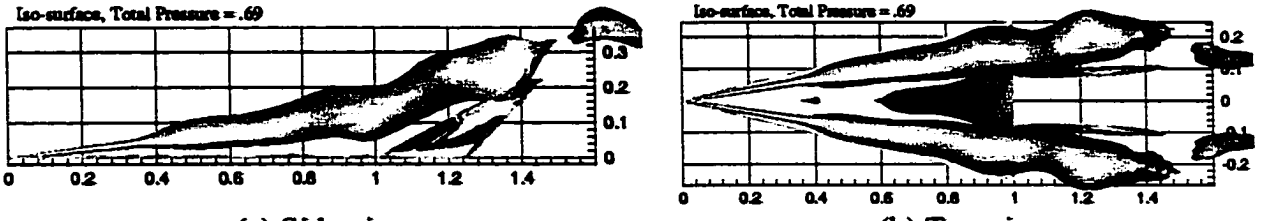

(a) Side view (b) Top view

Figure 5.18 Top view and side view showing the vortex core total pressure iso-surface. Active control (T type) at $\tau = 10$. $Ma_\infty = 0.3$, $\alpha = 35°$, $Re = 1.25 \times 10^6$.

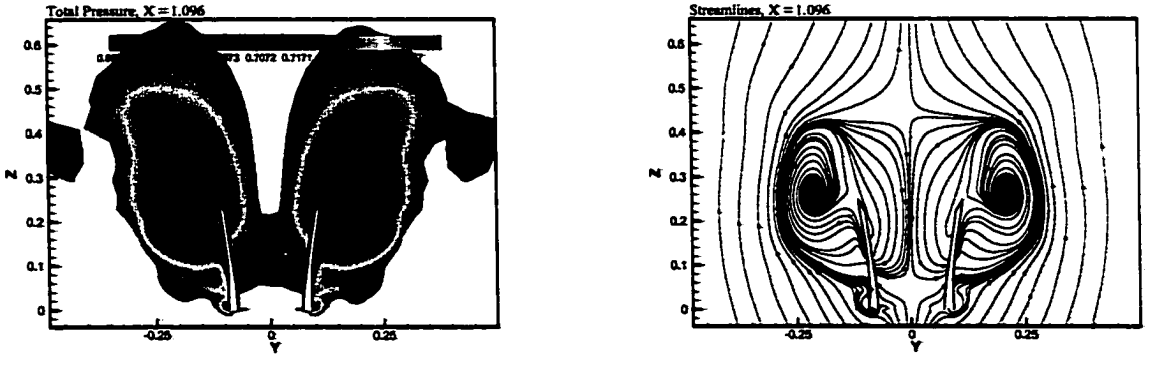

Figure 5.19 Snap shots of total pressure contours and instantaneous streamlines on cross plane, x = 1.096. Active control (T type) at $\tau = 10$. $Ma_\infty = 0.3$, $\alpha = 35°$, $Re = 1.25 \times 10^6$.

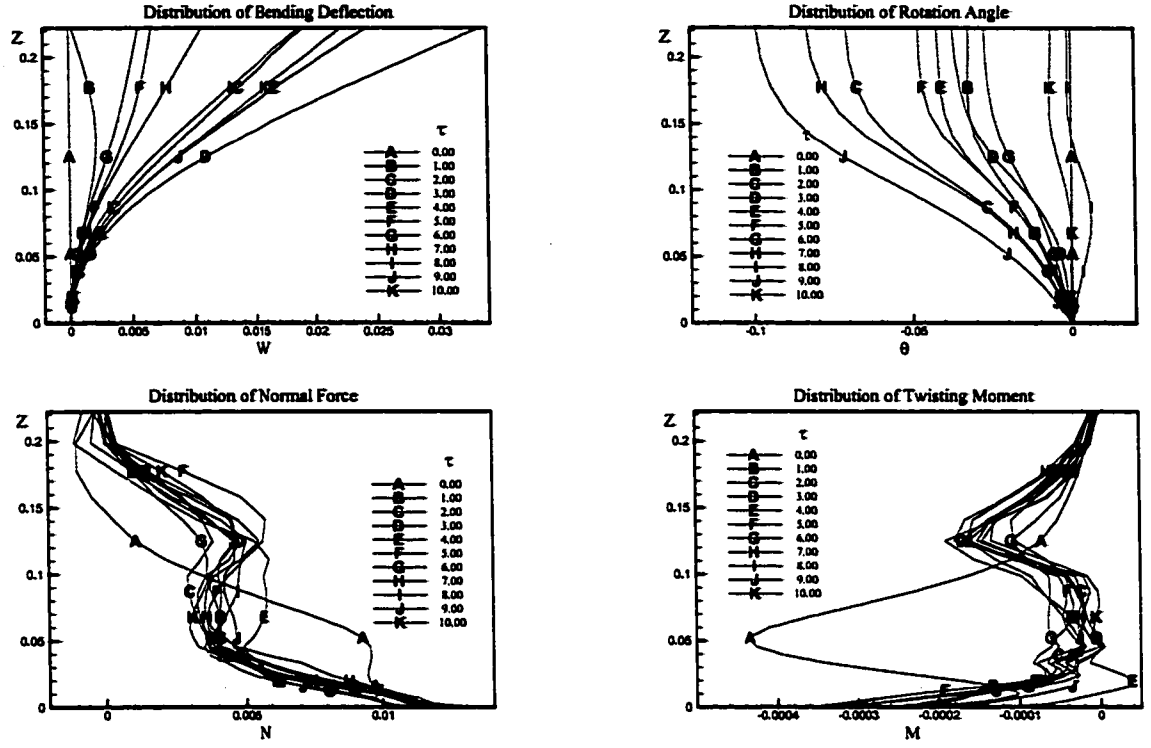

Figure 5.20 Distribution of bending deflection, rotation angle, normal force and twisting moment along the tail span. Active control (T type) at $\tau = 10$. $Ma_\infty = 0.3$, $\alpha = 35°$, $Re = 1.25\times10^6$.

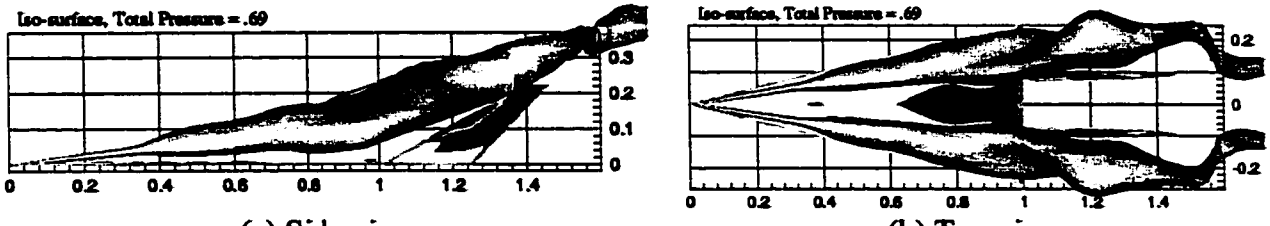

(a) Side view (b) Top view

Figure 5.21 Top view and side view showing the vortex core total pressure iso-surface. Active control (T_2 type) at $\tau = 10$. $Ma_\infty = 0.3$, $\alpha = 35°$, $Re = 1.25\times10^6$.

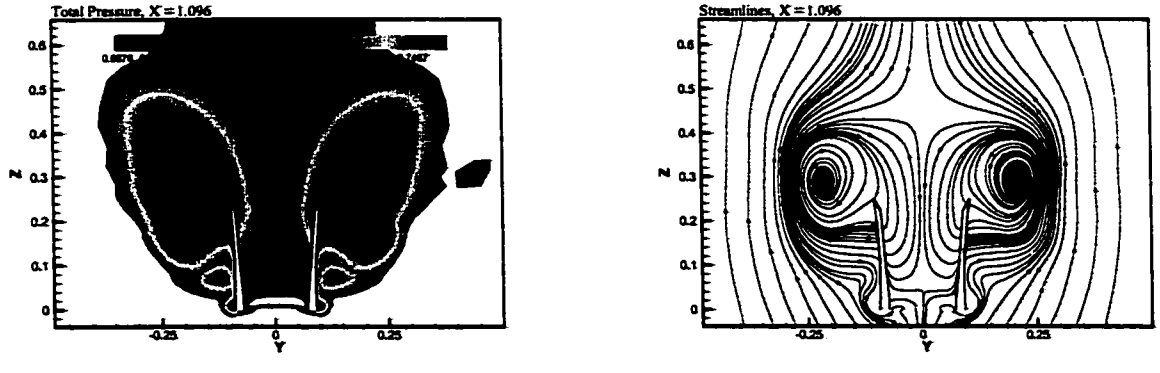

Figure 5.22 Snap shots of total pressure contours and instantaneous streamlines on cross plane, $x = 1.096$. Active control (T_2 type) at $\tau = 10$. $Ma_\infty = 0.3$, $\alpha = 35°$, $Re = 1.25\times10^6$.

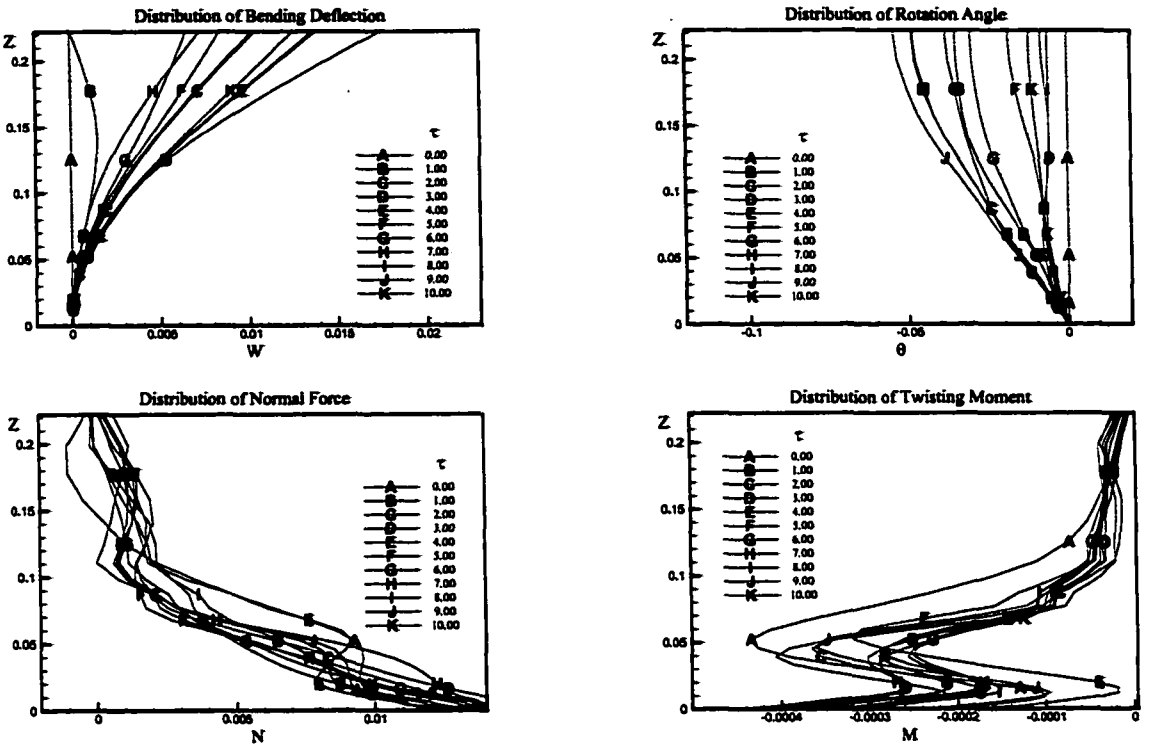

Figure 5.23 Distribution of bending deflection, rotation angle, normal force and twisting moment along the tail span. Active control (T_2 type) at $\tau = 10$. $Ma_\infty = 0.3$, $\alpha = 35°$, $Re = 1.25\times10^6$.

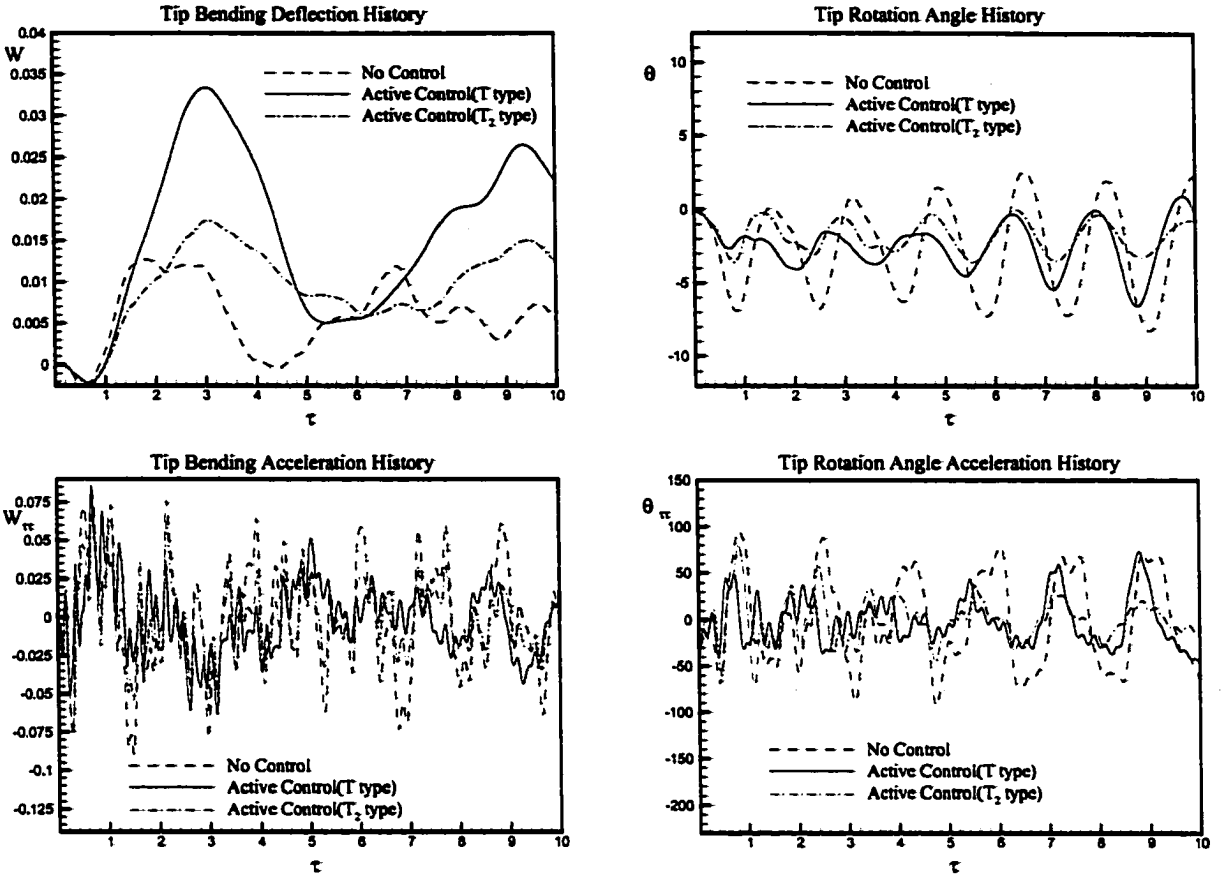

Figure 5.24 Effect of Adaptive Flow Control on the history of right tail tip bending and torsion deflections and accelerations for uncoupled bending-torsion modes. $M_\infty = 0.3$, $\alpha = 35°$, $Re = 1.25\times10^6$.

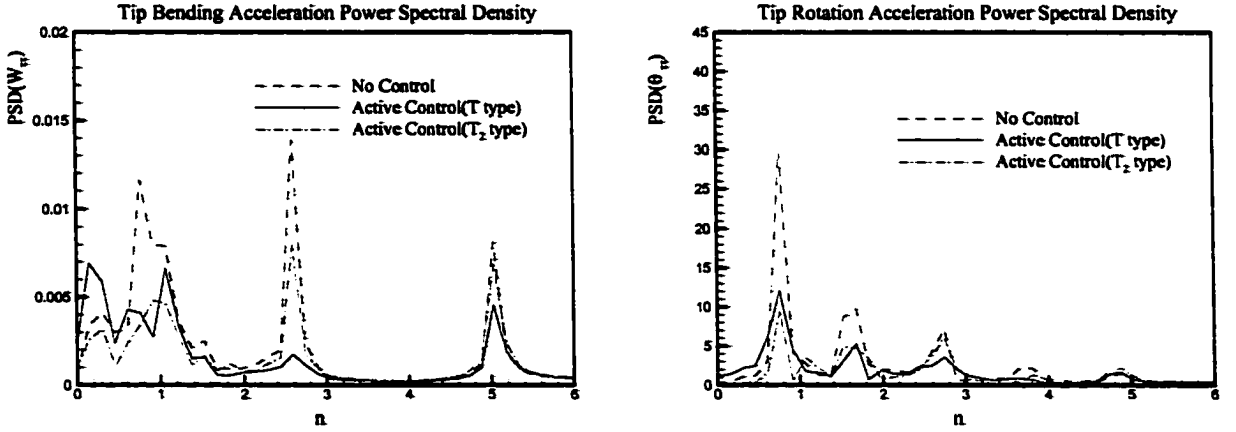

Figure 5.25 Effect of Adaptive Flow Control on power spectral density of right tail tip bending and torsion accelerations for uncoupled bending-torsion modes. $M_\infty = 0.3$, $\alpha = 35°$, $Re = 1.25\times10^6$.

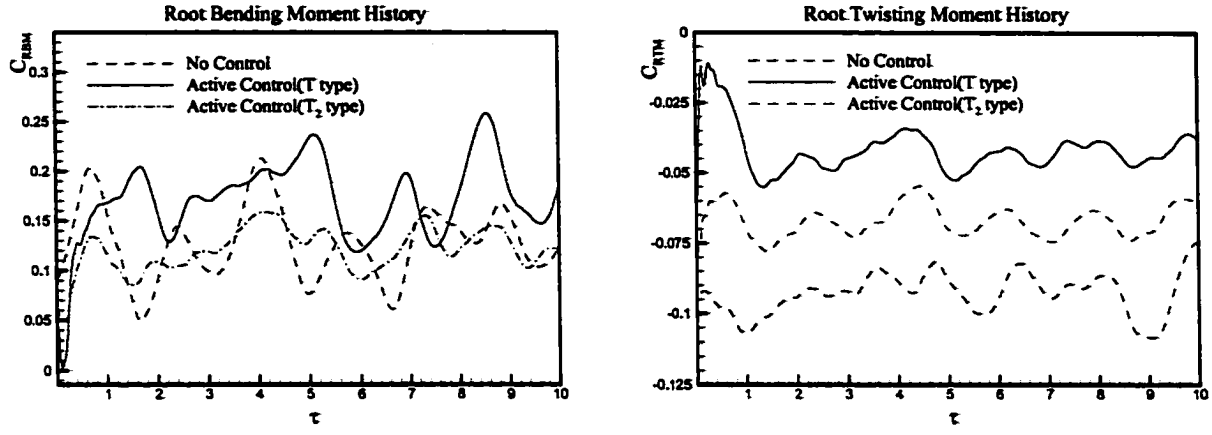

Figure 5.26 Effect of Adaptive Flow Control on the history of right tail root bending moment and twisting moment coefficients for uncoupled bending-torsion modes. $M_\infty = 0.3$, $\alpha = 35°$, $Re = 1.25\times10^6$.

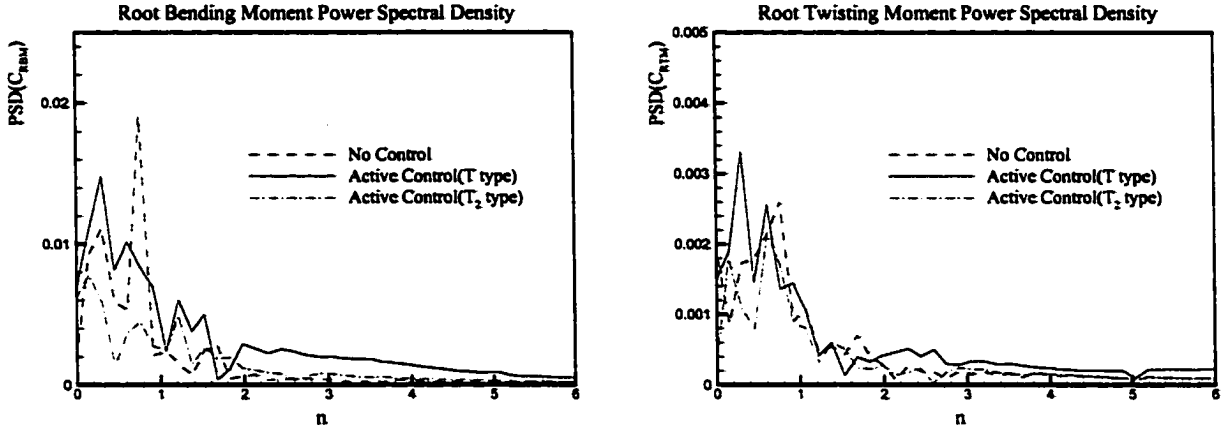

Figure 5.27 Effect of Adaptive Flow Control on power spectral density of right tail root bending moment and twisting moment coefficients for uncoupled bending and torsion modes. $M_\infty = 0.3$, $\alpha = 35°$, $Re = 1.25\times10^6$.

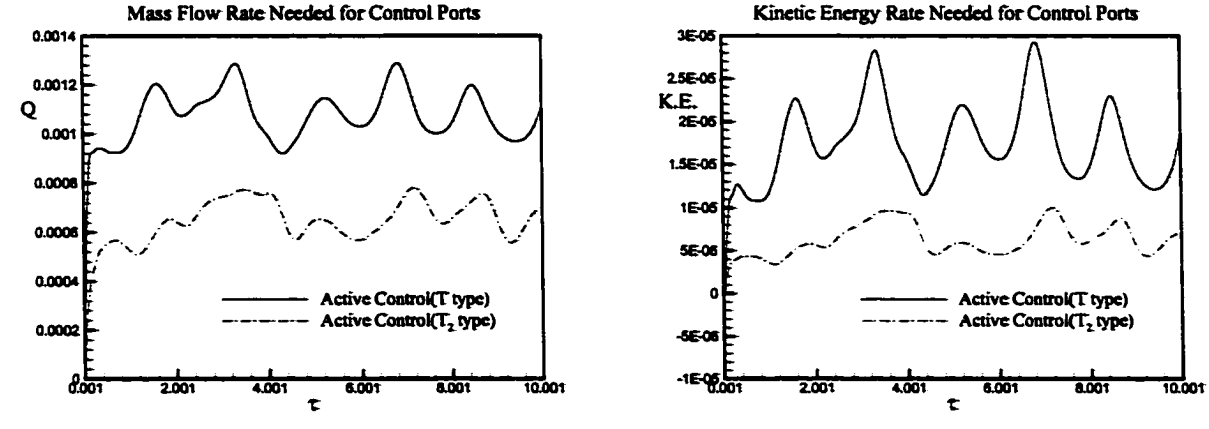

Figure 5.28 Mass flow rate and K.E. needed for active control ports. $M_\infty = 0.3$, $\alpha = 35°$, $Re = 1.25\times10^6$.

5.5 Summary

The twin-tail buffet alleviation is addressed using adaptive active flow control. The concept behind this technique is to place control ports within a small area on the tail surfaces. The locations of these control ports are determined according to the locations of a range of high-pressure difference. Flow suction or blowing is applied through these control ports to reduce the pressure differences. The suction or blowing volume flow rate from each port is proportional to the pressure difference across the tail at the location of the port.

Comparisons of the fluid flow and aeroelastic responses with those of the no-control case have shown assessments of the control effectiveness of this adaptive control technique. It has been shown that the vortex breakdown location moved further downstream. The normal force and twisting moment distributions are substantially decreased with damping of their amplitudes of variation. The bending and rotation angle responses do not change their sign. The power spectral densities of the root bending moment and root twisting moment show substantial decreases of more than 70%. The tail tip acceleration responses have shown similar decreases. The idea behind introducing the concentrated cells control is to use a small number of the control ports effectively within a small area of the tail. This is viewed as a practical design in comparison with the design complications of distributing the control ports on the whole area of the tail as was presented in Ref. 63. The problem of changing the location of control ports as the angle of attack varies can be solved by using a sliding solid plate which is moved up or down on the tail surface in order to close or open control ports as the angle of attack changes producing the T-type or T_2-type control.

CHAPTER 6: PARALLEL HIGH-ORDER CODE AND VALIDATIONS

6.1 Introduction

To investigate the flow control on tail buffet, a new parallel code based on high order compact scheme was developed. The reasons for developing a new code are: 1) Computational efficiency: The code used in chapter 4 and 5, which was based on the CFL3D code, does not have the parallel function. It is computationally prohibitive to use that code to investigate the JaVA based flow control since it needs millions of grid points. 2) Computational accuracy: The flow generated by JaVA is complex small-scale flow, which interacts with a higher-scale mean flow. Low-order scheme may introduce large artificial damping and cannot capture some small-scale but important flow.

Several cases are shown here to validate the parallel high-order compact code (PHCC) in fluid dynamics computation. There are inviscid cases, viscous cases and moving boundary cases. Results are compared with theoretical analysis, experimental results and computational results produced by other codes, including third-order upwind scheme (CFL3D, Roe scheme). These comparisons show the accuracy and efficiency of PHCC.

6.2 Code Validations

6.2.1 Advection of Vortical Disturbance

Advection of vortical disturbance is about the vortex convection in an inviscid unsteady flow. This problem was used by many researchers[126] as a testing case. It shows the scheme's capabilities of accurately predicting vortical structure convection, which is very important in direct and large eddy simulations (DNS/LES). The initial condition is imposed by setting a vortex, centered at the location (x_c, y_c), and satisfying the following relations: [126]

$$u = U_\infty - \frac{C(y-y_c)}{R^2}\exp(-\frac{r^2}{2}),\ v = \frac{C(x-x_c)}{R^2}\exp(-\frac{r^2}{2})$$

$$p = p_\infty - \frac{\rho C^2}{2R^2}\exp(-r^2),\ r^2 = \frac{(x-x_c)^2+(y-y_c)^2}{R^2}$$

where u and v are the Cartesian velocity components in x and y direction, p and R are static pressure and vortex core radius, respectively. The Mach number of the mean flow is set to 0.1. The nondimensional vortex strength parameter $C/(U_\infty R)$ is chosen to be -0.02. The density is assumed to be constant. A uniform Cartesian mesh with $\Delta x=\Delta y=0.2$ is used. The grid size is 201×161 and the time step is set to 0.004.

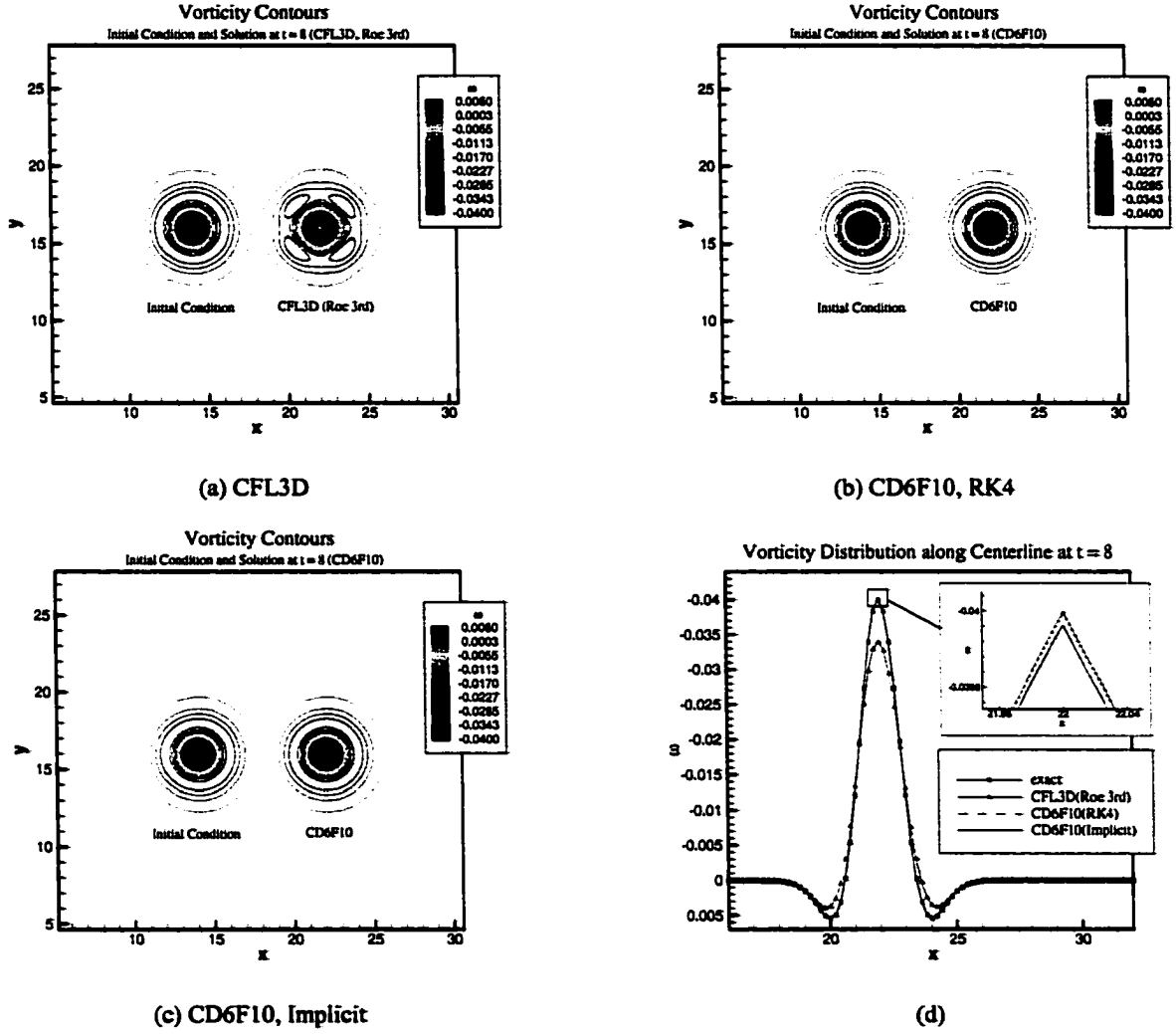

(a) CFL3D

(b) CD6F10, RK4

(c) CD6F10, Implicit

(d)

Figure 6.1 Comparison of vorticity contours and vorticity along centerline.

Figure 6.1a to 6.1c show the solution of CFL3D (Roe, 3rd order upwind), the explicit and the implicit compact scheme PHCC (CD6F10, 6th order with 10th order filter) at t = 8, respectively. Figure 6.1d shows the comparison of vorticity distribution along centerline. The results of compact scheme show good agreement with the exact solution in terms of vorticity distribution. In fact, there is no eye-seeing difference between the results of compact scheme and exact solution in figures 6.1b, 6.1c and 6.1d. The

where the wavelength $L = 2\pi/\alpha$. Figure 6.2e shows the comparison of kinetic energy growth between PHCC and CFL3D. PHCC (CD6F10) shows good agreement with linear theory. However, there are noticeable differences between linear theory result and the result produced by the CFL3D (3rd order upwind scheme). Figure 6.2f shows the vorticity contours at t=70, which is given by PHCC. A vortex is rolling up because of the developing of the small disturbance in shear flow.

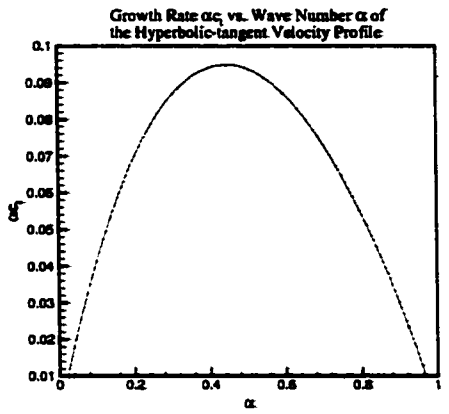

(a)

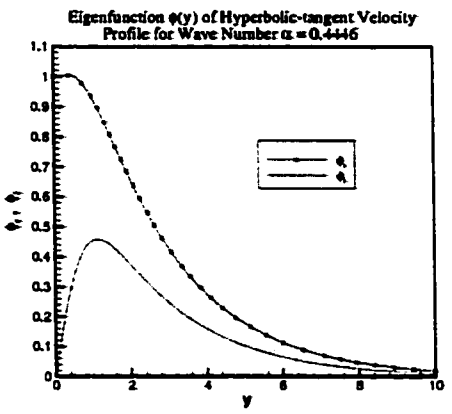

(b)

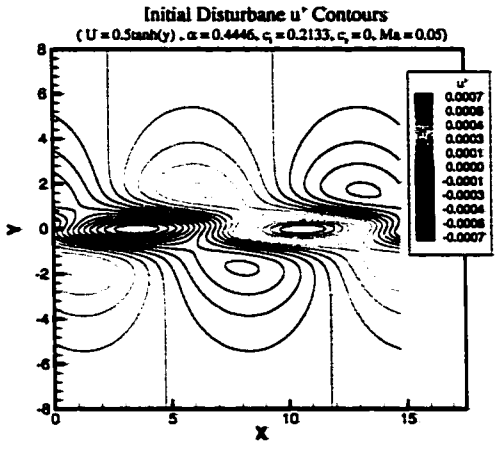

(c)

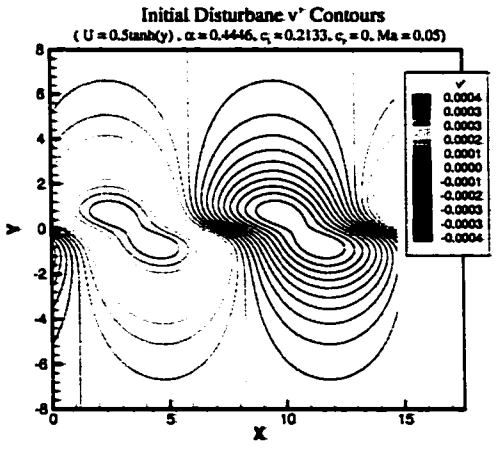

(d)

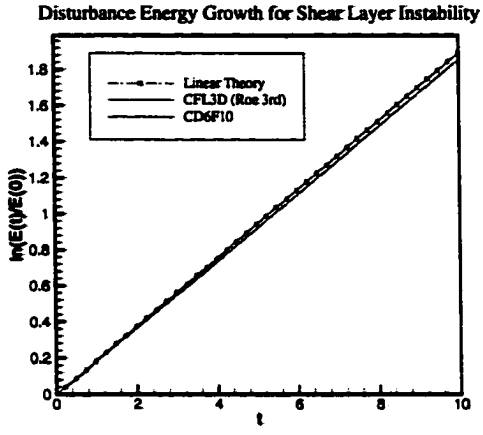

(e)

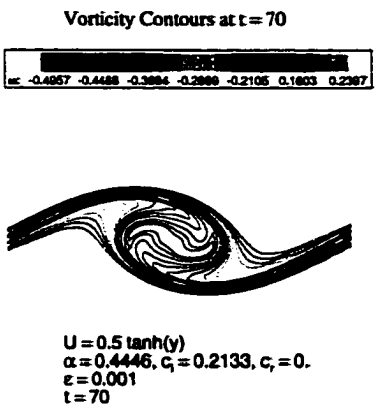

(f)

Figure 6.2 Evolution of small-amplitude disturbance in shear flow.

6.2.3 The Suddenly Accelerated Plane Wall, Couette Flow

This case shows the viscous effects on the flow formation in Couette flow. The Couette flow is generated by an impulsive motion of the lower wall in a channel. The flow in the channel is driven by the lower wall and at last reaches a linear velocity profile. The flow is assumed to be periodic in streamwise and spanwise directions. The simplified Navier-Stokes equation and the boundary conditions are

$$\frac{\partial u}{\partial t} = \nu \frac{\partial^2 u}{\partial y^2}$$

$t \le 0$: $u = 0$ for $0 \le y \le h$

$t > 0$: $u = U_0$ at $y = 0$, $u = 0$ at $y = h$

The exact solution can be found in Ref. 112, pp 92 and 278. The transient velocity distribution is

$$\frac{u}{U_0} = \sum_{n=0}^{\infty} \{\operatorname{erfc}(2n\eta_1 + \eta) - \operatorname{erfc}(2(n+1)\eta_1 - \eta)\}, \quad \eta = \frac{y}{2\sqrt{\nu t}}, \eta_1 = \frac{h}{2\sqrt{\nu t}}$$

The temperature distribution at steady status is given by

$$T - T_0 = \frac{\mu U_0^2}{2k} \frac{y}{h}\left(1 - \frac{y}{h}\right)$$

where U_0 and T_0 are the velocity and temperature of lower wall, respectively. The temperature of upper wall is assumed to be T_0. The height of channel is h. In the

calculation, the flow condition is set as Re = 1.0 and $M_w = 0.05$. The boundary conditions on the walls are set to be no-slip and isothermal conditions.

The velocity and temperature distribution at different time, which are obtained by using PHCC, are shown in Figure 6.3a and 6.3b. $\delta = 0.25, 0.5, 1.0, 1.5, 4$ corresponding to t = 0.0039, 0.0156, 0.0625, 0.1406, 0.5, respectively. They are in excellent agreement with the exact solutions (the exact solutions are not shown here because they are totally overlapped by the results of PHCC).

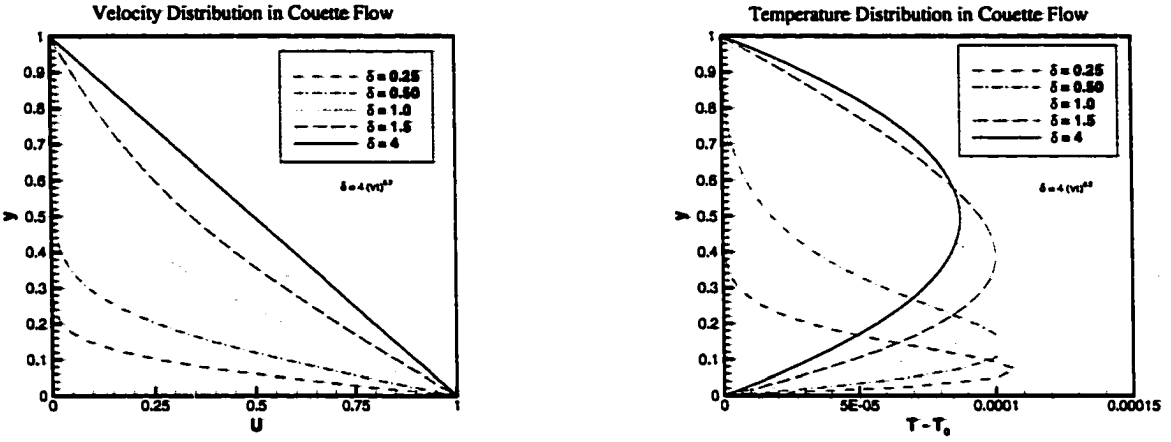

(a) (b)

Figure 6.3 Velocity and temperature distribution in Couette flow.

6.2.4 Flat Plate Boundary Layer

In boundary layer flow, the viscous effect is very important. The boundary layer flow over a flat plate is a well-known test case because its exact solution can be easily obtained. Under the incompressible assumption, the solution of the steady, laminar, flat plate boundary layer is given by Blasius equation.

$$f''' + \frac{1}{2} f f'' = 0$$

The Mach number of freestream flow is set as 0.1. Figure 6.4 shows comparison of the velocity profile between PHCC (CD6F10) and Blasius solution at different Re_x number. Results show an excellent agreement between high order compact scheme (CD6F10) and the analytic solution (Blasius solution).

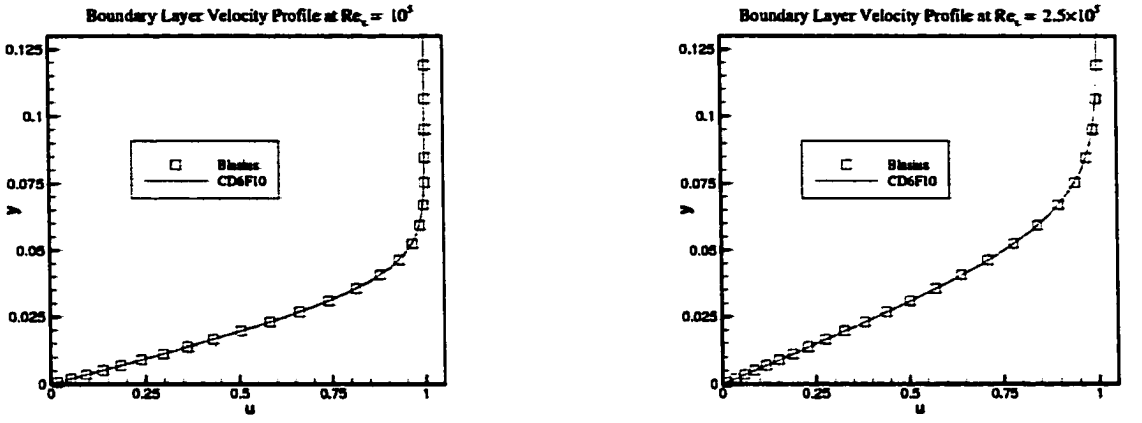

(a) (b)

Figure 6.4 Velocity profile of boundary layer flow at $Re_x = 10^5$ and 2.5×10^5.

6.2.5 Flow past a Circular Cylinder

The flow over a circular cylinder has the characteristic of simple geometry and complex flow field. A lot of experimental and numerical studies have been done and there are reviews given by Berger and Wille[8], and Williamson[134]. The flow over a circular cylinder shows the dependence on Reynolds number. There are two symmetric counter-rotating vortices behind the cylinder when Re is about 5 to 40. As the Re increases up to 190, the vortex begins to shed and forms the famous Karmann vortex street. As Re is larger than about 190, there are spanwise scales with wavelength of about four cylinder diameters[4]. When Re increases to 260, the flow generates three dimensional finer scales and the spanwise wavelength becomes about one cylinder diameter. With the increasing of Re number, the vortex street becomes turbulence. After Re is bigger than 3×10^5, the laminar boundary layer on the cylinder begins to undergo turbulence transition and wake becomes more chaotic. After the critical point $Re = 3.5\times10^6$, the boundary layer on the cylinder becomes fully turbulent and the vortex street forms again.

The two-dimensional circular cylinder calculations have been used to be a validation case for long time. When Re is larger than about 250, the three dimensional features become important and the two-dimensional calculations cannot produce accurate drag and lift coefficients[71]. So the three-dimensional calculations are necessary and are used.

6.2.5.1 Ma = 0.1, Re = 20 and 40

At Re number 20 and 40, the flow over circular cylinder is steady and consists of two symmetric counter-rotating vortices. Figure 6.5 show the results obtained by using PHCC. Figure 6.5a and 6.5b show the streamlines at Re = 20 and 40, respectively. Figure 6.5c shows the history of C_D for both cases. Table 6.1 lists the comparison of vortex length and C_D. Results obtained by PHCC display good agreement with experiment and other computational results.

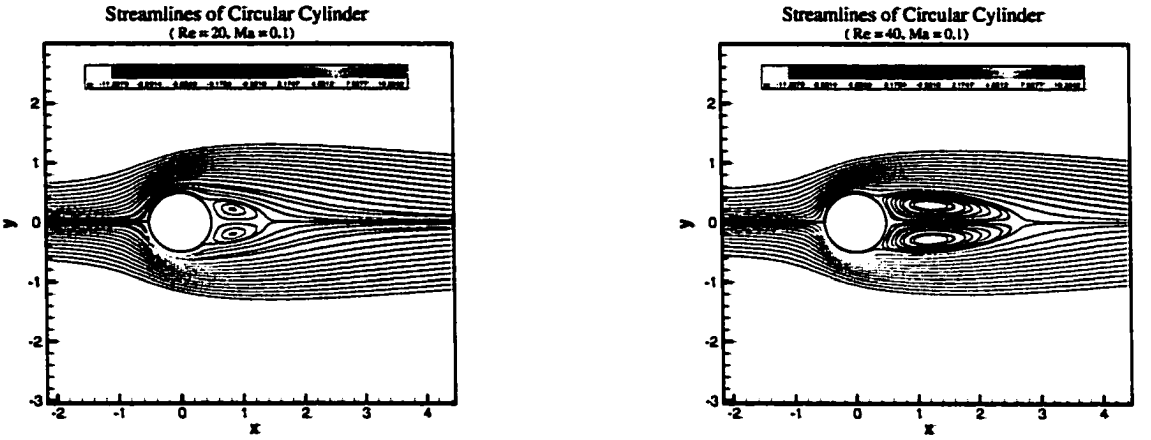

(a) (b)

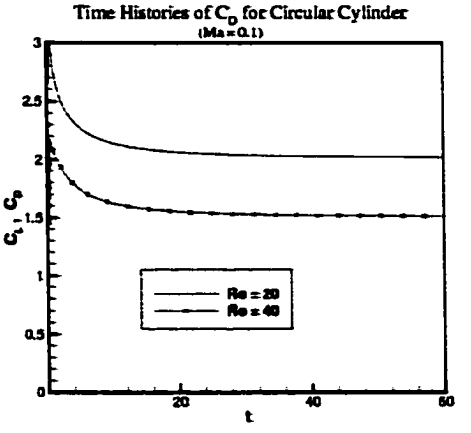

(c)

Figure 6.5 Circular cylinder flow at Re = 20 and 40.

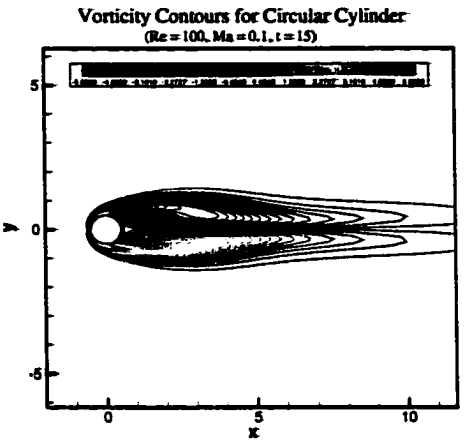

(a)

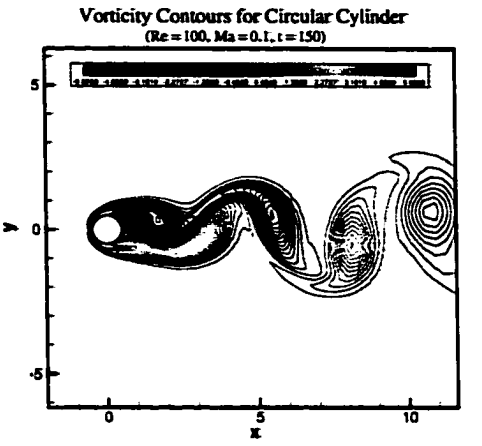

(b)

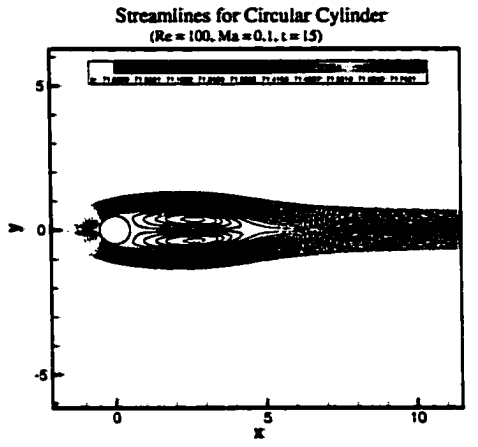

(c)

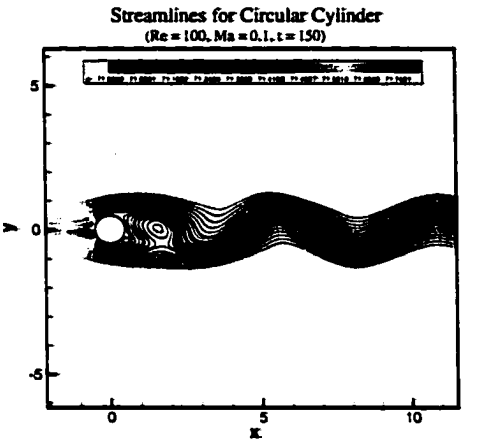

(d)

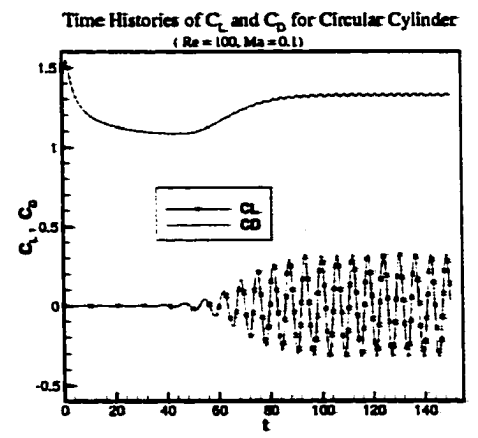

(e)

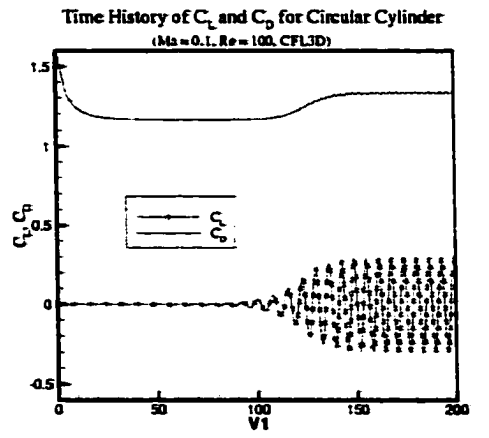

(f)

Figure 6.6 Circular cylinder flow at Re =100.

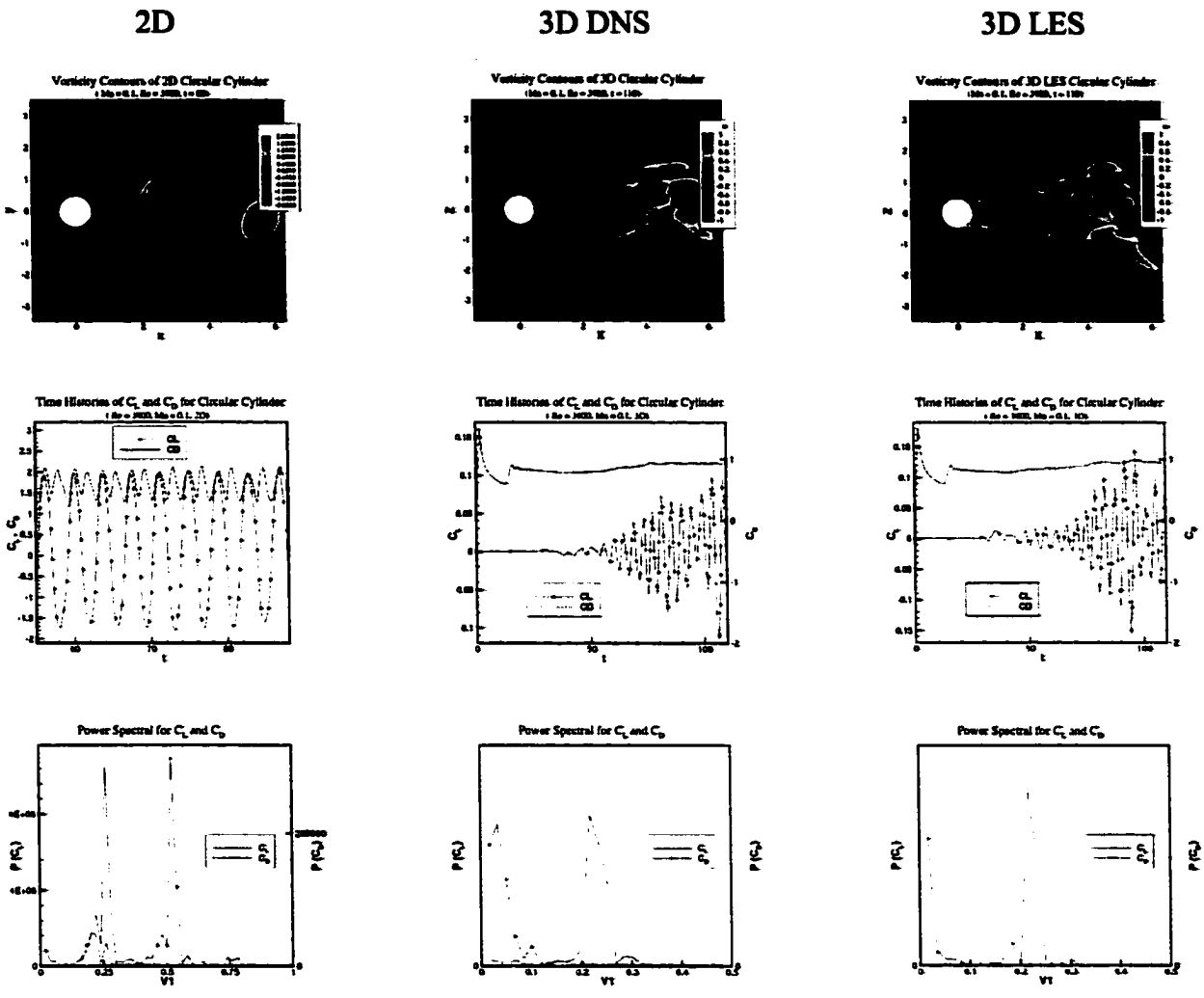

Figure 6.7 Circular cylinder flow at Re = 3900.

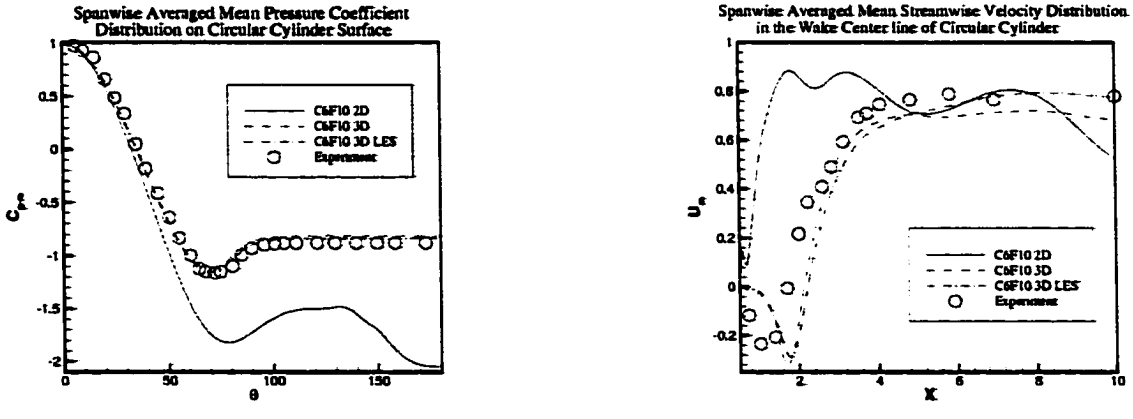

(a) (b)

Figure 6.8 Circular cylinder flow at Re = 3900.

6.2.6 Efficiency of PHCC

To test the efficiency of PHCC, tests are conducted on fix size grids. Table 6.4 lists the execution time comparison of CFL3D and PHCC. The execution time is for a viscous computation on one CPU. The 2D grid is 101×101 and the 3D grid is 146×11×161. On both 2D and 3D tests, PHCC shows that its execution time is about three times faster than that of the CFL3D. These differences are attributed to the difference scheme, small code size and better optimization of PHCC.

Table 6.4 Execution time comparison between CFL3D and PHCC.

	2D, grid 101×101		3D, grid 146×11×161	
	CFL3D	PHCC	CFL3D	PHCC
T(sec)	8.318	2.659	360.08	121.19
μs/grid point/iteration	13.59	4.344	23.21	7.811

Tests were run at a Pc with AMD Athlon 1.4G CPU.

To test the parallel speedup and efficiency of PHCC, a 3D problem with fixed size grid (181×41×129) is run on Sun E10000 parallel computer and home made cluster computer. The Sun E10000 consists of 64 nodes. The cluster computer consists of 16 nodes, but right now only six nodes (all are 2G PentiumIV) are available. The speedup and the efficiency are defined as

$$\text{speedup} = \frac{T_1}{T_n}, \qquad \eta = \frac{T_1}{n \cdot T_n}$$

where the T_1 and T_n are the wall-clock execution time on 1 and n CPUs. The execution time, speedup and efficiency on two parallel computers are list in Table 6.5 and Figure 6.9. The execution time listed in the table is for 20 time steps. There are three sub-iterations in each time step.

Table 6.5 Execution time, speedup and efficiency comparison.

N_p	Sun E10000				Cluster			
	T(sec)	μs/grid point/iteration	Speedup	η	T(sec)	μs/grid point/iteration	Speedup	η
1					405.12	7.053	1.00	1.00
2					206.68	3.598	1.96	0.98
4					113.48	1.975	3.57	0.89
6					80.724	1.405	5.02	0.84
20	395*	6.878*						

*There are lots of jobs running at E10000 and there are several jobs running in one CPU. At the normal speed these numbers should be about 130 and 2.3, respectively.

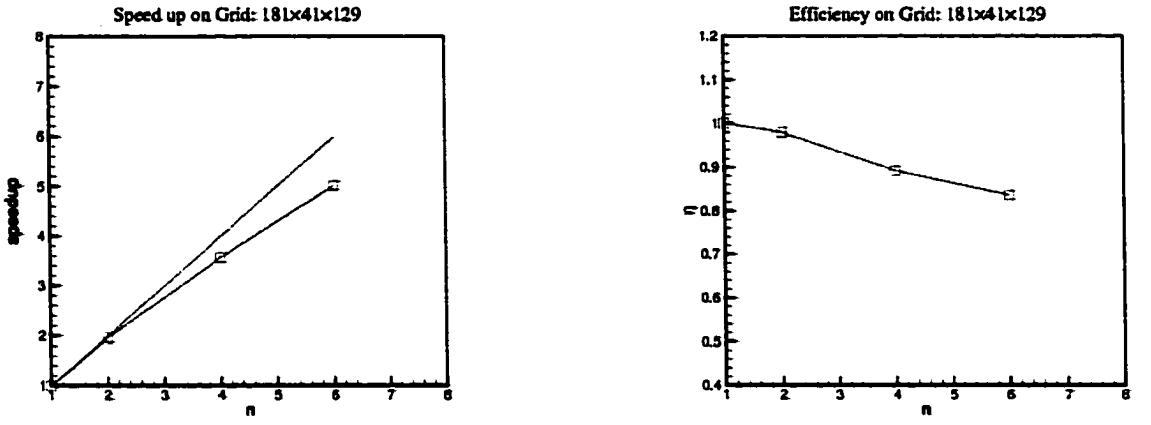

Figure 6.9 Speed up and efficiency of parallel code.

6.3 Summary

PHCC produces excellent results in the inviscid or viscous, steady or unsteady test cases. The PHCC results also show high efficiency in comparison with those of the CFL3D. The main purpose of developing PHCC is to simulate the flow control for the buffet problem of the delta-wing/twin-tail configuration by synthetic jet actuators and jet and vortex actuators, which requires: 1). Very large number of grid points because of the small size of the actuators as compared to the tail size. 2). More accurate turbulence simulation because the wake of vortex breakdown is highly turbulent, and the buffet control using actuators is an interaction among the highly turbulent wake, the tails and the actuators. PHCC can do parallel computation and can deal with large-scale computational problem with a low cost cluster of personal computers. The high order scheme used in PHCC can be coupled with LES/DES turbulence model to produce more accurate turbulence simulation.

CHAPTER 7: APPLICATIONS OF JET AND VORTEX ACTUATOR AND SYNTHETICE JET ACTUATOR

7.1 Introduction

To improve the aerodynamics and structural dynamics performance of aircraft, many flow control methods have been developed and used. These methods can be cataloged as passive flow control and active flow control. Passive flow control includes the use of stationary fences, strakes and flaps. Passive flow control methods have the advantages of being simple, low cost and easy to manufacture. But there are two significant disadvantages: passive flow control cannot be optimized for multiple flight conditions and passive flow control methods may add drag when control is not needed. Active flow control has the potential to minimize both disadvantages because active flow control can be adjusted for optimizing overall flight conditions. In the previous two chapters, methods of active flow control are introduced. They are blowing and suction, which need additional air, pump and pipe. A primary goal of active control is to develop efficient actuators. One of the promising candidates is the zero-net-mass flux system, which only needs electric input and does not require external plumbing. Therefore, vehicle weight would not be increased and the design might be relatively simple. There are two types of zero-net-mass devices: synthetic jet actuator, and jet and vortex actuator (JaVA). The mechanisms of generating vorticity are different for the synthetic jet actuator and JaVA. JaVA does not rely on external flow to generate a vortex, but synthetic jets use the interaction with an external flow to generate vorticity. In addition, the JaVA operates over a range of amplitudes and frequencies, potentially allowing control over different flight regimes.

This chapter presents the computational simulations of the JaVA induced flow. As mentioned early in Chapter 2, the JaVA consists of a cavity with a plate, which serves as the actuator surface and is driven by a mechanical driver (a shaker) or a piezoelectric driver. The actuator plate acts as a piston pumping air out of the cavity on the down-stroke and sucking air into the cavity on the upstroke. Previous research work[80, 81] indicated that the actuator produced several flow fields (free jet, wall jet and vortex flow) according to amplitudes, frequency and slot spacing. Figure 7.1 shows the ranges of these

flow fields as a function of the Reynolds number, Re, and the scaled amplitude of the actuator plate, S_a. Figure 7.2 shows a typical time-averaged visualization for the flow field produced by JaVA operating in vortex flow mode.

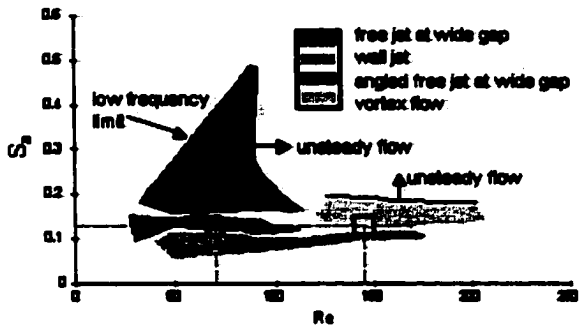

$g_r = 3$ (b = 9.65mm)

Figure 7.1 Flow fields produced by JaVA[80].

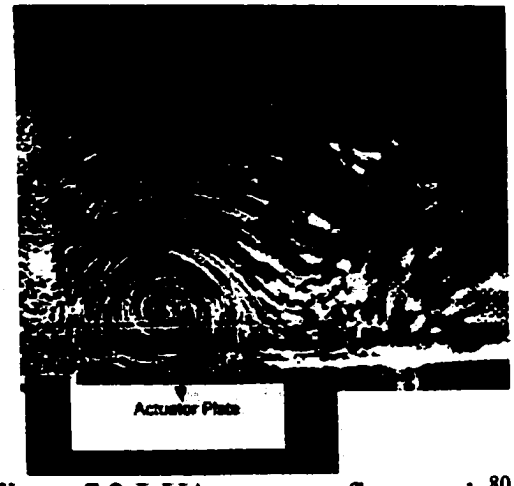

Figure 7.2 JaVA at vortex flow mode[80].

Next, the flow induced by the synthetic jet actuator is presented as a comparison. The application of the synthetic jet and JaVA for flow control is investigated. Buffet alleviation by using synthetic jet and JaVA is presented.

In this chapter, the computational simulations of JaVA (section 7.2) are conducted by using INS2D, an incompressible code, because of the very low Mach number of the flow. Other simulations are conducted by using PHCC.

7.2 Validation of Jet and Vortex Actuator Flows

7.2.1 Computational Model and Grid

The computational model of jet and vortex actuator consists of a cavity, an oscillating plate and the external region. To simulate the flow field induced by JaVA, three multi-block grids are used in the two-dimensional computation. These blocks are 213×253 (red region), 65×165 (green) and 79×165 (blue). The block adjacent to the actuator plate moves with the plate motion. The grid near the solid wall is refined.

The cavity depth is 0.5in. The thickness and width of the oscillating beam are 0.044in and 0.38in, respectively. The width of wide slot is 0.0376in and the width of the narrow slot is about 0.004 ~ 0.005in. The grids are nondimensionalized by the width of oscillating plate.

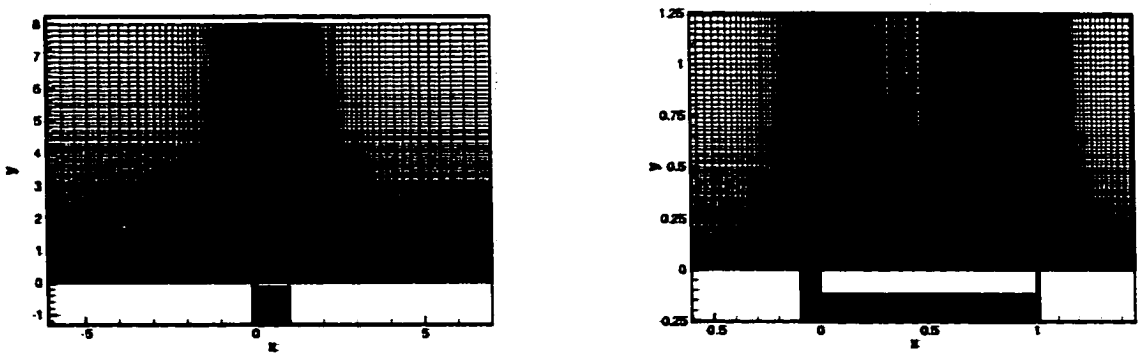

Figure 7.3 The multi-block grid used to simulate JaVA.

7.2.2 Flow Field Validation

With different combinations of the amplitude, frequency and slot spacing, jet and vortex actuator (JaVA) can generate several flow types, including free jet, wall jet and vortex flow. Two types of flow applications, a vortex flow and a jet flow, are presented.

Vortex Flow

The first case presented is the vortex flow, which corresponds to the green rectangle in Figure 7.1. The main parameters for the vortex case are:

$$f = 190Hz \qquad Re = 146 \qquad Sa = 0.13$$

Figure 7.4 shows the time-averaged visualization of the experimental work, which was conducted by Lachowicz et al.[80], for the vortex flow. Figures 7.5a – 7.5h show the average velocity contours from 1st cycle (referring to the actuator plate cycle) to 8th cycle, respectively. The development of the vortex flow is generated from 1st cycle to 8th cycle. The size and center of the computed vortex shown in Figure 7.5h are in good agreement with the experimental result shown in Figure 7.4.

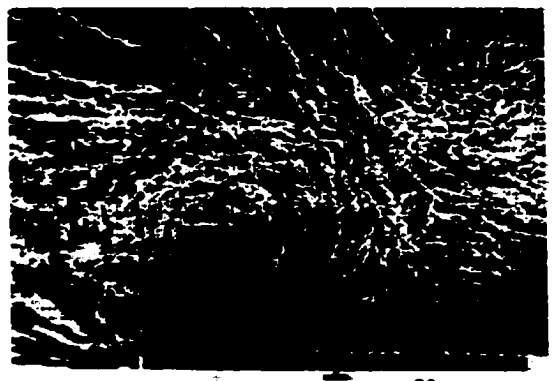

Figure 7.4 Time-averaged visualization for vortex flow[80].

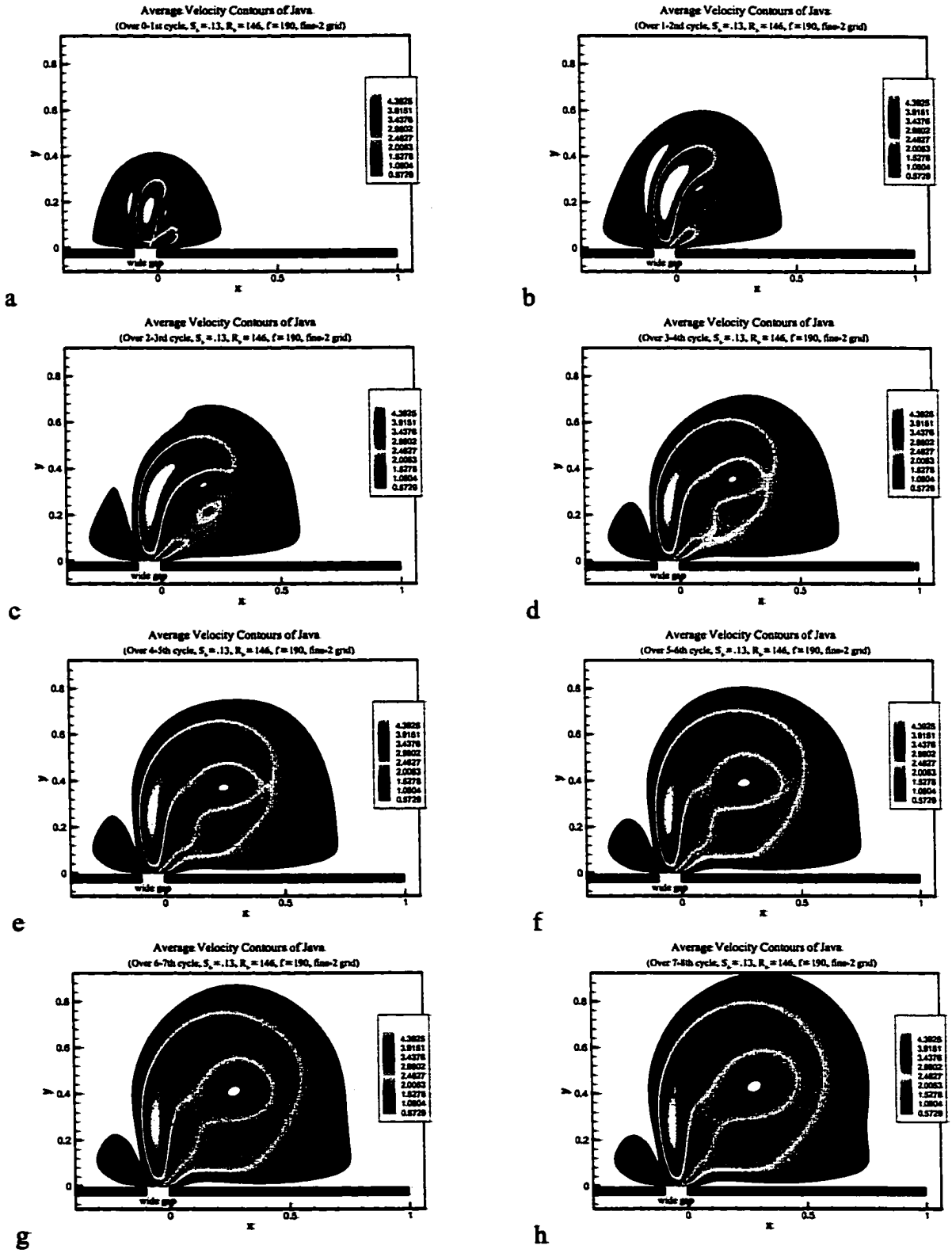

Figure 7.5 Computational simulations of JaVA flow field for vortex flow.

Jet Flow

The second flow presented is the angle free jet flow, which corresponds to the green circle in Figure 7.1. The main parameters for the angle free jet flow are:

$$f = 70Hz \qquad Re = 56 \qquad Sa = 0.13$$

Figure 7.6 shows the time-averaged visualization of the experimental work, which was conducted by Lachowicz et al.[80], for the jet flow case. Figures 7.7a – 7.7h show the average velocity contours from 1st cycle to 8th cycle, respectively. The development of the angle free jet flow is shown from Figure 7.7a to Figure 7.7h. The angle of the free jet shown in Figure 7.7h is in good agreement with the experimental result shown in Figure 7.6.

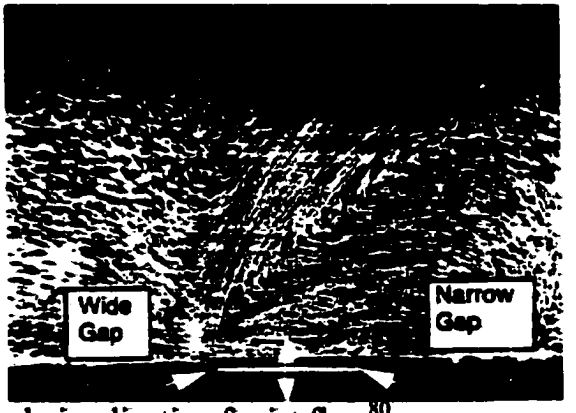

Figure 7.6 Time-averaged visualization for jet flow[80].

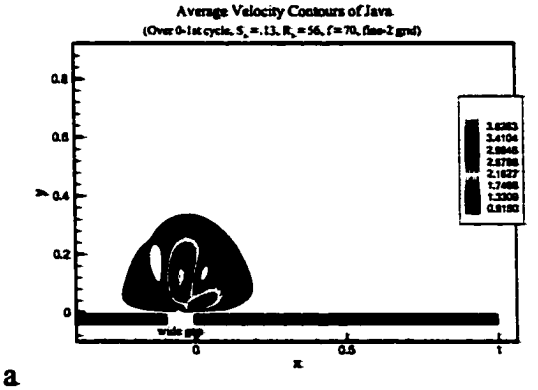

a

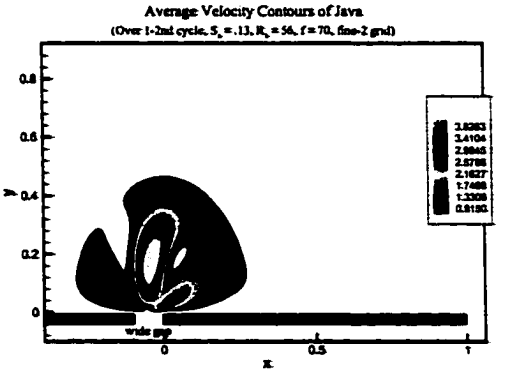

b

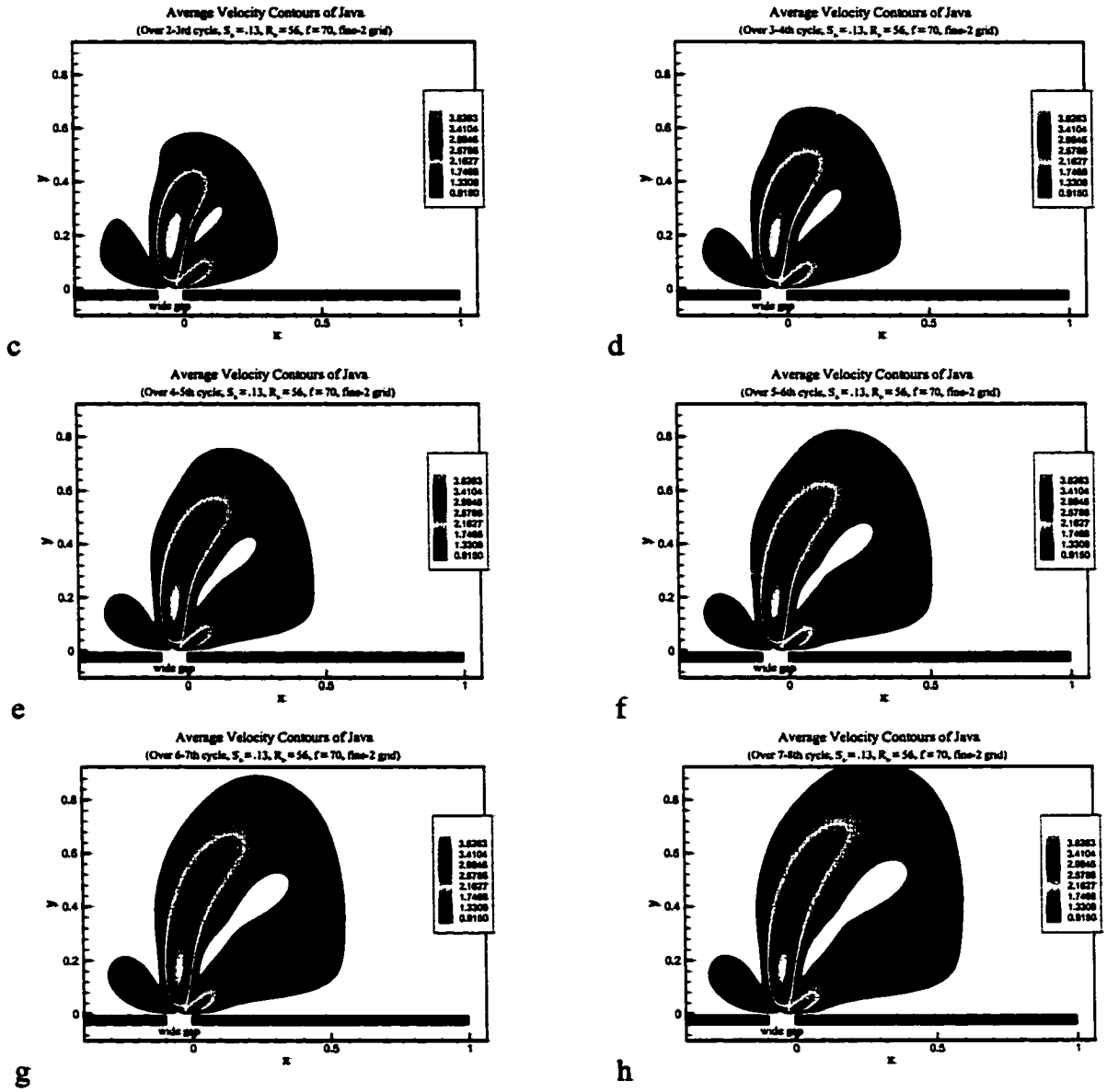

Figure 7.7 Computational simulations of JaVA flow field for jet flow.

7.3 Validation of Synthetic Jet Actuator

Recently, there have been massive experimental and computational investigations published on the synthetic jet actuators. The cases presented here are for validation purpose.

7.3.1 Computational Model

The model of the synthetic jet actuator consists of a cavity, a nozzle and an external region. In the computational simulation four blocks, as shown in Figure 7.8, are used. They are cavity (red block), nozzle (green block) and external zone (blue and cyan

blocks). The bottom of the cavity is capable of oscillating to generate synthetic jet. The grids are nondimensionalized by the width of jet nozzle, d, which is 0.5mm. The length of nozzle is equal to d. The nondimensional width and length of cavity are 15 and 10, respectively. The geometry parameters are obtained from Ref 105. The grid sizes are 301×151 (red block, cavity), 97×117 (green block, nozzle), 331×149 (blue block, external region 1) and 331×156 (cyan block, external region 2), respectively.

The reason of dividing the external region into two blocks is to keep loading balance in parallel computation. Then the four blocks can be run on four CPUs to save time.

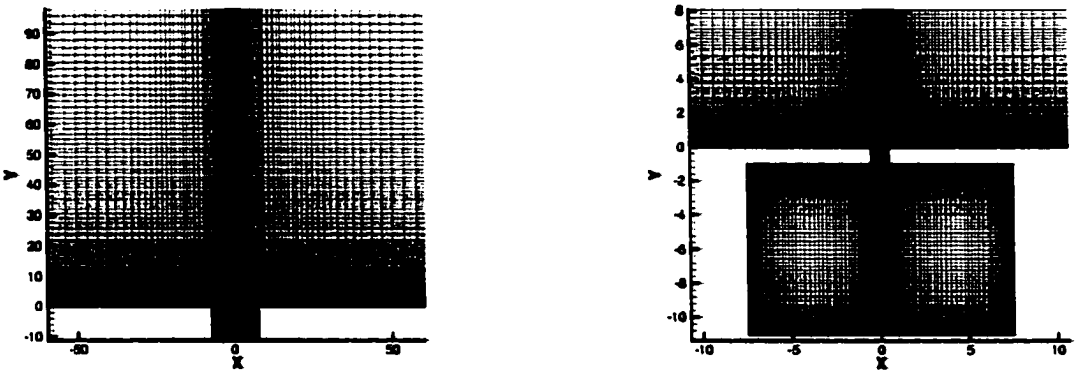

Figure 7.8 Multi-block grid used to simulate synthetic jet actuator.

7.3.2 Validation cases of Synthetic Jet Actuator

For this case, the conditions are set as the standard sea level atmospheric conditions. The reference velocity is 22m/s, which corresponds to M = 0.065. The oscillating frequency of cavity bottom is set as 1000Hz. These flow conditions are obtained from Ref 105.There are 8000 time steps for each oscillation period and the time step is set as 0.0055. In each time step, five sub-iterations are used. The computations are conducted on four Intel P4 2G cluster and they used about 1 second per time step.

Figures 7.9a – 7.9d show the instantaneous vorticity contours at t = 10T, 10.25T, 10.5T and 10.75T, where T is the oscillation period, respectively. The reduced frequency is ω, which is defined as $\omega = 2\pi/T$. Figure 7.9e shows the published computational results from Ref. 105. The comparison of time mean velocity at nozzle exit is shown in Figure

7.10. The instantaneous velocity at nozzle exit is shown in Figure 7.11. All of these results show good agreement with other published computational results.[105]

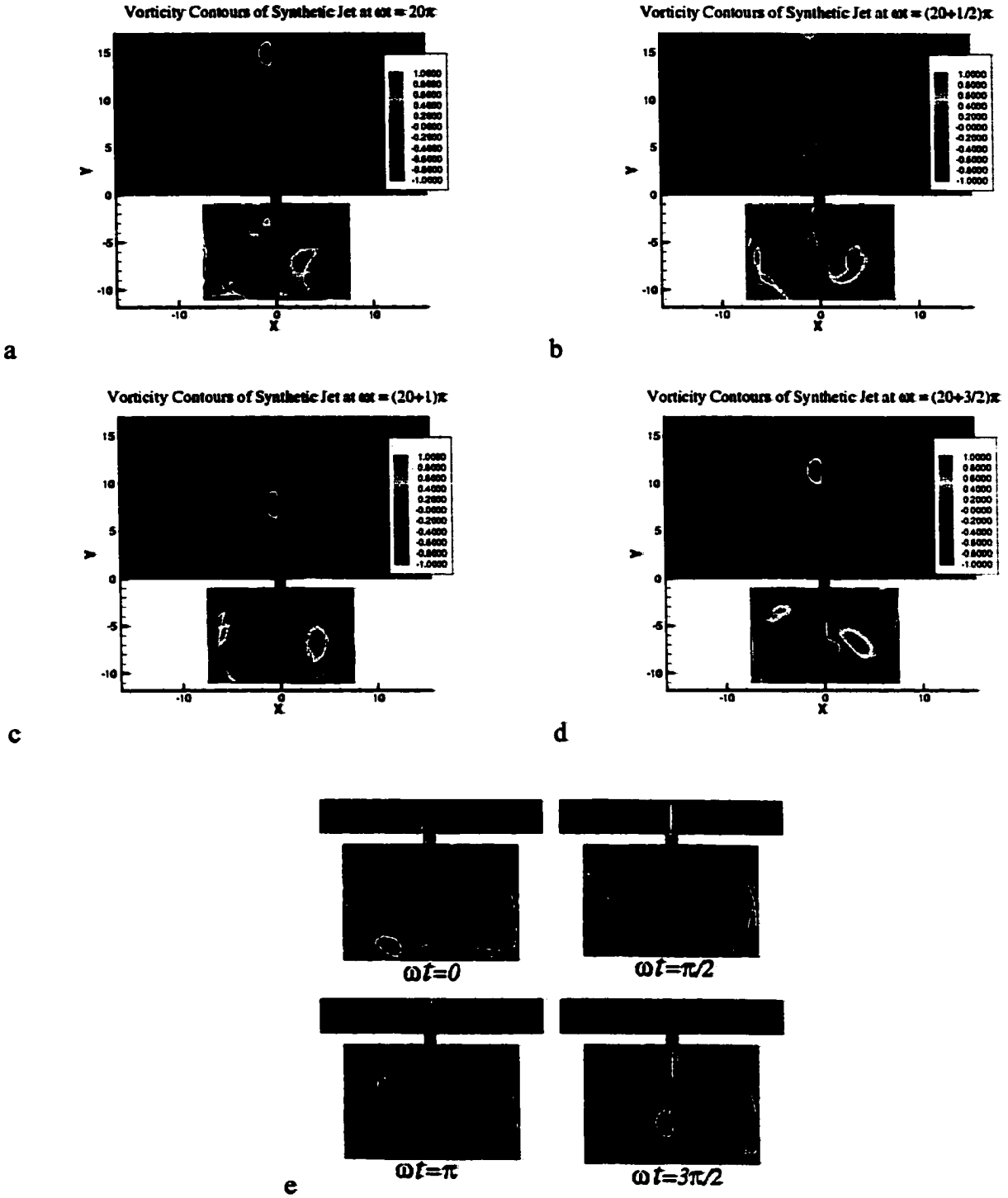

Figure 7.9 Instantaneous vorticity contour of synthetic jet flowfield. (a)-(d) Present PHCC. (e) Ref. 105.

be useful in buffet control. The potential application of oscillating exciting in buffet control was mentioned in Ref. 137. However, buffet alleviation was not shown in the computational case presented in Ref. 137, where the oscillating amplitude of C_p was decreased near trailing edge but increased near leading edge. The average oscillating amplitude of C_p over whole airfoil also was increased. So, the position, the oscillating frequency and amplitude of actuator should be investigated to achieve the optimal buffet control at different flow conditions because some combinations of excitation position, frequency and amplitude may not produce any good effect or may produce adverse effect on buffet control.

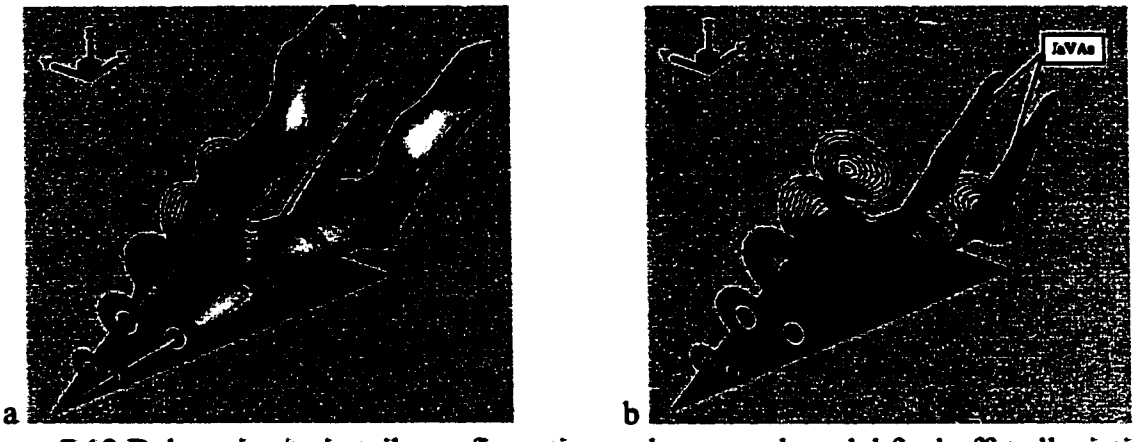

Figure 7.12 Delta-wing/twin tails configuration and proposed model for buffet alleviation by using actuators on twin-tails.

Figure 7.12a shows a delta-wing/twin-tail configuration at high angle of attack. Vortices generated from leading edge of delta-wing breakdown before they reach the twin tails. Highly turbulent wake would produce pressure fluctuation on the tails. Figure 7.12b shows a proposed buffet alleviation by using actuators on the surface of twin tails. Because of the limitation of computer resources, a simplified 2D model is investigated here. Figure 7.13a shows the flow field on the plane along the vortex core. Figure 7.13b shows the simplified 2D model of buffet alleviation by attaching actuator on airfoil. Numerical simulation is used in this research in order to investigate the best parameter, such as frequency and maximum velocity amplitude, for buffet control.

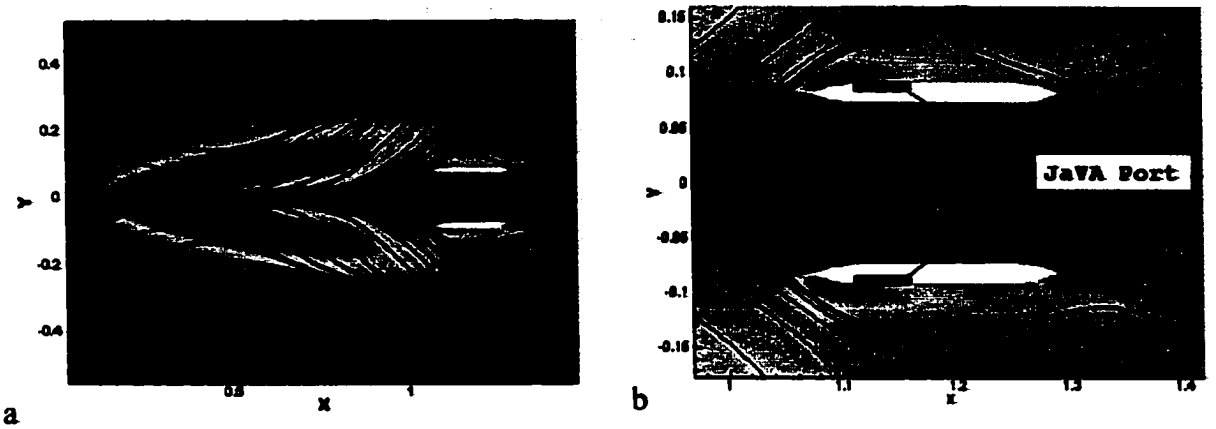

a b

Figure 7.13 Plane along vortex core (a) and the simplified 2D model of buffet alleviation by using actuators on airfoil (b).

The simplified 2D model consists of an airfoil and an actuator. The airfoil is a NACA0012 airfoil. The synthetic jet actuator is attached near 1% airfoil. The jet and vortex actuator is placed on the airfoil upper surface at 1.5% chord station. Figure 7.14 shows the grid used to simulate flow control by using a synthetic jet actuator. There are four grid blocks, which are 104×101(red, cavity), 63×45(green, nozzle), 378×63(blue, external region 1) and 378×64(black, external region 2). These four blocks are run using four CPUs separately. Figure 7.15 shows the grid used to simulate flow control by a jet and vortex actuator. There are three grid blocks, which are 95×51(red, cavity), 405×68(green, external region 1) and 405×69(blue, external region 2). These three blocks are run using three CPUs separately. The thickness of oscillating plate of the jet and vortex actuator is assumed to be zero in this computational application.

The external flow conditions are set as: Ma = 0.2, Re = 10^5, and the airfoil angle of attack is $\alpha = 15°$. At these conditions the flow will separate on upper airfoil surface near the leading edge. The pressure on the upper surface of airfoil will be highly unsteady and produce oscillating force on the airfoil. It needs to be noted that one important difference between the simplified 2D model and the twin-tail buffet is that the unsteady excitation in the simplified 2D model is generated by flow separation near upper surface of airfoil at a high angle of attack; while the pressure oscillation acting on the twin-tail is due to a highly turbulent wake that is generated by the vortex breakdown. However, if the flow around the airfoil or twin-tail is assumed to be a vibration system with numerous

springs, active control of such systems – exciting some frequencies or suppressing some frequencies – becomes similar. In this section the effects of different actuator parameters on the pressure response are investigated. All computations are obtained by using PHCC.

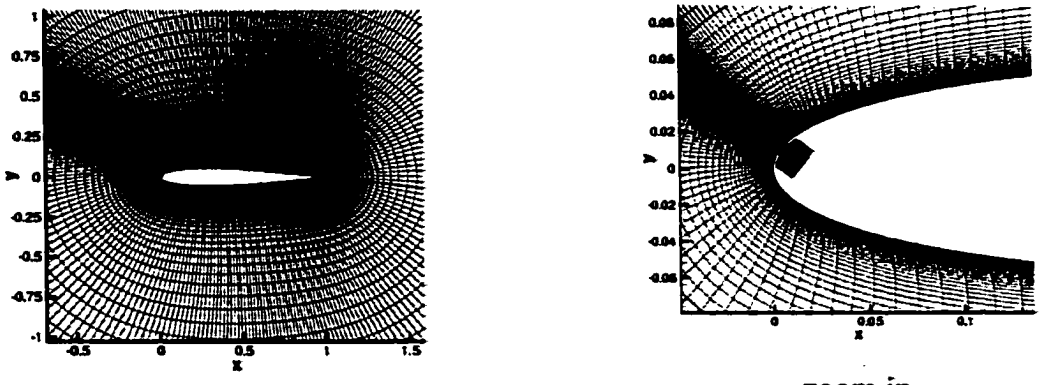

zoom in

Figure 7.14 Grid used for flow control using a synthetic jet actuator.

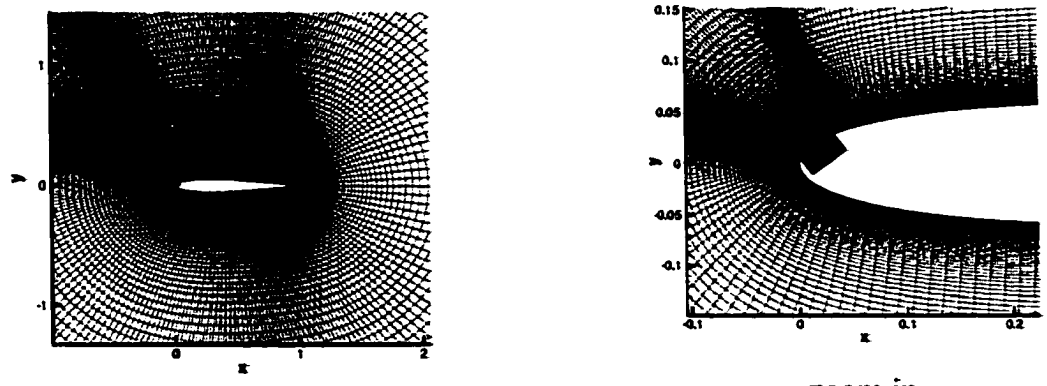

zoom in

Figure 7.15 Grid used for flow control using jet and vortex actuator.

In this study, two parameters (jet velocity and oscillating frequency) for synthetic jet actuator and three parameters (velocity and frequency of oscillating plate, and direction of JaVA) for JaVA are investigated. The table below shows the parametric study of active control by both actuators.

Table 7.1 Parameters for synthetic jet actuator

		exciting frequency f_e						
		0.1	0.2	0.5	1.	2.	4.	10.
V^*	0.05	Ja1	Ja2	***Ja3***	Ja4	***Ja5***	***Ja6***	***Ja7***
	0.1	Jb1	Jb2	Jb3	Jb4	Jb5	Jb6	Jb7
	0.2	Jc1	Jc2	***Jc3***	Jb4	***Jc5***	***Jc6***	***Jc7***

* V, maximum velocity at nozzle exit

Table 7.2 Parameters for jet and vortex actuator

		exciting frequency f_e						
		0.1	0.2	0.5	1.	2.	4.	10.
V_b^+	0.02	va1	va2	***va3***	va4	***va5***	***va6***	***va7***
		va1-	va2-	***va3-***	va4-	***va5-***	***va6-***	***va7-***
	0.035	vb1	vb2	vb3	vb4	vb5	vb6	vb7
		vb1-	vb2-	vb3-	vb4-	vb5-	vb6-	vb7-
	0.05	vc1	vc2	***vc3***	vc4	***vc5***	***vc6***	***vc7***
		vc1-	vc2-	***vc3-***	vc4-	***vc5-***	***vc6-***	***vc7-***

\+ V_b, maximum velocity of oscillating plate
\- Narrow slot close to leading edge

Because there are a lot of figures and some of them do not show appreciable control effect on the flow field, only the cases in ***Bold Italic*** are shown here.

Figures 7.16 – 7.39 show comparisons between the no-control case and control cases. These comparisons include the time history of pressure difference at 50% airfoil and power spectral density of pressure difference, the time history of normal force and power spectral density of normal force. The normal force is defined as the force normal to the mean plane of airfoil. The symbols of control case and corresponding parameters are listed in the table above.

Figures 7.16 – 7.23 show the results of using the synthetic jet actuator. The best control is achieved in control case Jc6 (Figure 7.22). The pressure difference PSD near low frequencies (1-3) are reduced more than 80%. Peak of pressure difference PSD is shifted to near a value of 4. The peak of normal force PSD is reduced by up to 40%. Low exciting velocity (control case Ja6, Figure 7.18) is not as good as high exciting velocity (control case Jc6). Very high exciting frequencies do worse job (control case Ja7, Figure 7.19 and control case Jc7, Figure 7.21). Low exciting frequencies do not have much effect (control case Ja3, Figure 7.16 and Jc3, Figure 7.20).

Figures 7.24 – 7.39 show the results of using the jet and vortex actuator. The best control achieved by JaVA is the control case vc5 (Figure 7.33) and vc5- (Figure 7.37). The peak of pressure difference PSD is shifted toward the exciting frequency. The normal force PSD is reduced more than 50% except at exciting frequency, compared to the no-control case. High exciting frequencies (vc7, vc7-) or low exciting frequencies (vc3, vc3-)

and low exciting velocity (va5, va5-) have little or worsening effect. The direction of JaVA has little effect on control.

Comparing the effectiveness of synthetic jet actuators and JaVA, JaVA achieves best control at a relatively low velocity (vc5 and vc5-), while the corresponding synthetic jet actuator (Ja6) does not produce good effect.

It is important to note that the exciting frequencies and velocities presented here are not optimal. The values of these parameters used here only show an approximate effect on the characteristics of flow field near airfoil. Based on the comparison of all the control cases, it can be concluded that actuators (synthetic jet, JaVA) can produce good effect on buffet control if they are operated at carefully selected frequencies, which are coupled with the flow system, and carefully selected velocities, which are big enough to change the pressure characteristics near the airfoil. It also needs to be noted that different flow problems have different flow properties. So the exciting frequencies should be adaptive adjusted to these different flow properties.

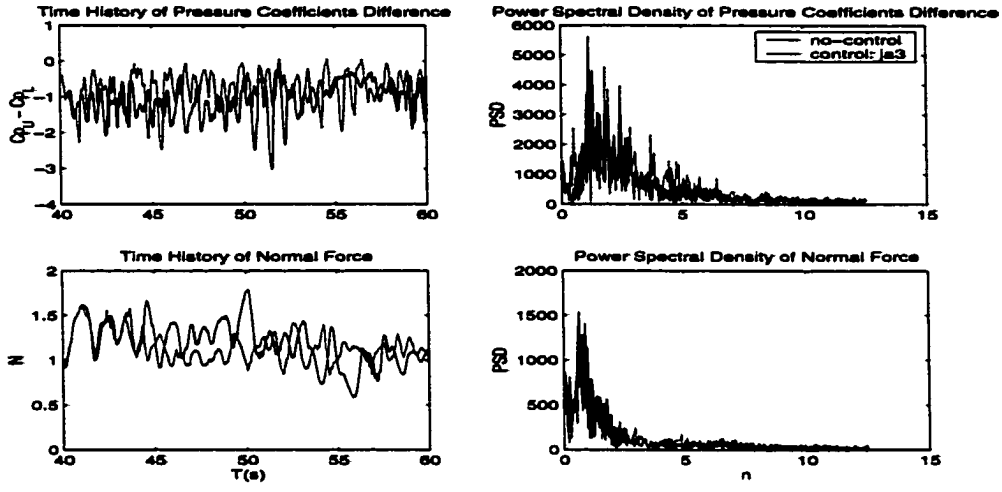

Figure 7.16 Comparison between no-control-case and control-Ja3.

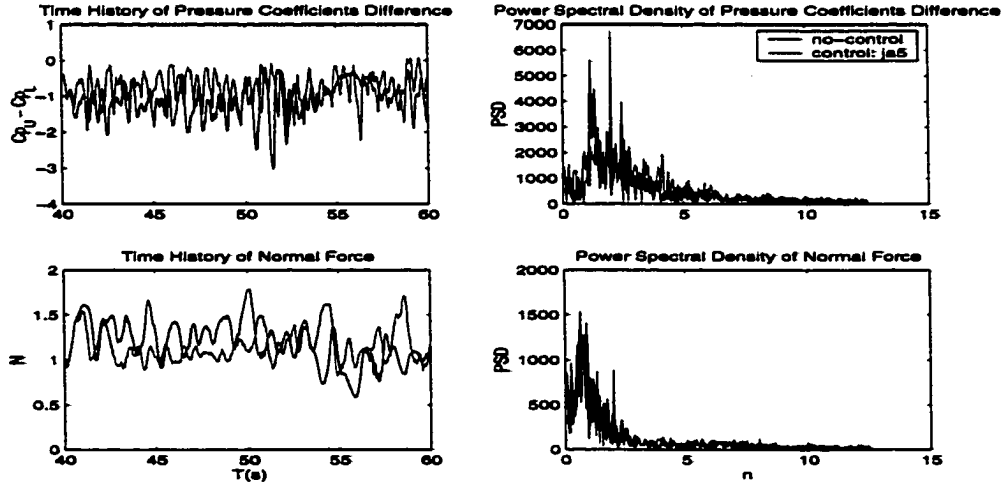

Figure 7.17 Comparison between no-control-case and control-Ja5.

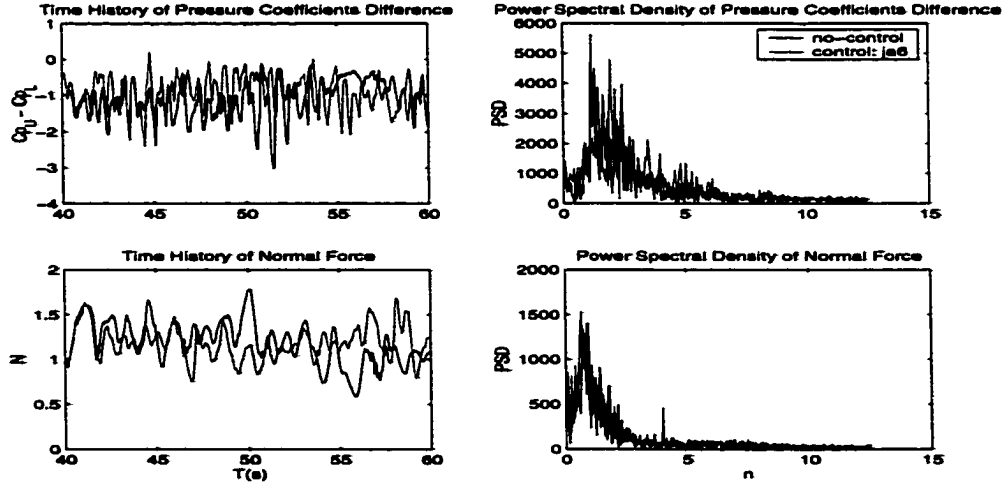

Figure 7.18 Comparison between no-control-case and control-Ja6.

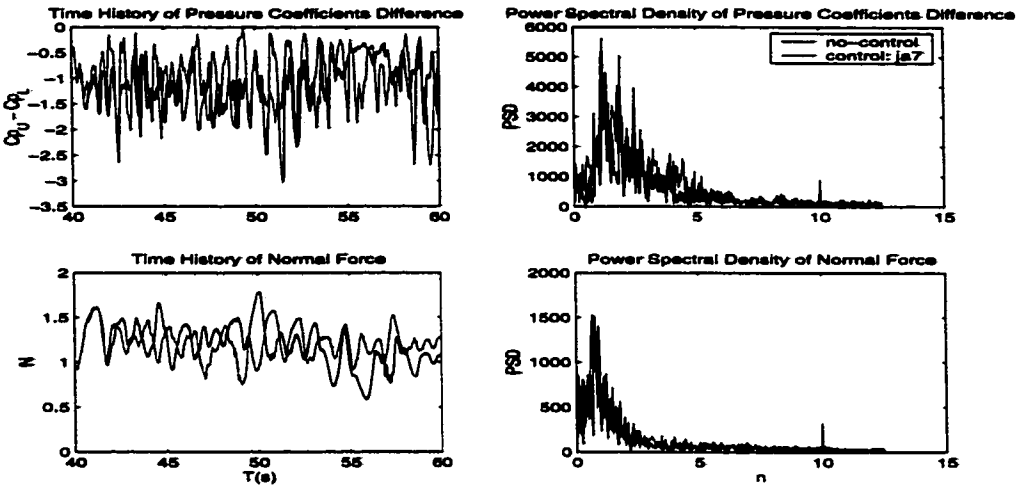

Figure 7.19 Comparison between no-control-case and control-Ja7.

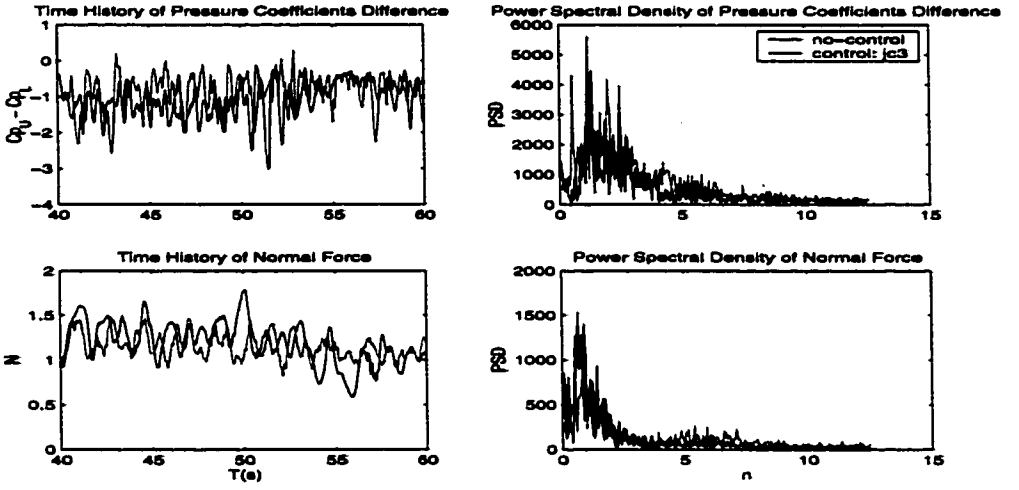

Figure 7.20 Comparison between no-control-case and control-Jc3.

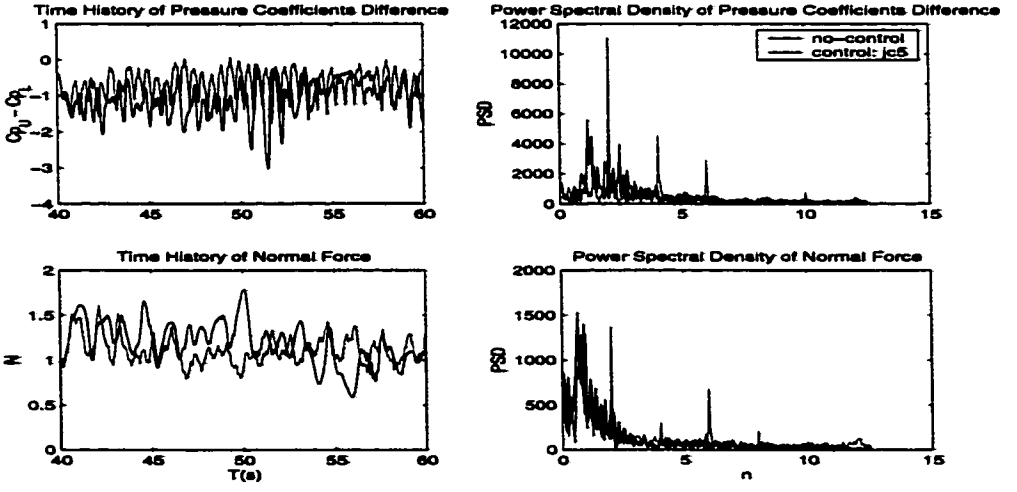

Figure 7.21 Comparison between no-control-case and control-Jc5.

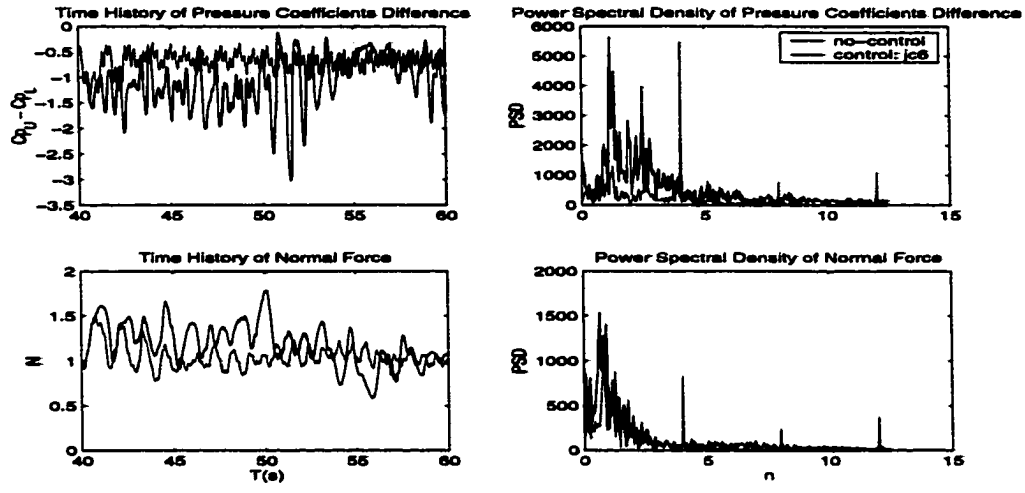

Figure 7.22 Comparison between no-control-case and control-Jc6.

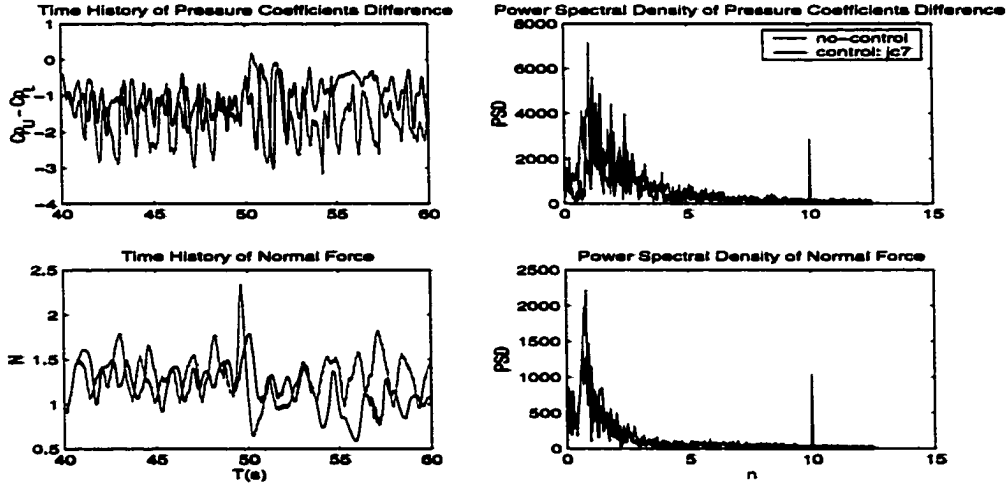

Figure 7.23 Comparison between no-control-case and control-Jc7.

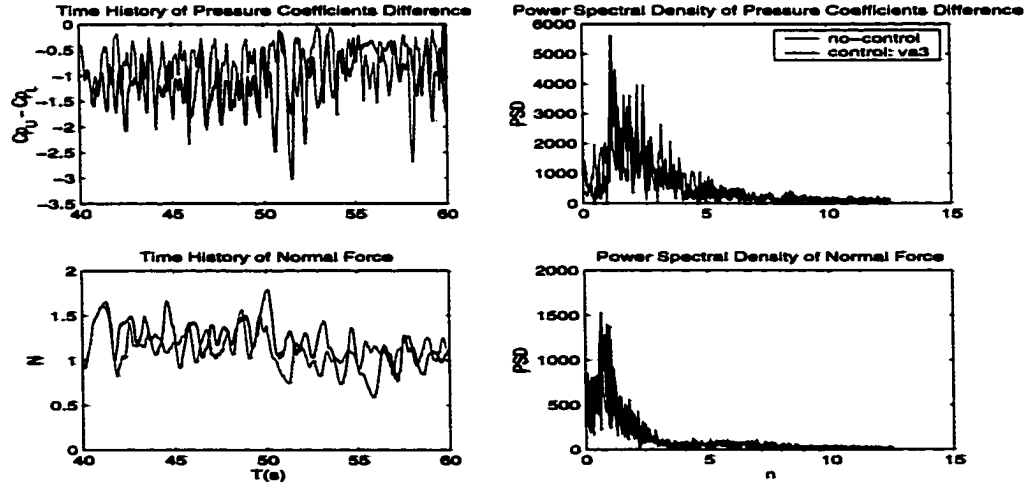

Figure 7.24 Comparison between no-control-case and control-va3.

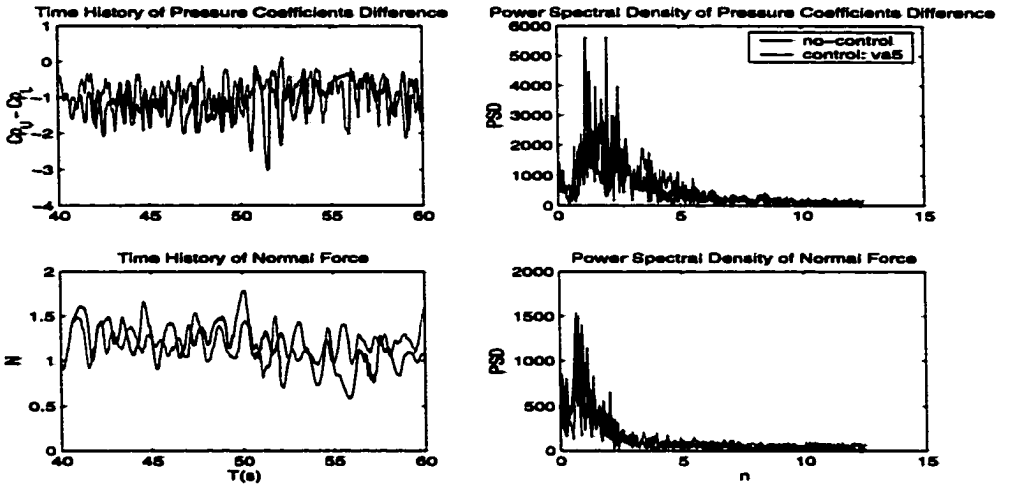

Figure 7.25 Comparison between no-control-case and control-va5.

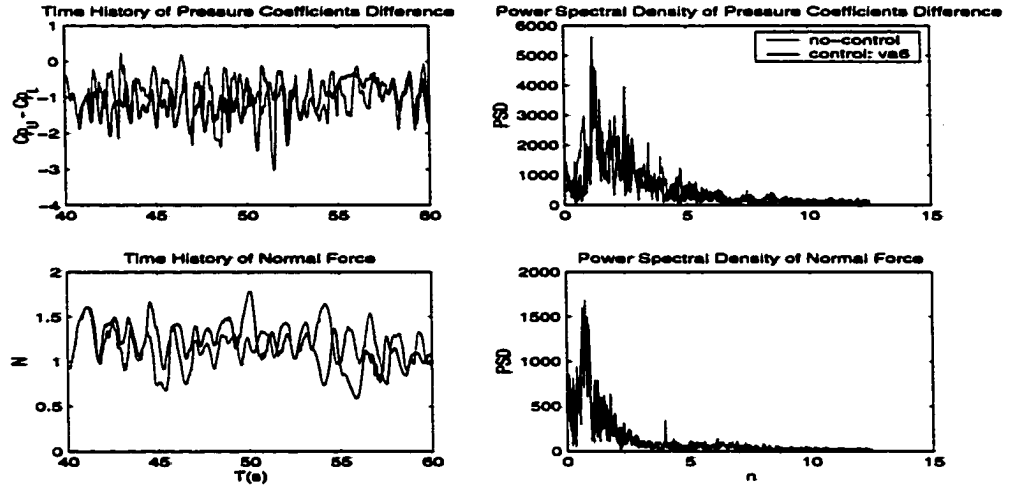

Figure 7.26 Comparison between no-control-case and control-va6.

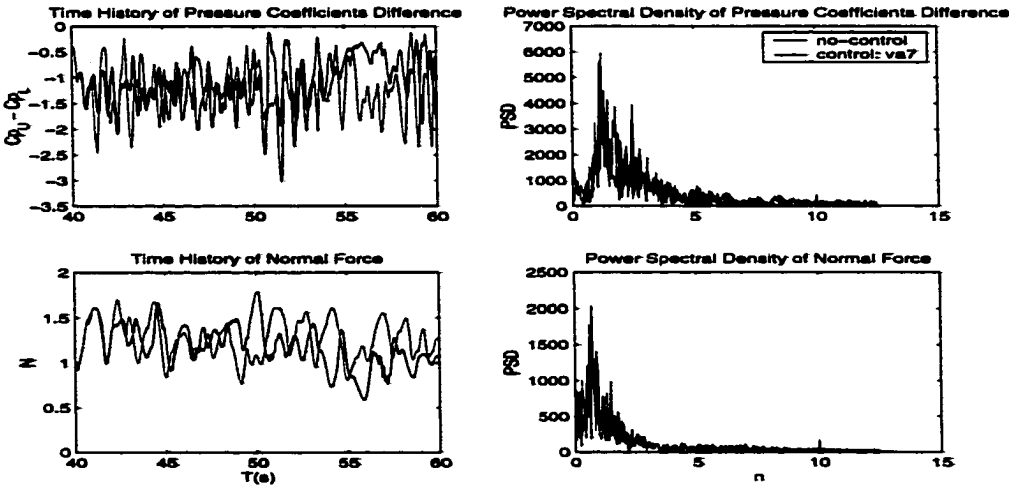

Figure 7.27 Comparison between no-control-case and control-va7.

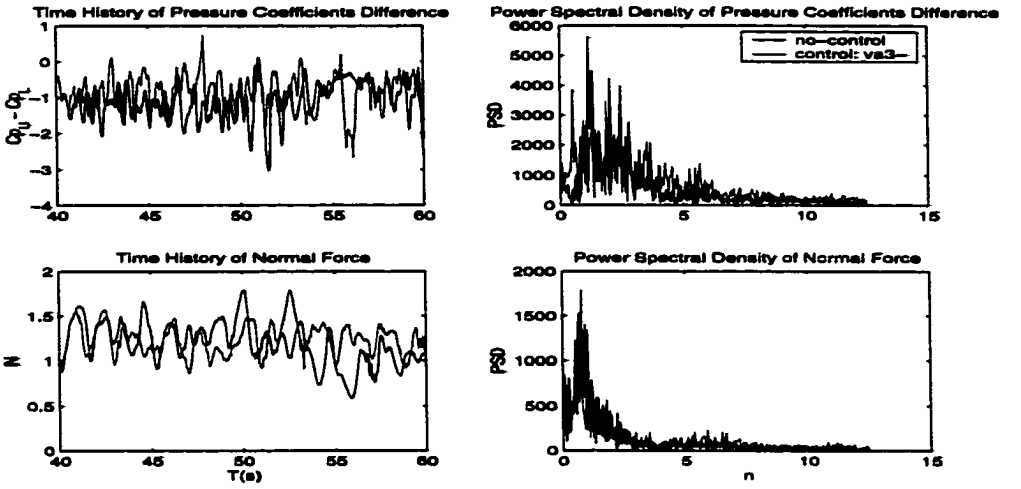

Figure 7.28 Comparison between no-control-case and control va3-.

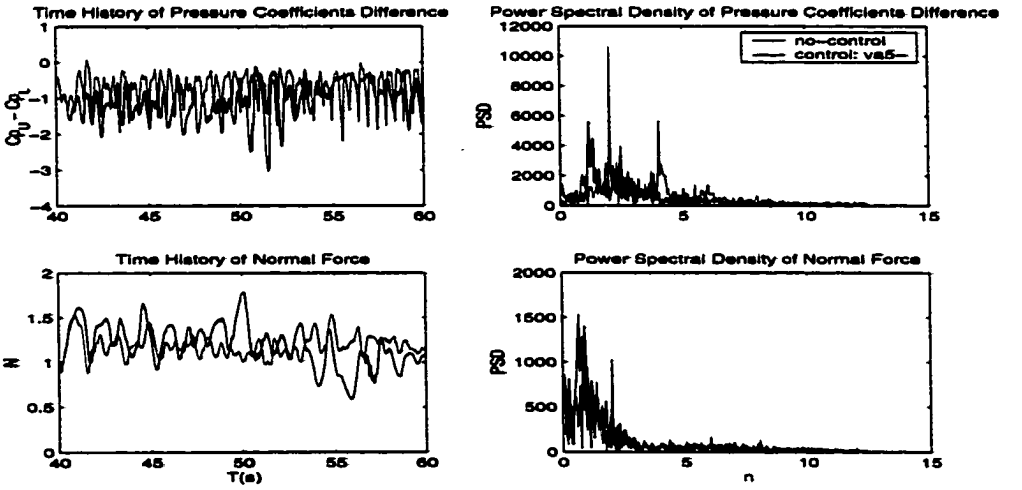

Figure 7.29 Comparison between no-control-case and control va5-.

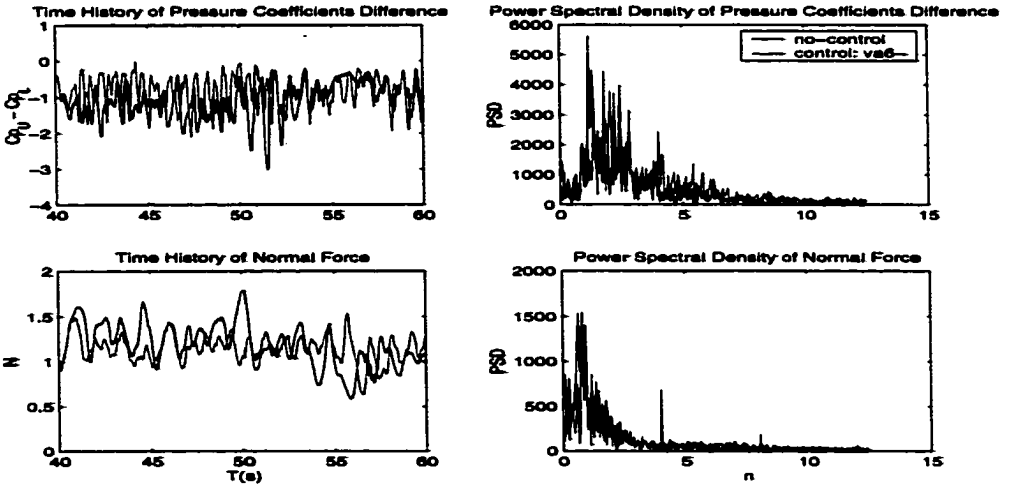

Figure 7.30 Comparison between no-control-case and control va6-.

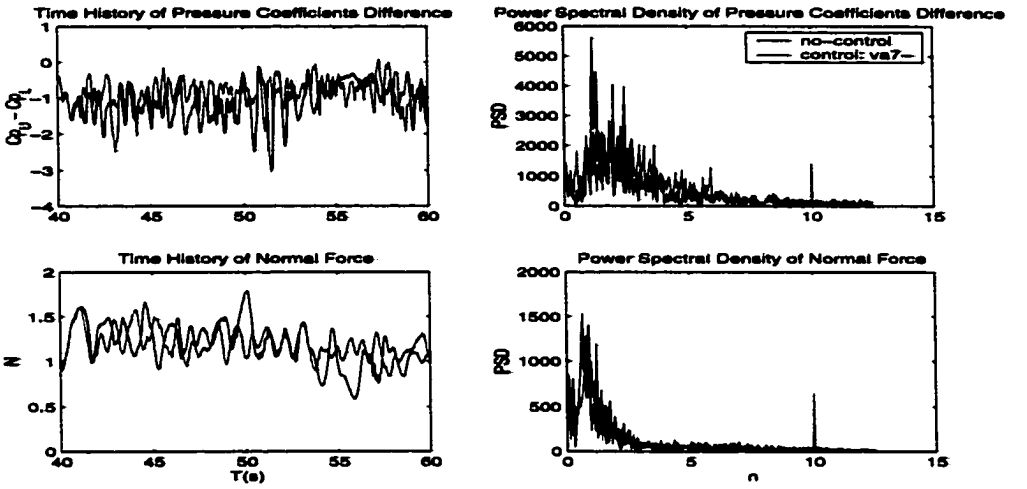

Figure 7.31 Comparison between no-control-case and control va7-.

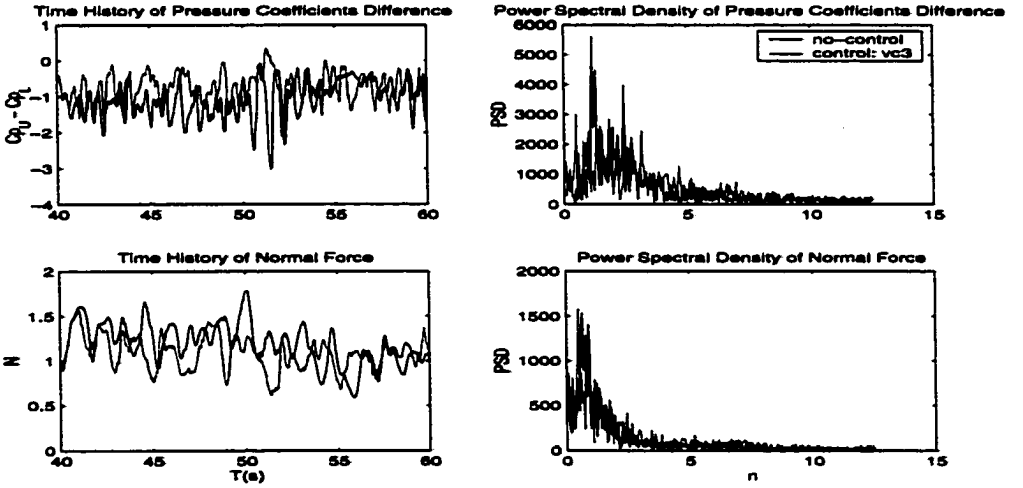

Figure 7.32 Comparison between no-control-case and control vc3.

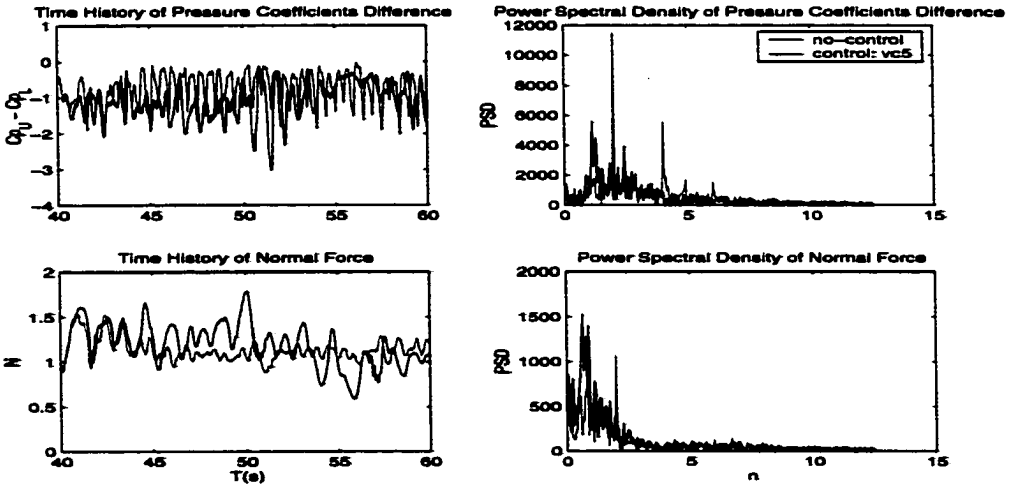

Figure 7.33 Comparison between no-control-case and control vc5.

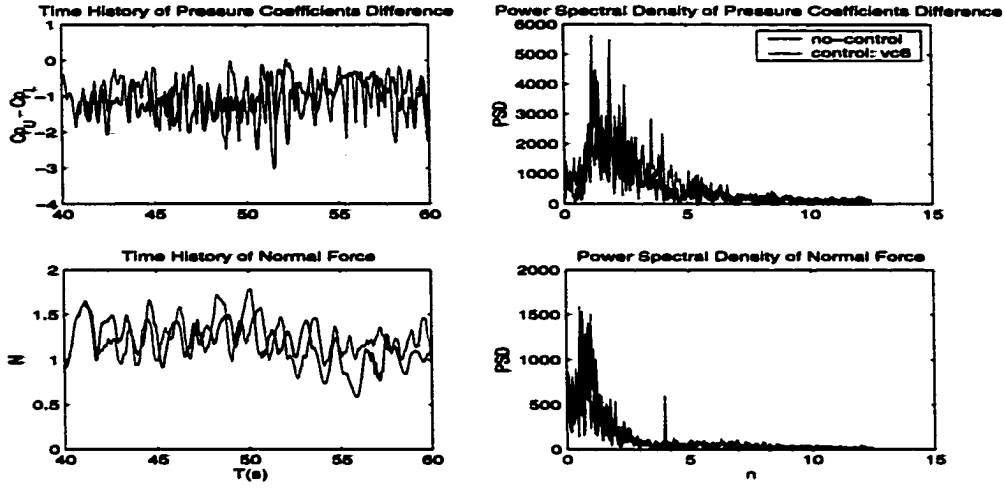

Figure 7.34 Comparison between no-control-case and control vc6.

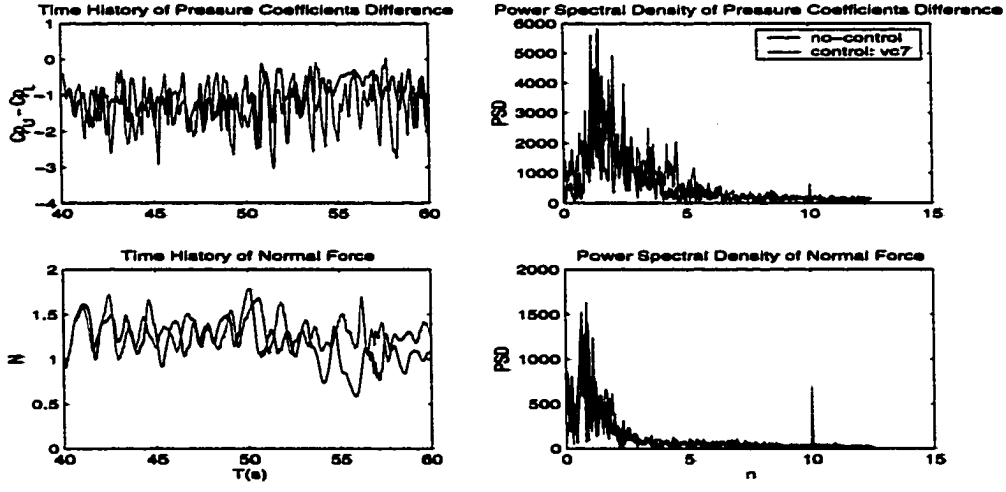

Figure 7.35 Comparison between no-control-case and control vc7.

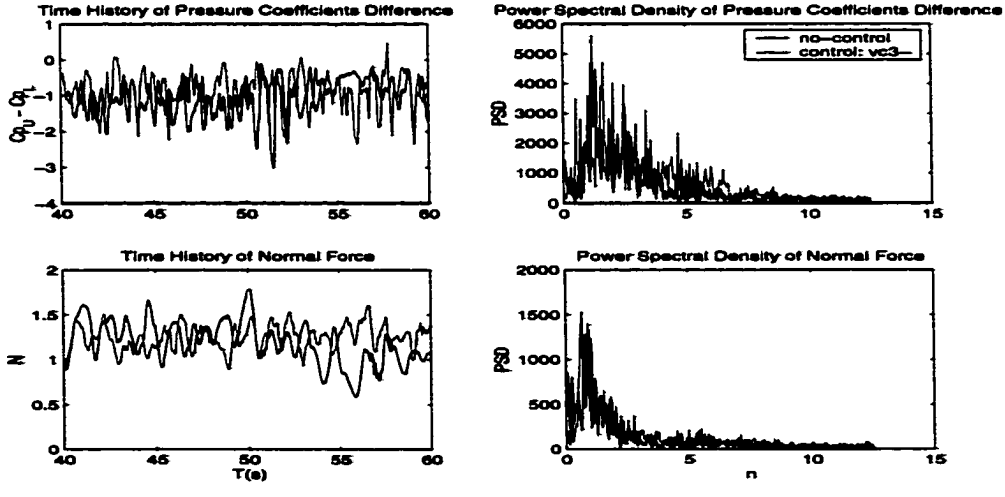

Figure 7.36 Comparison between no-control-case and control vc3-.

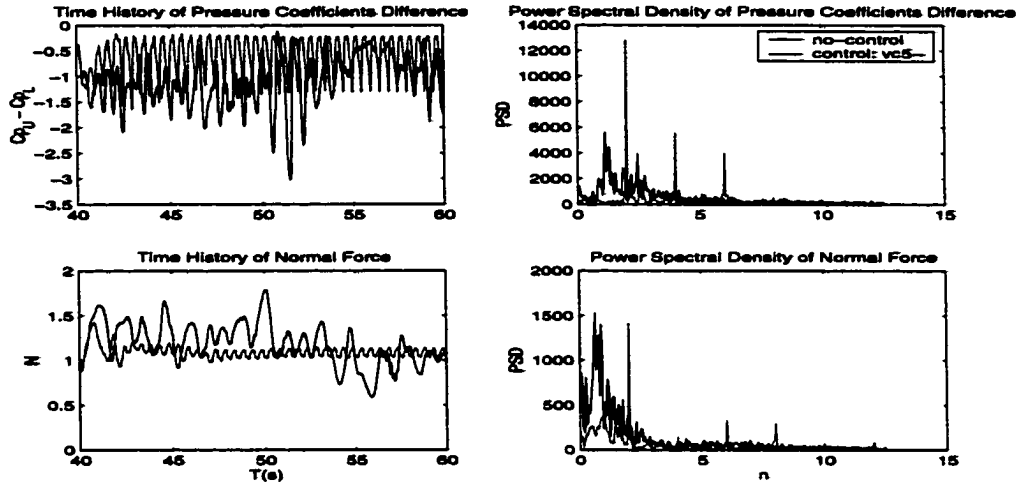

Figure 7.37 Comparison between no-control-case and control vc5-.

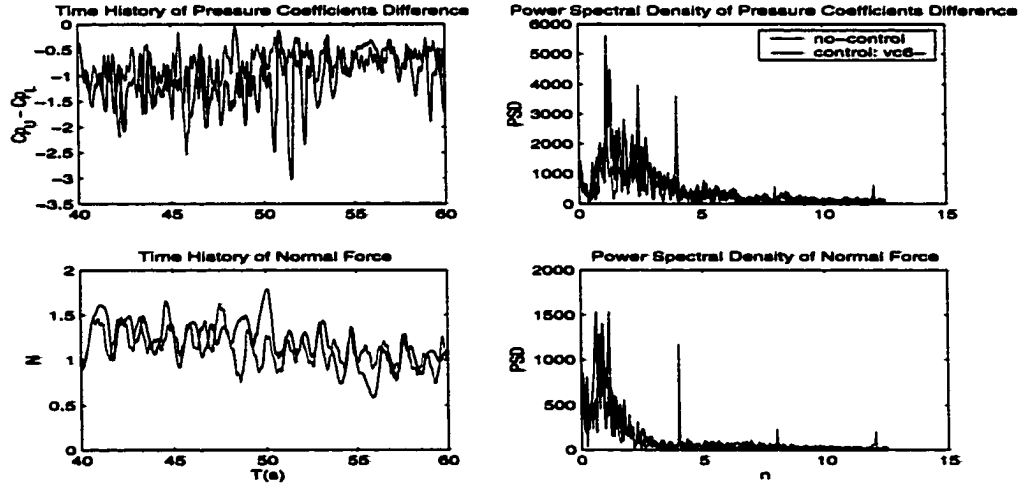

Figure 7.38 Comparison between no-control-case and control vc6-.

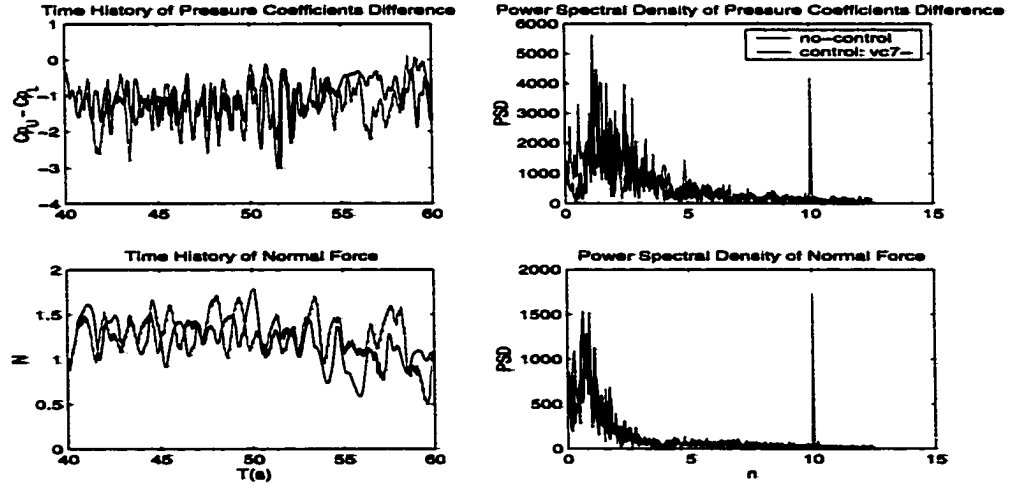

Figure 7.39 Comparison between no-control-case and control vc7-.

7.5 Summary

Jet and Vortex Actuators (JaVA) have been computationally investigated. A computational simulation model, which uses the full Navier-Stokes equations, has been developed and applied to the JaVA. Computational simulations duplicate two types of flow, vortex flow mode and free jet mode, and show good agreement with the experimental data. Computational simulations of synthetic jet actuator are conducted as validation cases.

The model of delta-wing/twin tails buffet alleviation by applying actuator on the surface of twin tails is simplified to a 2D model, which consists of an airfoil and an actuator (a synthetic jet actuator or a JaVA). Parametric investigation of the actuator has been conducted. With proper selection of the parameters values, the oscillating amplitude of the pressure difference and the normal force acting on the airfoil can be reduced, the peak of the normal force PSD can be reduced and the frequencies at which the peaks of the pressure difference PSD responses occurred can be shifted to higher frequency levels. Too low or too high exciting frequencies have either no control effect or adverse control effect. Low exciting velocity may not produce enough disturbances to suppress the pressure oscillation.

case, if the control ports are adjusted adaptively. Thus, this adaptive flow control method can benefit buffet control during aircraft maneuvering, when the angle of attack changes with time.

In Chapter 6, a high order compact scheme code (PHCC) has been developed for its advantages of computational accuracy and efficiency. Validations of the code are carried out for different flow cases. Compared with other computational simulation results and experimental data, the PHCC shows the expected high accuracy and efficiency.

In Chapter 7, Jet and Vortex Actuators (JaVA) have been computationally investigated and applied to an airfoil at a high angle of attack with unsteady separated flow. A computational simulation model has been developed and applied to the JaVA. The results of the computational simulations duplicate two types of flow – a vortex flow mode and a free jet mode, and show good agreement with the available experimental data. Computational simulations of synthetic jet actuator are also conducted and validated. The model of delta-wing/twin tails for buffet alleviation using actuators on the surface of twin tails is simplified to a 2D model, consisting of an airfoil at a high angle of attack and an actuator placed near the airfoil leading edge. Parametric investigations of the actuators are carried out. It has been shown that actuators (synthetic jet actuator or jet and vortex actuator) can reduce the oscillating amplitude of pressure difference acting on the airfoil and shift the frequencies at which the peaks of the PSD responses occurred. It also has been shown that with proper selection of the parameters, actuators can suppress the pressure level and variation near airfoil; hence, they will be beneficial for tail buffet alleviation.

8.2 Recommendations

The research work done in this dissertation has introduced the basics and foundations for continuing more targeted research work on the problem of twin tail buffet alleviation. Conducting computational simulation of 2D model with unsteady incoming flow, which originates from a typical breakdown vortex flow, should be the next step in order to assess the control effectiveness of the actuators. A parametric study which

includes optimal positions, exciting frequencies, phases and velocity for the actuators should be performed.

Once the control effectiveness is established for the 2D model, research work should be directed to the 3D model of the delta-wing/twin-tail configuration. Applying the actuators on the surface of twin-tails and investigating the optimal distributions, exciting frequencies, phases and velocity of the actuators should be the focus of this stage of the research work. However, considering the size of tail (~meter), the size of the actuators (~millimeter) and tens or hundreds of actuators attached on the surface of the tails, then tens of million grid points are needed and the 3D simulation is still a task that will require very extensive computational hardware and software resources. Parallel computation with a cluster of PC's with more than several hundred processors is envisioned to be the approach for handling the 3D type problems.

REFERENCES

1. "Active Flow Control — Bright Prospects and Basic Challenges," *Journal of Aircraft*, Vol. 38, No. 3, 2001, pp. 401.

2. Amitay, M., Smith, D., Kibens, V., Parekh, D., and Glezer, A., "Aerodynamic Flow Control of Bluff Bodies Using Synthetic Jet Actuators," In the proceedings of the IUTAM-Symposium "Mechanics of Passive and Active Flow Control," Gottingen, Germany, 7-11 September, 1998.

3. Amitay, M., Pitt, D., Kibens, V., Parekh, D. and Glezer, A., "Control of Internal Flow Separation using Synthetic Jet Actuators," AIAA 2000-0903, January 2000.

4. Barkley, D and Henderson, R. D., "Three-dimensional Floquet stability analysis of the wake of a circular cylinder," J. Fluid Mech. 322, 215, 1996.

5. Bean, D. E., Greenwell, D. I. And Wood, N. J., "Vortex Control Technique for the Attenuation of Fin Buffet," *Journal of Aircraft*, Vol. 30, No. 6, 1993, pp. 847-853.

6. Bean, D. E., and Wood, N. J., "An Experimental Investigation of Twin Fin Buffeting and Suppression," AIAA 03-0054.

7. Beaudan, P., Moin, P., "Numerical Experiments on the Flow Past a Circular Cylinder at Sub-Critical Reynolds Number," Stanford University, Departmnet of Mechanical Engineering Report No. TF-62, Stanford, CA, Dec. 1994.

8. Berger, E. and Wille, R., "Periodic flow phenomenon," Annu. Rev. Fluid Mech. 4, 313, 1972.

9. Bui, T. T., "A Parallel, Finite-Volumn Algorithm for Large-Eddy Simulation of Turbulent Flows," NASA/TM-1999-206570.

10. Cain, A. B., Kral, L. D., Donovan, J. F. and Smith, T. D., "Numerical Simulation of Compressible Synthetic Jet Flows," AIAA 98-0084, January 1998.

11. Chatlynne, E., Rumigny, N., Amitay, M., and Glezer, A., "Virtual Aero-Shaping of a Clark-Y Airfoil Using Synthetic Jet Actuators," AIAA 2001-0732, Janaury 2001.

12. Chen, Y., Liang, S., Aung, K., Glezer, A., and Jagoda, J., "Enhanced Mixing in a Simulated Combustor Using Synthetic Jet Actuators," AIAA 99-0449.

13. Craig, K, "Computational Study of Blowing on Delta Wings at High Alpha," AIAA paper 92-0410, also *Journal of Aircraft*, Vol. 30, No.6, 1993, pp. 833-839.

14. Délery, J. M., "Physics of Vortical Flows," Journal of Aircraft, Vol. 29, No.5, 1992, pp. 856-876

15. Duncan, W. J., Ellis, D. L. and Scruton, C., "Fist Report on the General Investigation of Tail Buffeting," Aeronaut. Research Com. R. & M., 1457, part I, 1932, 1541, part II, 1933.

16. Edwards, J. W., "Assessment of Computational Prediction of Tail Buffeting," NASA TM 101613, Jan. 1990.

17. Ekaterinaris, J. and Schiff, L. B., "Numerical Simulation of Incidence and Sweep Effects on Delta Wing Vortex Breakdown," *Journal of Aircraft*, Vol. 31, No.5, 1994, pp. 1043-1049.

18. Elle, B. J., "An Investigation at Low Speed of the Flow Near the Apex of Thin Delta Wings with Sharp Leading Edges," ARC 19780-perf. 1621-f.m. 2629, Aeronautical Research Council, January 1958.

19. Elle, B. J., "On the Breakdown at High Incidences of the Leading Edge Vortices on Delta Wings," *Journal of the Royal Aeronautical Society*, Vol. 64, August 1960, pp.491-493.

20. Erickson, G. E., "Water-Tunnel Studies of Leading Edge Vortices," *Journal of Aircraft*, Vol. 19, No. 6, June 1982, pp.

21. Escudier, M., "Vortex Breakdown: Observations and Explanations," *Progress in Aerospace Sciences*, Vol. 25, No. 2, 1988, pp. 189-229.

22. Flynn, G. A., Morrison, J. F., and Mabey, D. G., "Buffet Alleviation on an Unswept Wing at High Incidnece," AIAA 99-0791.

23. Fung, Y. C., "An Introduction to the Theory of Aeroelasticity," Dover Publications, 1969.

24. Gartshore, I., "Recent Work in Swirling Incompressible Flow," Report LR-343, N.R.C. No. 6968, National Research Council of Canada, 1962.

25. Gee, K., Murmann, S. M., and Schiff, L. B., "Computation of F/A-18 Tail Buffet," AIAA Paper 95-3440, AIAA Atmospheric Flight Mechanics Conference, Baltimore, MD, August 1995. Also *Journal of Aircraft*, Vol. 33, No. 6, 1996, pp. 1181-1189.

26. Germano M., Ugo Piomelli, Moin P., and William H. Cabot, "A Dynamic Subgrid-Scale Eddy Viscosity Model," *Physics of Fluids*, Vol. 3, July 1991, pp. 1760-1765.

27. Glezer, A. and Amitay, M., "Synthetic Jets," Annu. Rev. Fluid Mech. 2002. vol.34 pp.503-529.

28. Gordnier, R. E. and Visbal, M. R., "Numerical Simulation of the Unsteady Vortex Structure Over a Delta Wing," AIAA 91-1811-CP, 1991.

29. Görtz, S. and Rizzi, A., "Computational Study of Vortex Breakdown over Swept Delta Wings," AIAA 99-3118.

30. Gursul, I., "Unsteady Flow Phenomena over Delta Wings at High Angle of attack," AIAA Journal, Vol. 32, No. 2, 1994, pp. 225-231.

31. Guy, Y., Morrow, J. A., and McLaughlin, T. E., "Control of Vortex Breakdown on a Delta Wing by Periodic Blowing and Suction," AIAA 99-0132, January 1999.

32. Hauch, R. M. , Jacobs, J. H. and Dima, C., "Reduction of Vertical Tail Buffet Response Using Active Control," AIAA paper 95-1080, AIAA 36th Structures, Structural Dynamics, and Materials Conference, New Orleans, LA, April, 1995. Also Jounal of Aircraft, Vol. 33, No. 3, 1996, pp. 617-622.

33. Hall, M. G., "A Numerical Method for Solving the Equations for A Vortex Core," ARC 27150, Reports and Memoranda, No. 3467, A.R.C., 1965.

34. Hassan, A. A., JanakiRam, R. D., "Effects of Zero-Mass Synthetic Jets on the Aerodynamics of the NACA-0012 Airfoil," AIAA 97-2326.

35. Hassan, A. A., "Numerical Simulations and Potential Applications of Zero-Mass Jets for Enhanced Rotorcraft Aerodynamic Performace," AIAA paper 98-0211, January, 1998.

36. Henderson, R. D., "Details of the drag curve near the onset of vortex shedding," *Phys. Fluids*, 7 (9), Sept. 1995.

37. Hummel, D., "On the Vortex Formation over A Slender Wing at Large Angles of Incidence," AGARD-CP-247, October 1978.

38. Jacobson, S. A., and Reynolds, W. C., "Active boundary layer control using flush-mounted surface actuators," *Bulletin of the American Physical Society*, Vol. 96, 1993, pp. 2197.

39. Jacobson, S. A., and Reynolds, W. C., "Active control of Streamwise Vortices and Streaks in Boundary Layers," *Journal of Fluid Mechanics*, Vol. 360, 1998, pp. 179-211.

40. Joslin, R. D., Lachowicz, J. T. and Yao, C. S., "DNS of Flow Induced by A Multi-Flow Actuator," FEDSM 98-5302, 1998 ASME Fluids Engineering Division Summer Meeting, June 1998.

41. Kandil, H. A., "Navier-Stokes Simulation of Quasi-Axisymmetric and Three Dimensional Supersonic Vortex Breakdown," Ph.D. Dissertation, Department of Mecahnical Engineering and Mechanics, Old Dominion University, May 1993.

42. Kandil, O. A., Kandil, H. A. and Liu, C. H., "Computation of Steady and Unsteady Compressible Quasi-Axisymmetric Vortex Flow and Breakdown," AIAA 91-0752, January 1991.

43. Kandil, O. A., Kandil, H. A., "Computation of compressible quasi-axisymmetric slender vortex flow and breakdown," *Computer Physics Communications*, Vol. 65, 1991, pp. 164-172.

44. Kandil, O. A., Kandil, H. A. and Liu, C. H., "Supersonic Quasi-Axisymmetric Vortex Breakdown," AIAA 91-3311-CP, September 1991.

45. Kandil, O. A., Kandil, H. A. and Liu, C. H., "Critical Effects of Downstream Boundary Conditions on Vortex Breakdown," AIAA 92-2601-CP, June 1992.

46. Kandil, O. A., Kandil, H. A. and Liu, C. H., "Shock/Vortex Interaction and Vortex Breakdown Modes," IUTAM Symposium of Fluid Dynamics of High Angle of Attack, No. T.1.3. Tokyo, Japan, September 1992.

47. Kandil, O. A., Kandil, H. A. and Liu, C. H., "Shock-Vortex Interaction Over a 65-degree Delta Wing in Transonic Flow," AIAA 93-2973, July 1993.

48. Kandil, O. A., and Flanagan, M. W., "Vertical Tail Buffet in Vortex Breakdown Flows," 5th International Symposium on Computational Fluid Dynamics, Sendai Japan, August 1993.

49. Kandil, O. A., Kandil, H. A. and Liu, C. H., "Supersonic Vortex Breakdown Over a 65-degree Delta Wing in Transonic Flow," AIAA 93-3472, August 1993.

50. Kandil, O. A., Kandil, H. A. and Massey, S. J., "Simulation of Tail Buffet Using Delta Wing-Vertical Tail Configuration," AIAA 93-3688-CP, AIAA Atmospheric Flight Mechanics Conference, Monterery CA, August 1993, pp. 566-577.

51. Kandil, O. A., Massey, S. J. and Kandil, H. A., "Computations of Vortex Breakdown Included Tail Buffet Undergoing Bending and Torsional Vibrations," AIAA 94-1428-CP, AIAA/ASME/ASCE/ASC Structural, Structural Dynamics and Material Conference, SC April 1994, pp. 977-993.

52. Kandil, O. A., Massey, S. J. and Sheta, E. F., "Structural Dynamics/CFD Interaction for Computation of Vertical Tail Buffet," International Forum on Aeroelasticity and Structural Dynamics, Royal Aeronautical Society, June 1995, pp. 52.1-52.4. Also in *Royal Aeronautical Journal*, August-September 1996, pp. 297-303.

53. Kandil, O. A., Massey, S. J. and Sheta, E. F., "Aerostructural Vortical Flow Interactions With Applications to F/A-18 and F-117 Tail Buffet," NASA CR-203245, High-Angle-of-Attack Technology Conference, NASA Langley Research Center, Hampton, VA, September 1996.

54. Kandil, O. A., Menzies, M. A., "Effective Control of Computationally Simulated Wing Rock in Subsonic Flow," AIAA 97-0831, January 1997.

55. Kandil, O. A., Sharaf El-Din, H. H., and Liu, C. H., "Active Control of Asymmetric Vortical Flows around Cones Using Injection and Heating," AIAA 91-, 1992.

56. Kandil, O. A., Sharaf El-Din, H. H., and Liu, C. H., "Three Dimensional Solution of Pneumatic Active Control of Forebody Vortex Asymmetry," AIAA 95-0101, January 1995.

57. Kandil, O. A., Sheta, E. F., "Coupled and Uncoupled Bending-Torsion Responses of Twin-Tail Buffet," AD-Vol. 53-3, 4th International Symposium on Fluid Structure Interactions, Aeroelasticity, Flow-Induced Vibration & Noise, 1997 ASME Int'l Mech. Eng'g Congress & Exposition, November 1997.

58. Kandil, O. A., Sheta, E. F., Liu, C. H., "Effects of Coupled and Uncoupled Bending-Torsion Modes on Twin-Tail Buffet Response," IUTAM-Symposium on Dynamics of Slender Vortices, Aachen, Germany, August 1997.

59. Kandil, O. A., Sheta, E. F., and Massey, S. J., "Buffet Responses of a Vetical Tail in Vortex Breakdown Flows," AIAA 95-3464-CP, AIAA Atmospheric Flight Mechanics Conference, August 1995, pp. 345-360.

60. Kandil, O. A., Sheta, E. F., and Massey, S. J., "Twin Tail/Delta Wing Configuration Buffet Due to Unsteady Vortex Breakdown Flow," AIAA 96-2517-CP, 14th AIAA Applied Aerodynamics Conference, June 1996, pp. 1136-1150.

61. Kandil, O. A., Sheta, E. F., and Massey, S. J., "Fluid/Structure Twin Tail Buffet Response Over A Wide Range of Angles of Attack," AIAA 97-2261-CP, 15th AIAA Applied Aerodynamics Conference, June 1997.

62. Kandil, O. A., Yang, Z., and Sheta, E. F., "Flow Control and Modification for Alleviating Twin-Tail Buffet," AIAA 99-0138, Reno, NV, January 1999.

63. Kandil, O. A., Yang, Z., "Adaptive Suction and Blowing Flow Control Effectiveness for Twin-Tail Buffet Control," AIAA 99-3126, 17th AIAA APA Conference, Norfolk, VA, June 1999.

64. Kandil, O. A., Yang, Z., and You, R, "Effectiveness of Adaptive Flow Control for Twin-Tail Buffet," AIAA 2000-4414, AIAA Applied Aerodynamic Conference, Denver, CO, August 2000.

65. Kandil, O. A., Yang, Z., and Lachowicz, J.T., "Computational and Physical Analysis of Active Vortex Generators," IEEE 2000-0483, IEEE Aeropace Conference 2000, March 2000.

66. Klute, S. M., Martin, R. A., Rediniotis, O. K., and Telionis, D. P., "Flow Control Over Delta Wings at High Angle of Attack," AIAA CP 93-3494, 1993.

67. Koumoutsakos, P., "Simulations of vortex generators," *Center for Turbulence Research, Annual Research Briefs*, 1995, pp. 233-240.

68. Kral, L. D., Donovan, J. F., Cain, A. B. and Cary, A. W., "Numerical Simulation of Synthetic Jet Actuators," AIAA 97-1824, June-July 1997.

69. Krause, E., Shi, X. G. and Hartwich, P. M., "Computation of Leading Edge Vortices," AIAA paper 83-1907, 1983.

70. Kravchenko, A. G. and Moin, P. and Shariff, K., "B-Spline Method and Zonal Grids for Simulations of Complex Turbulent Flows," *Journal of Computational Physics*, 151, pp. 757-789, 1999.

71. Kravchenko, A. G. and Moin, P., "Numerical studies of flow over a circular cylinder at $Re_D = 3900$," Physics of Fluids, Vo. 12, No. 2, 2000.

72. Lachowicz, J. T., Yao, C. S. and Wlezien, R. W., "Scaling of an Oscillatory Flow Control Actuator," AIAA 98-0330, January 1998.

73. Lambourne, N. and Bryer, D., "The Bursting of Leading-Edge Vortices: Some Observations and Discussion of the Phenomenon," R. and M. No. 3282, Aerodynamics Division, National Physical Laboratory, London, England, April, 1961.

74. Lee, B. H. K. and Brown, D., "Wind-Tunnel Studies of F/A-18 Tail Buffet," AIAA paper 90-1432, June 1990, also *Journal of Aircraft*, Vol.29, No.1, 1992, pp.146-152.

75. Lee, B. H. K. and Tang, F. C., "Characteristics of the Surface Pressures on a F/A-18 Vertical Fin Due to Buffet," *Journal of Aircraft*, Vol. 31, No. 1, 1994, pp. 228-235.

76. Lee, B. H. K. and Valerio, N. R., "Vortical Flow Structure near the F/A-18 LEX at High Incidence," *Journal of Aircraft*, Vol. 31, No. 5, 1994, pp. 1221-1223.

77. Lee, C. Y. and Goldstein, D. B., "Two-Dimensional Synthetic Jet Simulation," AIAA 2000-0406, January 2000.

78. Lele, S. K., "Compact Finite Difference Scheme with Spectral-like Resolution," *Journal of Computational Physics*, Vol. 103, 1992, pp. 16-42.

79. Liepmann, H. W., "On the Application of Statistical Concepts to the Buffeting Problem," *J. Aeronaut.Sci.* v.19, 1952, pp.793-800.

80. Lachowicz, J. T., Yao, C. S., and Wlezien, R. W., "Scaling of an Oscillatory Flow-Control Actuator," AIAA 98-0330, 36th Aerospace Sciences Meeting and Exhibit, January 1998.

81. Lachowicz, J. T., Yao, C. S., Joslin, R. D., "Physical Analysis and Scaling of a Jet and Vortex Actuator," FEDSM99-6921, 3rd ASME/JSME Joint Fluids Engineering Conference, July 1999.

82. Massey, S. J., "Dvelopment of A Coupled Fluid/Structure Aeroelastic Solver with Applications to Vortex Breakdown Included Twin Tail Buffet," Ph.D. dissertation, Department of Aerospace Engineering, Old Dominion University, 1997.

83. Massey, S. J., and Kandil, O. A., "Effect of Apex Flap Deflection on Vertical Tail Buffeting," AIAA 98-0762, January 1998.

84. Mathew, J., Sankar B. and Cattafesta L., "Finite Element Modeling of Piezoelectric Actuators for Active Flow Control Applications," AIAA paper 2001-0300, 39the Aerospace Sciences Meeting & Exhibit, Reno, NV, January 2001.

85. Meyn, L. A. and James, K. D., "Full-Scale Wind-Tunnel Studies of F/A-18 Tail Buffet," AIAA paper 93-3519, August 1993, also *Journal of Aircraft*, Vol.33, No.3, 1996, pp.589-595.

86. Michalke, A., "On the Inviscid Instability of the Hyperbolic-Tangent Velocity Profile," *Journal of Fluid Mechanics*, Vol. 19, No. 4, 1964, pp. 543-556.

87. Miller, L. S., and Gile, B. E., "Effects of Blowing on Delta Wing Vortices During Dynamic Pitching," Journal of Aircraft, Vol. 30, No.3, 1993, pp. 334-339.

88. Mittal, R., Rampunggoon, P., and Udaykumar, H. S., "Interaction of a Synthetic Jet with a Flat Plate Boundary Layer," AIAA 2001-2773.

89. Moin, P., Squires, K., Cabot, W. and Lee, S., "A Dynamic Subgrid-Scale Model for Compressible Turbulence and Scalar Transport," *Physics of Fluids* A, vol. 3, Nov. 1991, pp. 2746-2757.

90. Morgan, P.E., Visbal, M.R. and Sadayappan, P., "Application of a Parallel Implicit Navier-Stokes Solver to Three Dimensional Viscous Flows," AIAA 2000-0961, Reno, NV, January 2000.

91. Moses, R. W. and Pendleton, E., "A Comparison of Pressure Measurements Between a Full-Scale and a 1/6-Scale F/A-18 Twin Tail During Buffet," NASA TM 110282, August 1996.

92. Moses, R. W. and Ashley, H., "Spatial Characteristics of the Unsteady Differential Pressures on 16% F/A-18 Vertical Tails," AIAA paper 98-0519, 1998.

93. Moses, R. W., "Contributions to Active Buffeting Alleviation Programs by the NASA Langley Research Center," AIAA paper 99-1318, 1999.

94. O'Rourke, M. J., Ralston, J. N., Kloc, S. J., and Langan, K. J., "Development of a Conformal Pneumatic Forebody Control for Next-Generation Fighters," AIAA 96-0786, January 1996.

95. Payne, F. M., Ng, T. T., Nelson, R. C., and Schiff, L. B., "Visualization and Wake Surveys of Vortical Flow Over a Delta Wing," AIAA Journal, Vol. 26, No.2, February 1988, pp. 137-143.

96. Peckham, D. and Atkinson, S., " Preliminary Results of Low Speed Wind Tunnel Test on a Gothic Wing of Aspect Ratio 1.0," CP-508, Aeronautical Research Council, August 1957.

97. Pedreiro, N., Rock, S. M., Celik, Z. Z., Roberts, L., "Roll-Yaw Control at High Angle of Attack by Forebody Tangential Blowing," AIAA 96-0773, January, 1996.

98. Pettit, C. L., Brown, D. L., Banford, M. P. and Pendleton, E., "Full-Scale Wind-Tunnel Pressure Measurements of an F/A-18 Tail During Buffet," AIAA paper 94-3476, August 1994, also *Journal of Aircraft*, Vol.33, No. 6, 1996, pp.1148-1156.

99. Poinsot, T. J. and Lele, S. K., "Boundary Conditions for Direct Simulations of Compressible Viscous Flows," Journal of Computational Physics, Vol. 101, 1992, pp. 104-129.

100. Polhamus, E., "Vortex Lift Research: Early Contributions and Some Current Challenges," NASA N86-27191, October 1985.

101. Reisenthel, P, Xie, W, Gursul, I., and Bettencourt, M., "An Analysis of Fin Motion Induced Vortex Breakdown," AIAA 99-0136, January 1999.

102. Rizk, Y. M., Guruswamy, G. P., and Gee, K., "Numerical Investigation of Tail Buffet on F-18 Aircraft," AIAA Paper 92-2673, June 1992.

103. Rizk, Y. M., Guruswamy, G. P., and Gee, K., "Computational Study of F-18 Vortex Induced Tail Buffet," AIAA Paper 92-4699, September 1992.

104. Rizzetta, D. P., "Numerical Simulation of the Interaction between a Leading-Edge Vortex and a Vertical Tail," AIAA 96-2012-CP, June 1996.

105. Rizzetta, D. P., Visbal, M. R., and Stanek, M. J., "Numerical Investigation of Synthetic Jet Flowfields," AIAA paper 98-2910, June 1998, also *AIAA Journal*, Vol. 37, No. 8, 1999, pp. 919-927.

106. Rizzetta, D. P. and Visbal, M. R., Blaisdell, G. A., "Application of a High-Order Compact Difference Scheme to Large Eddy and Direct Numerical Simulation," AIAA Paper 99-3714, June, 1999.

107. Rizzetta, D. P. and Visbal, M. R., "Direct Numerical and Large-Eddy Simulation of Aerodynamic Flows," Referenc document VA-00-04, the Technical Support Package free on-line at http://www.afrlhorizons.com.

108. Roe, P. L., "Approximate Riemann Solvers, Parameter Vectors, and Difference Schemes," Journal of Computational Physics, Vol. 43, October 1981, pp. 357-372.

109. Rumsey, C. L., Biedron, R. T., Thomas, J. L., "CFL3D: Its History and Some Recent Applications," NASA TM 112861, May 1997.

110. Saddoughi, S. G., "Experimental investigation of on-demand vortex generators," *Center for Turbulence Research, Annual Research Briefs*, 1994, pp. 197-203

111. Sarpkaya, T., "Vortex Breakdown in Swirling Conical Flows," *AIAA Journal*, Vol. 9, No. 9, 1971, pp. 1792-1799.

112. Schlichting, H., "Boundary-Layer Theory," McGraw-Hill, Inc.

113. Seifert, A. and Pack, L.G., "Oscillatory Excitation of Unsteady Compressible Flows over Airfoils at Flight Reynolds Numbers," AIAA paper 99-0925, 37th AIAA Aerospace Sciences Meeting and Exhibit, Jan. 1999, Reno, NV.

114. Sheta, E. F., Kandil, O. A., "Effect of Configuration Pitching Motion on Twin Tail Buffet Response," AIAA 98-0520, January 1998.

115. Sheta, E. F., Kandil, O. A., and Yang, Z., "Effectiveness of Flow Control for Alleviation of Twin-Tail Buffet," SAE paper No. 985501, 1998 World Aviation Conference, Anaheim, CA, September, 1998.

116. Sheta, E. F., "Computational Investigation and Validation of Twin-Tail Buffet Response including Dynamics and Control," Ph.D. Dissertation, Department of Aerospace Engineering, Old Dominion University, May 1998.

117. Sheta, E. F., Rock, S. G. and Huttsell, L. J., "Characteristics of Vertical Tail Buffet of F/A-18 Aircraft," AIAA paper 2001-0710, AIAA 39th Aerospace Sciences Meeting & Exhibit, Reno, NV, January, 2001.

118. Smith, B. L. and Glezer, A, "Vectoring and Small-Scale Motions Effected in Free Shear Flows Using Synthetic Jet Actuators," AIAA 97-0213, January 1997.

119. Smith, B. L. and Glezer, A., "The Formation and Evolution of Synthetic Jets," *Phsics of Fluid*, Vol. 10, No. 9, 1998, pp. 2281-2297.

120. Smith, B. L. and Swift, G. W., "Synthetic Jets at Large Reynolds Number and Comparison to Contiunous Jets," AIAA 2001-3030, 2001.

121. Taylor, S. L., Kjelgaard, S. O., Weston, J. L., Thomas, W. L. and Sellers, W. L., "Experimental and Computational Study of the Subsonic Flow About A 75° Swept Delta Wing," AIAA paper 87-2425, 1987.

122. Thomas, W. L., Krist, S. T., and Anderson, W. K., "Navier-Stokes Computations of Vortical Flows Over Low-Aspect-Ratio Wings," *AIAA Journal*, Vol. 28, No. 2, February 1990, pp. 205-212.

123. Triplett, W. F., "Pressure Measurements on Twin Vertical Tails in Buffeting Flow," *Journal of Aircraft*, Vol. 20, No. 1, 1984, pp. 920-925.

124. Vatsa, V., Thomas, J., and van Leer, B., "Navier-Stokes Computations of Prolate Spheroids at Angle-of-Attack," AIAA CP 87-2627, August 1987.

125. Visbal, M. R., "Numerical Simulation of Spiral Vortex Breakdown Above a Delta Wing," AIAA 95-2309, June 1995.

126. Visbal, M.R., and Gaitonde, D. V., "High-Order-Accurate Methods for Complex Unsteady Subsonic Flows," AIAA 98-131, January 1998.

127. Visbal, M.R., Gordnier, R. E., "A High-Order Flow Solver for Deforming and Moving Meshes," AIAA 2000-2619, June 2000.

128. Visser, K. D., and Washburn, A. E., "Transition Behavior on Flat Plate Delta Wings," AIAA paper 94-1850.

129. Washburn, A. E., Jenkins, L. N., and Ferman, M. A., "Experimental Investigation of Vortex-Fin Interaction," AIAA CP-93-0050, January 1993.

130. Webster, W. and Shang, J., "Numerical Simulation of the Unsteady Vortex Structure Over a Delta Wing," AIAA91-1814-CP, 1991.

131. Werlé, H., "Sur L' éclatement des Tourbillons D'apex D'une Aile Delta aux Faibles Vitesses," La Rechreche Aéronautique, No. 74, Jan./Feb. 1960, pp. 23-30.

132. White, F. M., "Viscous Fluid Flow," Second Edition, McGraw-Hill, Inc, 1991.

CURRICULUM VITA

for

Zhi Yang

DEGREES:

Doctor of Philosophy (Aerospace Engineering), Old Dominion University, Norfolk, Virginia, December 2002

Master of Sicence (Propulsion Engineering), Beijing Univeristy of Aeronautics and Astronautics, Beijing, China, May 1995

Bachelor of Sicence (Propulsion Engineering), Beijing Univeristy of Aeronautics and Astronautics, Beijing, China, July 1992

PROFESSIONAL CHRONOLOGY:

Department of Aerospace Engineering, Old Dominion University, Norfolk, Virginia

Research Assistant, September 1997 – Present

HONORS AND AWARDS:

ODU Aerospace Engineering Faculty Award, 2000

ODU Aerospace Engineering Faculty Award, 2001

SCHOLARLY ACTIVITIES COMPLETED:

- Essam F. Sheta, Osama A. Kandil and Zhi Yang. **Effectiveness of Flow Control for Alleviation of Twin-Tail Buffet.** AIAA Paper 98-5501@SAE Paper 985501. AIAA and SAE, 1998 World Aviation Conference, Anaheim, CA, Sept. 28-30, 1998.
- Osama A. Kandil, Zhi Yang and Essam F. Sheta. **Flow Control and Modification for Alleviating Twin-Tail Buffet,** AIAA 99-0138, AIAA 37th aerospace sciences meeting and exhibit, Jan 11-14, 1999. Reno, NV.
- Osama A.Kandil and Zhi Yang, **Adaptive Suction and Blowing Flow Control Effectiveness for Twin-Tail Buffet Control,** AIAA-99-3126, AIAA Applied Aerodynamics Conference, 17th, Norfolk, VA, June 28-July 1, 1999.
- Osama A. Kandil, Zhi Yang. **Computational and Physical Analysis of Active Vortex Generators.** IEEE 2000-0483, IEEE aerospace conference 2000, Big Sky-Montana, March 18-25, 2000.
- Osama A. Kandil, Zhi Yang and Ruobo You. **Effectiveness of Adaptive Flow Control for Twin-Tail Buffet.** AIAA 2000-4414, AIAA Applied Aerodynamics Conference, 18th, Denver, CO, Aug. 14-17, 2000.
- Osama. A. Kandil, Zhi Yang, Juan A. Pelaez and D. Mavriplis, **"NASA Space Transportation Architecture Study at Very High Angles of Attack,"** AIAA 2001-0703, Aerospace Sciences Meeting and Exhibit, 39th, Reno, NV, Jan. 8-11, 2001.
- Osama. A. Kandil, Zhi Yang and P.J. Bobbitt, **"Prediction of Sonic Boom Signature Using Euler-Full Potential CFD with Grid Adaptation and Shock Fitting,"** AIAA 2002-2543, 8th AIAA/CEAS Aeroacoustics Conference, Breckenridge, CO June 17-19, 2002.